Thickness effect in composite laminates in static and fatigue loading

Lahuerta, Francisco

DOI
10.4233/uuid:7a2d4e15-e28b-4645-94d0-64b972064c87

Publication date
2017

Document Version
Final published version

Citation (APA)
Lahuerta, F. (2017). *Thickness effect in composite laminates in static and fatigue loading*. [Dissertation (TU Delft), Delft University of Technology]. https://doi.org/10.4233/uuid:7a2d4e15-e28b-4645-94d0-64b972064c87

THICKNESS EFFECT IN COMPOSITE LAMINATES IN STATIC AND FATIGUE LOADING

THICKNESS EFFECT IN COMPOSITE LAMINATES IN STATIC AND FATIGUE LOADING

Proefschrift

ter verkrijging van de graad van doctor
aan de Technische Universiteit Delft,
op gezag van de Rector Magnificus prof. ir. K. C. A. M. Luyben,
voorzitter van het College voor Promoties,
in het openbaar te verdedigen op woensdag 18 januari 2017 om 12:30 uur

door

Francisco LAHUERTA CALAHORRA

Ingeniero Industrial (Universidad de Zaragoza, Spanje)
geboren te Zaragoza, Spanje.

Dit proefschrift is goedgekeurd door de:

Promotor: Prof. dr. ir. L.J. Sluys
Copromotor: Dr. ir. F.P. van der Meer
Copromotor: Dr. ir. R.P.L. Nijssen

Samenstelling promotiecommissie:

Rector Magnificus,	voorzitter
Prof. dr. ir. L.J. Sluys,	Technische Universiteit Delft
Dr. ir. F.P. van der Meer,	Technische Universiteit Delft
Dr. ir. R.P.L. Nijssen,	WMC Knowledge Centre
Onafhankelijke leden:	
Prof. dr. C. Bisagni,	Technische Universiteit Delft
Prof. dr. ir. M. Veljkovic,	Technische Universiteit Delft
Prof. dr. ir. T. Tinga,	Universiteit Twente
Prof. dr. ir. L.P. Mikkelsen,	Danmarks Tekniske Universitet (Denemarken)

Keywords: composite, scale effect, thickness, static, fatigue, manufacturing

Printed by: GVO Printers & Designers (Ede)

ISBN 978-94-6186-773-5

An electronic version of this dissertation is available at
`http://repository.tudelft.nl/`.

SUMMARY

Thick Laminates (above 6 mm) are increasingly present in large composites structures such as wind turbine blades. Designs are based on static and fatigue coupon tests performed on 1-4 mm thin laminates. However, a thickness effect has been observed in limited available experimental data. For this reason standard experimental data cannot automatically be transferred to thicker laminates.

Different factors are suspected to be involved in the decrease of static and dynamic performance of thick laminates. These include the effect of self-heating, a mechanical scaling effect and the manufacturing process influence.

Self-heating during fatigue is related to the material energy loss factor. During dynamic loading a certain percentage of mechanical energy is dissipated into heat, leading to a rise in material temperature. When the temperature approaches the maximum service temperature of the material, a reduction in fatigue life can be observed. The work proposes an FE method to forecast self-heating, which is validated by using empirical data.

Scaling effects and coupon geometry influence the results of thickness scaled coupon tests. The thickness effect was studied with the help of compression and tension tests on thickness scaled coupons. In order to reduce the test effects of the scaled coupon tests the coupon geometry and clamping system are designed for optimal load introduction.

The manufacturing process and curing cycles are reported as one of the leading causes to explain possible scaling effects. Through-thickness lamina properties were studied using the sub-laminates technique. In this way, it was possible to relate the in-plane lamina properties with the manufacturing properties conditions. A relation between the mechanical properties and the process conditions is proposed.

In the case of static and fatigue properties, the sub-laminates tests report a large variation in resin related properties which is dependent on the manufacturing process. Scaled tests are studied from this point of view; the scaling effect is related to the manufacturing process, and the assumption of uniform strength fields is considered not valid for thick laminates in comparison with thin laminates.

SAMENVATTING

Dikke laminaten (meer dan 6 mm) zijn in toenemende mate aanwezig in grote constructies zoals wind turbine bladen. De ontwerpen zijn gebaseerd op data voor statische sterkte en vermoeiingsterkte zoals die zijn gevonden in coupon tests met 1-4 mm dunne laminaten. In de beperkte beschikbare experimentele gegevens is er echter een dikte-effect waarneembaar. Daarom zijn de experimentele gegevens niet zonder meer toepasbaar op dikke laminaten.

Van verschillende factoren wordt vermoed dat ze van invloed zijn bij de vermindering van statische en dynamische prestaties van dikke laminaten. Hieronder vallen het effect van interne verwarming, schalingseffecten, en de invloed van het productieproces.

De interne opwarming tijdens vermoeiing is gerelateerd aan de energieverliescoefficient van het materiaal. Tijdens dynamische belasting wordt een bepaald percentage van mechanische energie gedissipeerd in warmte, wat leidt tot een toename van de materiaaltemperatuur. Wanneer de temperatuur de maximale gebruikstemperatuur van het materiaal benadert, is een vermindering van de levensduur waar te nemen. In dit onderzoek wordt een FE-methode gebruikt om de interne opwarming te bepalen, die met empirische gegevens wordt gevalideerd.

Het effect van de dikte is bestudeerd met druk- en trektesten op coupons die geschaald zijn met de dikte. De schalingseffecten en coupon geometrie beïnvloeden de resultaten van de testen. Om de neveneffecten van de testmethode te reduceren zijn de geometrie van de coupon en de inklemmingsmethode bestudeerd.

Het fabricageproces en de uithardingscycli wordt gerapporteerd als een van de belangrijkste oorzaken die mogelijke dikte-effecten verklaren. De variatie van de laageigenschappen over de dikte is onderzocht met behulp van sub-laminaten. Op deze manier is het mogelijk om de laageigenschappen te relateren aan de verschillende condities die in de verschillende lagen tijdens fabricage optreden. Een relatie tussen de mechanische eigenschappen en de condities tijdens fabricage wordt voorgesteld.

Bij statische en vermoeiingstesten laten de testen van de sub-laminaten grote spreiding zien in de eigenschappen gerelateerd aan de hars. Deze spreiding is afhankelijk van het productieproces. Vanuit dit oogpunt worden geschaalde tests bestudeerd. Het schalingseffect blijkt gerelateerd aan het productieproces. De aanname dat de sterkte uniform is over de dikte is niet geldig voor dikke laminaten zoals die wel voor dunne laminaten geldt.

Past glories are poor feeding.

Isaac Asimov, Foundation

CONTENTS

1

INTRODUCTION

This chapter gives a general overview of the different topics involved in the three mechanisms that build the thickness effect, before motivating this dissertation.

MOTIVATION

From a mechanical point of view wind turbine blades are composite structures that are in most cases composed of sandwich panels, spar caps and adhesive bond lines (see figure 1.1). The main design requirements for a wind turbine blade are:

- low cost per kWh (cost of energy COE)
- high stiffness (to maintain tower clearance)
- fatigue resistance (with minimal service life $> 10^8$ load cycles with complex rainflow counting spectrums)
- environmental resistance (coatings resistant to humidity, ice, UV and erosion)
- low maintenance costs and downtime

The wind turbine blades COE share depends on the downtime and on the blade costs.

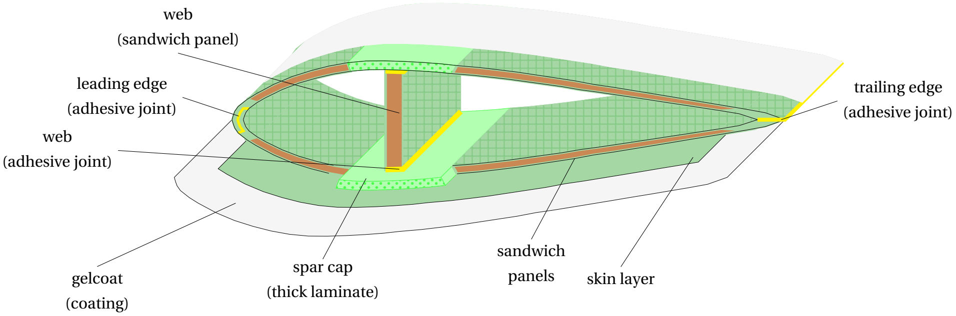

Figure 1.1: Composite materials in a wind turbine blade.

Downtime failure modes are partly associated with the bond lines, sandwich panels and environmental degradation of the coating (i.e. leading edge erosion). Blade costs are associated with blade design, materials and manufacturing methods.

The blade stiffness and fatigue resistance requirements are mainly dominated by the spar cap design. In general, spar caps are the main load carrier in the blade structure, and when there is a failure in the spar cap, it is catastrophic. Spar caps represent around 50% of the blade materials costs [1], because most of the glass and / or carbon fibers are located in the spar caps. Therefore, a significant part of the structural research focuses on the mechanical characterization of materials that are representative for the blade spar caps [2].

Spar caps are monolithic UD-dominated thick laminates, which can include a fraction of biax reinforcement. Spar cap thicknesses increase with length and class of the blade up to 100 or 150 mm thick for 70-80 meter long blades. However, the mechanical characterisation of the materials representative of the spar caps thick laminates is based on static and fatigue test on 1-5 mm thin coupons. It is not certain whether the actual material performance in thick laminates is the same as that in the thin laminates standardized test. Possible scaling effects must be taken into account with the use of safety factors [3–6]. This difference in scales is potentially problematic and further understanding of the possible scaling effects is required to avoid over-dimensioning or unexpected failure.

Daniel [7] performed a series of thick compression tests reporting complex kink bands geometries and no significant changes on the overall compressive strength. Later Zimmermann [8] tested and modeled an ultra thick laminate composite sub-component reporting significant material property degradation for ultra thick laminates. Moreover, Stammes & van Wingerde [9–11] carried out tests on thick laminates showing significant differences in the S-N curves of thin and thick laminates. Figure 1.2 shows the S-N curves of 4 and 30 mm thick coupons where a significant thickness effect was reported as well as a test effect due to the grip system. Therefore, because of the increasing presence of thick laminates in the main structural parts of the present and future wind turbines blades, a study on the behaviour of thick laminates testing, manufacturing and properties is valuable.

The aim of this thesis project is to study the effect of thickness on the static and fatigue properties of composite laminates. Moreover, in order to determine the mechanisms that drive the observed differences between thin and thick laminates, the approach followed in the present work is to identify potential mechanisms involved in the thickness effect and to study the contribution of each mechanism independently. The following mechanisms are considered:

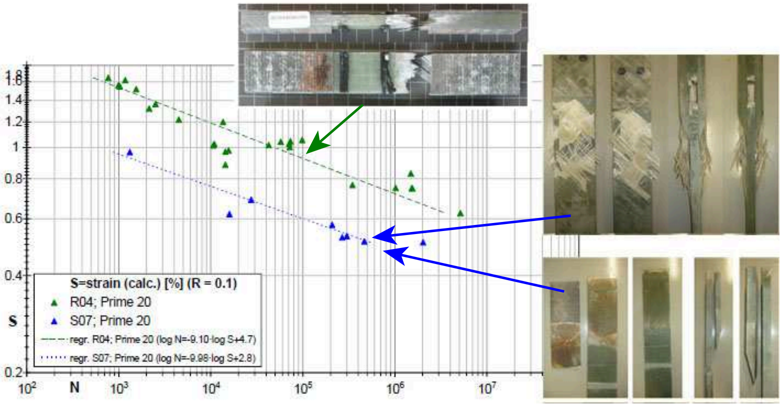

Figure 1.2: S-N curves for 4 (above, green curve) and 30 mm (below, blue curve) UD thick coupons (Stress, R = 0.1) performed by WMC [9].

- scaling effects and the influence of design parameters on thick laminates scaled coupon stress mechanical tests
- self-heating of thick laminates and its influence on mechanical properties during dynamic loading
- the influence of the manufacturing process on the mechanical properties of thick laminates

THESIS OUTLINE

This thesis is divided into six chapters. In the remainder of this chapter a literature review of the main topics involved in the thickness effect is discussed. In chapter two the self-heating effect in thick laminates is described. Coupons of different thicknesses are tested at various frequencies and under various insulation conditions. The tests are correlated with an analytical self-heating model in which a fraction of the strain energy is transformed into heat. This strain energy fraction corresponds to the loss factor that is measured empirically. Additionally, to forecast the temperature rise during the dynamical loading in the laminate core, an FE methodology based on this mechanism and the empirical loss factors is described.

In chapters three and four, studies into the scaling of the strength of thick laminates are presented for compression and tension coupons respectively. A detailed study of a suitable coupon geometry and manufacturing process for thick laminates coupons is carried out. Scalable coupon geometries are designed for compression and tension tests where the testing side effects need to be minimised. Based on these coupon designs, different thicknesses are tested under static and cyclic loading.

Chapter five studies the influence of the manufacturing process of thick laminates and the variability of the lamina properties through the thickness. For this purpose, thick laminates are manufactured, and sub-laminate panels are extracted from the thick laminates. The sub-laminate panels are tested as standard thin specimens and the distribution of properties through the thickness is evaluated and correlated with the local curing cycles. Moreover, to validate the influence of the manufacturing process these data are correlated to the scaled compression tests results from chapter three.

During the realisation of this work, two different experimental tools were developed. Appendix A describes an image processing tool that allows to monitor the delamination length in a double cantilever beam (DCB) test. With these tests, the strain energy release rate used in the FE models described in Chapter three and four was determined. Appendix B describes a passive infrared technique that allows to identify the locations that are experiencing the larger degradation due to fatigue. This technique was used in the fatigue test of chapter two and three.

RESEARCH QUESTIONS

The aim of the project is to determine how representative static and fatigue properties from tests on thin laminates are for those of a thick laminate. Several mechanisms are involved in the behaviour of a thick laminate compared with a thin one. Three mechanisms that are believed to have the highest impact on the performance of thick laminates were studied. Therefore, the main research question is decomposed in three sub-research questions to be studied independently (see figure 1.3). The central question is whether a size effect does exist. Next, there is the question what causes it. To answer the central question a direct approach is to carry out scaled tests and observe the behaviour. A prerequisite for this study is a robust test design to measure the size effect while minimizing the test influence (see chapter three and four). Moreover, two leading causes of the size effect are studied, the self-heating (see chapter two) and the influence of the manufacturing effect (see chapter five).

The study of self-heating (see chapter two) is considered as an attempt to answer the first sub-research question because it is believed to be a mechanism that can reduce fatigue performance of a thick laminate. GFRP (glass fiber reinforced polymer) presents two characteristics, poor thermal diffusivity properties and glass transition temperatures close to the ambient temperature operational ranges (between -40 to 50°C). According to the bibliography and practical experience the material temperature rises under dynamic loading due to the energy dissipation. If thick laminates are loaded in fatigue, the temperatures in the core of the laminate might rise above the operational range of the composite material. In particular, this applies to fatigue tests of thick laminate sections, where there

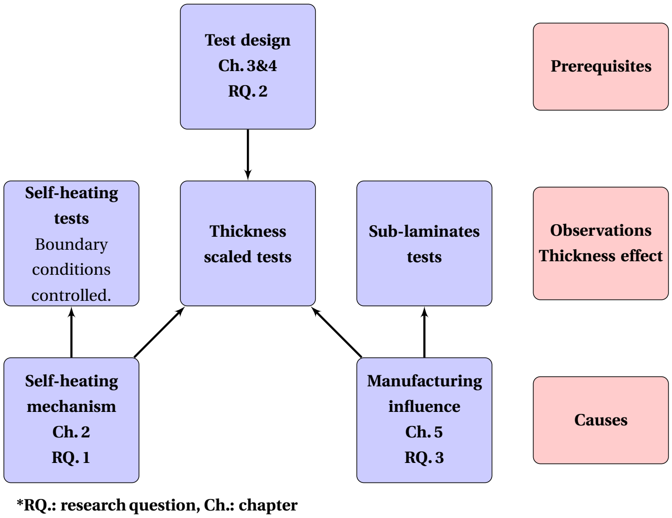

Figure 1.3: Thesis structure & research questions

is a compromise to be addressed between the test frequencies and the duration of the tests.

Scaling effects are an open topic in literature. Several references have been reported regarding CFRP (carbon fiber reinforced polymer) scaled static tests. However, the available literature in the case of GFRP regarding fatigue properties is scarce. To study the influence of the thickness carrying out scaled tension and compression tests was chosen as a straight forward approach. However, thickness scaled tests present some technical challenges and require several considerations regarding the influence of the tests on the final results. Therefore, the study of the thickness scaling via scaled tests is considered as a second sub-research question, where the test design, the tests setup and the geometries to be tested are studied (see chapter three and four).

The reviewed literature regarding the manufacturing process of GFRP laminates reports that there is a relation between the manufacturing conditions and the final performance of GFRP laminates. However, a direct correlation between both was not found. One of the main differences between thin and thick laminates is that during the manufacturing of thick laminates, curing cycles need to be smoothed (avoiding temperatures above degradation limits) due to the exothermic nature of the GFRP resin material. Therefore, to study the influence of the manufacturing process in thick laminates mechanical properties is considered as the third sub-research question (see chapter five).

* * *

EXPERIMENTS MATERIAL & MANUFACTURING METHOD

The same composite material was used for all experiments carried out in this thesis. The chosen material was a commonly used wind energy epoxy resin (Hexion RIM 135), a UD-glass fibre type E non-crimp fabric and when necessary a glass fibre type E biaxial material.

Plates were vacuum infused in a single-sided aluminium mould. In general, averaged fibre weight ratios were 70%, the void content was under 0.1%, and glass transition temperature (T_g) was around 80-85 °C. A conventional vacuum infusion process configuration with in-plane flow was used (see figure 1.4), and constant vacuum was applied during the whole curing cycle. The resin was tempered at 25 $^\circ C$ before the infusion and degassed while infused. The same manufacturing process conditions were arranged for the different plates, except the curing cycles and layouts.

The mechanical properties used for the FE calculations are shown in table 1.1.

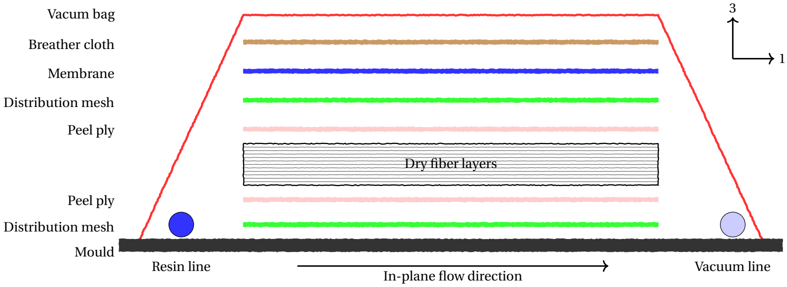

Figure 1.4: Vacuum bagging configuration.

SIZE EFFECT

In the remainder of this chapter a literature review related to the research questions is presented, starting with the topic of size effects under static loading.

Concerns about size effects were already discussed by Leonardo Da Vinci (1500's) suspecting that among cords of equal thickness the longest is the weakest [15]. Since then until our times different pieces of evidence on sizes effects in composites and other materials have been studied. In Bažant's [16] review on size effects in structural strength, the size effect in solid mechanics is understood as the change of the nominal strength of the structure when structures of similar shape but different size are compared.

Zweben [17] has listed significant observations on the existence of a size effect in composites:

- The mean tensile strength of carbon and glass fibers decreases for increasing length

		UD material		Biax 12	
		Type E Glass Fiber		**Type E Glass Fiber**	
		MPa		MPa	
Elastic modulus	E_{11}	39500	****	26000	**
	E_{22}	13190	**	26000	**
	E_{33}	13190	**	13190	***
Poisson	ν_{12}	0.26	****	0.15	**
	ν_{23}	0.26	**	0.15	**
	ν_{31}	0.08	***	0.08	***
Shear modulus	G_{12}	3535	**	3535	**
	G_{13}	3535	***	3535	***
	G_{23}	3535	***	3535	***
Tension strength	σ_{t11}	849	****	424.5	**
Compression strength	σ_{c11}	630	****	315	**
Shear strength	τ_{12}	43.5	**	43.5	**
Tension strength	σ_{t22}	85	**	424.5	***
Compression strength	σ_{c22}	147	**	315	***
Shear strength	τ_{23}	43.5	***	43.5	***
Tension strength	σ_{t33}	85	***	85	***
Compression strength	σ_{c33}	147	***	147	***
Shear strength	τ_{13}	43.5	***	43.5	***
Delamination Normal	σ_{max}	85	****	NA	
Delamination Tangencial	τ_{max}	50	****	NA	
Fracture toughness	G_{Ic} $[J/m^2]$	1250	[12]	NA	
	G_{IIc} $[J/m^2]$	4500	[13]	NA	
	G_{IIIc} $[J/m^2]$	4500	***	NA	
Layer thickness	[mm]	0.719	****	0.675	****

Table 1.1: Thesis experiment material mechanical properties (* Datasheet, ** Upwind [14], *** Assumption, **** Measured).

- The mean tensile strength of twisted and untwisted bundles of fibers decreases for increasing length
- Tensile failure of UD material is related to statistical failure of fiber breakage
- Tensile coupons are weaker than impregnated fibers
- Tensile and compression strengths derived from bending tests exceed tensile and compression test strengths obtained from uniaxial tests of un-notched specimens

On the other hand, according to the Pi-theorem set out by Buckingham it is possible to scale a model and obtain the same behavior as the prototype. However, the model behavior is found to be inaccurate [18]. In Sutherland's [19] review, it is concluded that despite the lack of consensus numerous authors agree that a size effect exists, and some reasons are suggested for this effect:

- Some mechanisms are insignificant at model scale but not at prototype scale
- Measurements and construction accuracy are at different scales
- Properties are affected by scale due to manufacturing processes
- It is not possible to scale fibers sizes
- It is technically challenging to scale ply thicknesses
- It is not very clear how to scale the manufacturing defects
- Failure mechanisms do not scale with size

Jackson [20, 21] performed a series of buckling tests on CFRP laminates, scaling the ply thickness and the laminate thicknesses from 0.3 mm to 5 mm. It was concluded that the results exhibited a scale effect in strength. Grimes [22] also argumented that size effects occur due to the difference in manufacturing quality that exists between large scales and small scales. Moreover, he argued that in the case of multi-material parts induced manufacturing differences like thermal stresses play a role. Grimes [22] reported a size effect in strength up to 8% in laminates and up to 40% in bonded joints.

In the case of compression strengths Camponeschi [23] reported on the effect of the thickness, concluding that there is a drop in the compression strength with increasing thickness, which is related to the material quality or tests side effects. There are tests with specific configurations that seem not to show size effects, such as the thick section CFRP pressure cylinder tests conducted by Blake [24]. It should be noted that the manufacturing processes and material grades used in these tests are relatively far from those used in the wind energy industry standards in terms of of cost and production rates. Bing [25] studied the size effect in end-loading compression coupons on off-axis tests, observing a decrease of strength with the increase in thickness, which further increases when the off-axis angle is close to zero degrees.

Wilkins [26] reviewed the nature of scaling effects with an emphasis on the use of

Weibull theory. This theory states that the probability of defects increases with the increase of the volume. Wang [27] also defended that there is a dependence of material strength with the volume that should be understood as a scaling effect. According to Wang [27] composite parts are manufactured with an initial defect distribution. Depending on the loading mode these defects grow until one becomes dominant and initiate failure. This point of view of failure leads to the concept of the effective or critical defect. The effective defects are described as the ones from all the possible causes that grow until final structural failure; they are studied from a fracture mechanics point of view.

Phillips [28] also reported a size effect for a comparative test of three and four point bending tests of GFRP. These results were studied using the two different theories that exist to explain size effects, the Weibull strength theory and the fracture or mechanics approach. Wisnom [29] described a size effect using the Weibull strength theory on bending tests where only the length and not the thickness was modified. Regarding the tensile strength Byron [30] performed a statistical analysis of laminates up to 60 plies, observing a decrease in the mean strength with increasing laminate thickness. Also Wisnom [31] found a size effect on a tensile test of around 16% for 64 plies CFRP coupons specially designed to avoid failure in the grips. Different gauge sections, thicknesses and widths were tested, and the decrease of strength fitted the Weibull strength theory. Lately, in his review Wisnom [32] discussed that the size effect depends on the failure mechanism. The studies show that failure mechanisms dominated by the fiber show a decrease in the strength with increasing volume according to Weibull strength theory.

On the other hand, there are also studies towards size effects in which it is reported that there is no statistically significant size effect regarding strength reduction. This is the case in Sutherland [33, 34] and Davies [35]. In both cases, tensile and flexural tests were carried out for different sizes and thicknesses but no relation between size and strength was found. Both studies were performed on marine hand lay-up composites, were the variability of defects induced by the manufacturing is higher. In the case of higher grade materials such as CFRP, Lavoie [36] performed a series of tensile test in a range from 1 to 4 mm thick coupons that did not show any variation with the volume of the coupon (discarding failures in the grips). It was concluded in this study that the Weibull strength theory cannot be used for predicting size effects.

There is also interesting research on size effects of notched coupon and open hole tests [37, 38]. However, these tests are not as common in wind industry as in aerospace industry, because in comparison has less representative design load cases.

A classic theory to explain size effects is the Weibull statistical strength theory [39] also referred to as the weakest-link theory [40]. The validity of this theory has been prove on materials such as ceramics, wood and it has also been considered by some authors for composites [17, 41]. In the Weibull theory, it is assumed that the material is made up of linked elements. When one of these elements fails, the structure collapses. In other words, the strength is limited by the weakest element.

Another classical theory to explain the size effects is based on crack density growth [42], where the amount of cracks per volume is considered until one or more of them arrives at a critical size which leads to failure. According to this, strength depends on the volume of material and the thickness. Based on both criteria different authors have proposed theories to explain the size effect [43–46] either from a purely statistical point of view or based on deterministic size effect models.

Resuming, it can be concluded that there is disagreement about the existence of an inherent size effect for composites. However, there is a major consensus on the fact that achieving the same strengths in small coupons or scaled models as thick coupons or full-scale prototypes is not obvious. The reasons for these might be different, such a:

- Test influences
    - Effect of the testing methods and failure modes
    - Influence of boundary conditions
- Manufacturing influences
    - Difficulties in scaling the measurement accuracy and manufacturing tolerances at different scales (angle orientations, ply drops)
    - Difficulties in scaling fibre diameters and ply thicknesses
    - Induced manufacturing defects that are non-scalable
    - Variability of material properties induced by the manufacturing process that is not scalable or difficult to reproduce
- Size effects
    - Weibull statistical strength theory
    - Increase of the number of manufacturing defects with volume
    - Increase of the defects growth speeds
    - Stress gradients that vary with the loading mode and dimensions

Scaling effects remain a research topic, even though numerous works have been published on the topic. A direct approach in which scaled geometries are tested present technical challenges. Since loads increase with increasing specimen size, different test frame sizes are required. Furthermore fatigue test frequencies must be adapted if self-heating is considered. Limited bibliography was found on scaled static compression and tension coupons tests, and even less in the case of fatigue properties. Therefore, the design of scaled tension and compression tests was identified as one aspect of the approach followed in this thesis.

DYNAMIC LOADING (FATIGUE)

Different failures modes can occur during damage evolution such as: fiber fracture, matrix cracking, matrix crazing, fiber buckling, fiber-matrix interface failure and delaminations. As a consequence of the initial manufacturing conditions, coupon scale effects and the testing conditions, the different damage modes and interaction between them under fatigue loading occur at different rates leading to a size effect in total fatigue life [47]. In addition, experimental fatigue data on thick laminates have suggested that their performance cannot be based on relatively thin laminates [9, 48].

According to Fong [49] there are two reasons why fatigue modeling, in general, is so difficult and expensive. The first reason is the several scales at which damage mechanisms are present: from atomic level, through levels of different phases, to component and structural level. The second reason is the impossibility of producing identical specimens with well characterized microstructural features, due to the manufacturing variability and characterization techniques.

Nyman [50] in 1996 concluded that the following points should require further investigation to improve fatigue life forecasting:

- The Goodman corrections for different stress ratios
- Multi-axial loading fracture criteria
- Testing methods for compressive failure
- Load sequence effects

In general, fatigue models can be classified into three categories: fatigue life models, phenomenological models for residual stiffness / strength and progressive models [47]. All of which have lifetime prediction as the main outcome.

- *Fatigue life models* use the information from S-N curves or Goodman-type diagrams and propose a fatigue failure criterion under fixed loading conditions
- *Residual strength models* have an inherent failure criterion restriction. Failure occurs when the applied stress is equal to the residual strength, or when the stiffness degradation crosses a certain threshold [51]
- *Progressive damage models* introduce one or more damage variables that describe the deterioration of the component

Common practice to determine static design limits of composite glass fibre reinforced parts such as wind turbine blades, test material characteristic values (stresses and strains) to a probability of 5% of failure according to a normal distribution. Moreover, reduction / safety factors are applied based on previous experimental tests [52] and standards such as the Germanischer Lloyd guidelines [3].

A similar approach is used to determine fatigue limits. To predict durability due to fatigue a Miner's rule or a residual strength model [53] is used, in conjunction with the Goodman diagram [54–56]. It allows to predict the cycles to failure as a function of mean and amplitude stress. Such models are constructed based on test material quasi-static properties (stresses and strains), S-N curves slopes and the reduction factors defined by the standards.

In both static and fatigue design, the material values are based on specimens not thicker than 4 mm obtained according to the appropriate test standard. Therefore, scaling effects, manufacturing effects and ageing effects that are present in the final structural behaviour are accounted for via reduction factors.

HEAT GENERATION OR SELF-HEATING DURING FATIGUE

When a metal spoon is cyclically bent up and down until it breaks (=fatigue), the spoon temperature will rise without external heat sources (=internal heat generation). Although this process is intuitive, the increase of temperature is a difficult process to explain from a scientific point of view, since energy dissipation is based in non simplified or ideal physical systems.

Since the first observations of the hysteresis loops in metal fatigue tests (Inglis [57] and Lovell [58]), different authors have related the area of these loops with the energy dissipation of the material, with internal friction or with fatigue damage. A rise in temperature on cyclic loading is the consequence of this dissipation. According to Moore [59] the recording of temperatures and its relation to fatigue was already suggested by Stromeyer in 1913. However, the problem was not formulated thermodynamically until the sixties by Green [60], Mroz [61, 62] and Nicholson [63].

Energy dissipation is part of several thermal fatigue and spontaneous heating theories in thermoplastic polymers [64–67]. The heat generated per unit of volume during the cycle is proportional to the work of the irreversible deformations as a consequence of the hysteresis, expressed as,

$$Q_R \simeq \sigma_a \cdot \epsilon_a \cdot w \cdot sin(\delta) \tag{1.1}$$

where Q_R is the heat generated rate, σ_a and ϵ_a are the stress and strain amplitudes, w is the loading frequency and δ is the phase-lag angle between the complex and real moduli which is proportional to the specific loss coefficient.

It has become possible to consistently monitor the temperature evolution during the cyclic loading with the development of thermography in the late 1950s. Since thermal imaging has become available, different researchers have monitored fatigue tests via infrared (IR) cameras to study thermal evolution. Reifsnider [68, 69] introduced the technique to composites testing boron / epoxy and boron / aluminium at different frequencies where the hysteresis loops and the temperature evolution were recorded. Based on that experimental data it was reported that there exists proportionality between the energy dissipation rate measured from the hysteresis cycles and the temperature increase. Also a temperature steady state after an initial transient temperature rise was reported [68].

Wong [70] developed a hybrid numerical/experimental technique for determining the heat dissipated during fatigue loading. For an aluminium alloy, it was reported that between 85% to 95% of the irreversible work dissipated as heat. For composites, Reifsnider discussed that part of the irreversible work dissipated as heat in the material and is used up as new surface energy coming from internal cracks, delaminations and fibre breakage [68]. Although, no conclusive bibliography has been found on these matters, it can be assumed that a very low percentage is involved in new surface energy development, so that this contribution can be neglected [71].

In Kenny's [72] experimental study of the elasto-plastic behaviour of thermoplastic composites under cyclic loads, based on the measuring of damping ratios, it was reported that the autogeneous heating of the specimen is due to internal friction during the cyclic loading and that the temperature rise can be evaluated under adiabatic conditions.

Jacobsen et al. [73] monitored FRP and ceramic composites in an adiabatic chamber during fatigue loading with thermocouples and an IR camera. With the help of a one-dimensional model for the heat loss under steady-state conditions, a methodology was described to measure variations in damping and stiffness properties. Similar observations on hybrid GFRP were made by Redon [74, 75], reporting that damage and heat localization lead to impending failure, while the parameters that control the localization need a better understanding to improve the fatigue resistance of the material by sensible microstructural design.

One of the major applications found for the monitoring of energy dissipation with an IR camera is the determination of the fatigue limits in metals via an accelerated test. This is possible, due to the sharp change that the temperature shows at the point of failure [76–80].

Recently Audenino [81] correlated the damping ratio measured with vibrational tests to the thermographic signal of two different types of steel for fatigue testing. For this purpose, a simple model for main thermal effects was described as:

$$Q_{\phi} + Q_{Kin} - Q_{Kout} - Q_r - Q_h = \Delta U_{int} \tag{1.2}$$

where Q_{ϕ} is the internal heating source, $Q_{Kin} - Q_{Kout}$ are the conductivity balance terms with the surroundings of the system, Q_r is the radiance heat exchange, Q_h is the convective heat exchange and ΔU_{int} is the internal energy.

According to Johnson [82] the evolution of the average temperature recorded by the IR camera can be used for characterising damage in fatigue tests. The use of thermography is particulary beneficial in the case of thick-section composites where it is not possible to monitor damage with other techniques, which only offers surface measurements. Thermography has been used on thick coupons recently [83, 84]. According to Toubal [85] this technique shows the relation between heat dissipation and damage for composites. It can be observed that the average temperature signal follows the same evolution as the modulus degradation curves that are normally divided into three phases.

Recently Naderi [86], Eleuteri [87] and also Maitournam [88] proposed a thermodynamic approach for the characterization of material degradation. These works claim that the cumulative entropy generation is constant at the time of failure and is independent of geometry, load and frequency. The fracture fatigue entropy is defined as,

$$s_f = \int_0^{t_f} \left(\frac{W_p}{T} - \frac{J_q \cdot gradT}{T^2}\right) \cdot dt \simeq \int_0^{t_f} \left(\frac{W_p}{T}\right) \cdot dt \tag{1.3}$$

where, the first term is defined by energy dissipation per cycle and the second term is the conductivity diffusion, generally assumed as negligible. Both terms are integrated during the total life. These observations were reported for metals [86, 89–91] and epoxy glass fibre reinforced composites [92–94].

In the OPTIMAT and INNWIND thick coupons tests, initially no thickness dependence of fatigue results was reported [10]. However, lately Stammes [9] reported that lower performance of thick sections was observed which might be related to the temperature build up inside the laminate.

Based on the different studies reported in this section, it can be concluded that fatigue and energy dissipation have a strong relation in composites. Taking into account that GFRP composites have poor diffusivity properties, the temperature rise due to fatigue might be an issue for thick laminates. Therefore, a better understanding of the causes and how to forecast the self-heating mechanism is required.

MANUFACTURING PROCESS INFLUENCE IN COMPOSITE MECHANICAL PROPERTIES

To evaluate laminate performance, a laminate has to be manufactured first. Voids, resin rich areas, dry spots and other defects and flaws are inevitably formed during the manufacturing process. The different parameters involved in the manufacturing process such as the curing cycle, and the infusion process are likely to modify the final mechanical properties.

Lee [95] elaborated a series of expressions that can be used in conjunction with cure models to evaluate the effects of the curing cycle on strength values and moduli of the composite after manufacturing. A relation between heat transfer rates and the interlaminar shear strengths (ILSS) was observed by Davies [96] and also by Liu [97] for epoxy resin in carbon-reinforced composites.

White [98] reported that the curing temperature determines the degree of curing and the resin system ultimate strengths. Huang [99] described different interfacial failure properties for two different curing cycles with differences of 20%. Also, Ziaee [100] reported a strong variation in strength and a decrease of 70% in the fracture toughness for different cure temperatures for vinyl-ester resins. Moreover, Zhang [101] reported a strong influence of the temperature ramps in the cure cycle on the hardness of an epoxy resin.

White and Kim [102] developed and studied a technique of staged curing. In this technique, two or more thin (<5 mm thick) prepreg laminates are manufactured at once with a similar curing cycle per staged laminate. Later, Ciriscioli [103] reported a technique to determine mechanical properties of thick pre-pregs using a porous film in between. This technique was applied to compare the properties of laminates of different thicknesses at the middle thickness position. Moreover, a technique to extract sub-laminates with the help of peel-ply layers from thick laminates was successfully applied and used to evaluate the mechanical properties at different thicknesses positions [104]. Lately Boey [105] reported a dependence of the flexural properties with the curing cycle and Shin [106] the process sensitivity of the compression strength.

While for thin laminates curing temperatures do not show large gradients through the thickness, in thick laminates strong gradients are observed [107]. Effectively, this is related to a curing cycle variation through the thickness, which can be expected to become more pronounced in thicker laminates. These gradients are caused by the exothermic nature of most curing cycles and the low thermal conductivity of the (uncured) resin.

Also, temperature gradients during the curing cycle are related to residual strains in composites that can lead to warpage and shrinkage [108, 109]. To monitor the curing cycle and the residual strains, different techniques can be used. Regarding the curing cycle, thermocouples and dielectric sensors allow to record the evolution of the curing temperature and matrix curing degree, respectively. Regarding the residual strains, strain gauges and embedded fibre Bragg sensors allow to monitor the strain development during the curing. Alternatively the hole drilling method (ASTM E837) can also be used to determine residual strains after manufacturing.

The works reported in this section share a general idea: temperature and manufacturing conditions have an impact on the laminate mechanical properties. However, no literature was found relating mechanical properties with manufacturing conditions for thick laminates. In fact, how to determine curing cycles remains an open question for the manufacturing of composite laminates. In spite of all uncertainties the manufacturing process, it is very likely that thick laminates present differences in comparison with thin laminates due to differences in local curing cycles and manufacturing conditions. To study the impact of the manufacturing conditions on the performance of thick laminates is therefore identified as a significant topic.

2

HEAT GENERATION OF THICK LAMINATES UNDER FATIGUE

Due to the poor thermal conductivity of composites and the material heating that occurs during fatigue loading, high temperatures may appear in the laminate. Since the mechanical properties of composites are dependent on the temperature, the fatigue performance may be affected negatively when local temperatures increase. This chapter describes the self-heating mechanism in thick laminates, propose an FE methodology to forecast such mechanism and reports a series of mechanical experiments. The comparison between FE models and experimental observations confirms the validity of the methodology.

INTRODUCTION

Heating of material is a factor to be considered during fatigue testing, which is supported by the ASTM D3479 [111] recommendations. Particulary for thick laminates heating is relevant [9, 112].

During cyclic loading of a laminate coupon, a percentage of the mechanical strain energy is transformed into heat due to non-reversible processes [66, 68]. This is also called intrinsic dissipation [74, 113, 114]. The non-reversible conversion of mechanical energy into heat is influenced by viscoelasticity, plasticity, damage and internal friction. These cause a change of the state of the material (effective stress and strain) and therefore a change in the internal energy that a given volume of material has. Energy release leads to the endogenous heating or self-generated heating of the material.

Heat generation during fatigue has been studied by different authors. Kenny and Marchetti [72] related the heating of a thermoplastic composite with the visco-plastic phase angle that appear during the dynamic loading. Audenino [81] correlated the material specific damping with thermographic observations carried out in steel. Katunin [115]

This chapter was extracted integrally from [110].

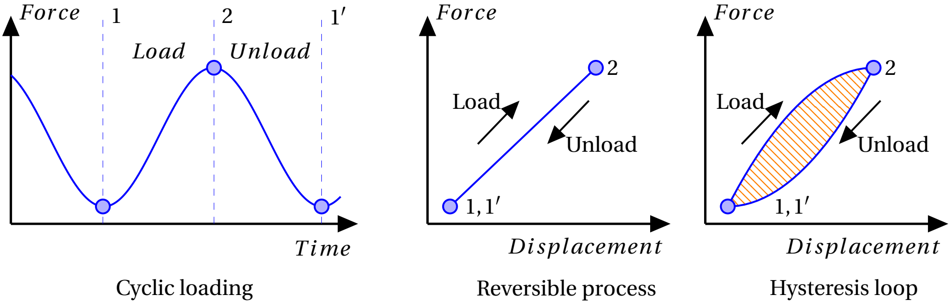

Figure 2.1: Scheme of cyclic loading. Reversible process and process with hysteresis loop.

proposed an analytical solution to the heat generation problem (also called self-heating) in the steady state based on a visco-elastic model.

In ideal mechanical reversible processes (see figure 2.1) the loading strain energy is equal to the unloading strain energy and there are no mechanical energy losses. In case of non-reversible processes, however, a certain degree of cycle hysteresis appears during a sinusoidal cyclic loading and unloading process.

When a hysteresis loop is developed the strain energy built up between point 1 and 2, and the strain energy returned between 2 and 1 are not equal. Thus, there is a loss of mechanical energy in the process defined by the following equations:

$$W_{1-2}^{load-norev} = \int_1^2 \sigma \cdot d\epsilon \tag{2.1}$$

$$W_{2-1}^{unload-norev} = \int_2^1 \sigma \cdot d\epsilon \tag{2.2}$$

$$\Delta W_{loss} = W_{1-2}^{load-norev} - W_{2-1}^{unload-norev} \tag{2.3}$$

The loss of mechanical energy during the cycle can be represented as a ratio of the total strain energy of the cycle in a reversible process. The hysteresis energy loss during the cycle is related with to cycle elastic energy according to the energy loss factor [112, 116]:

$$\Phi = \frac{\Delta W_{loss}}{W_{1-2}^{load-rev}} \tag{2.4}$$

Heating during the cyclic loading is linked to the mechanical process. The volumetric internal heat flow $\dot{Q}^{generated}$ that appears during cyclic loading can be expressed as [115],

$$\dot{Q}^{generated} = f \cdot \Phi \cdot W_{1-2}^{load-rev} \tag{2.5}$$

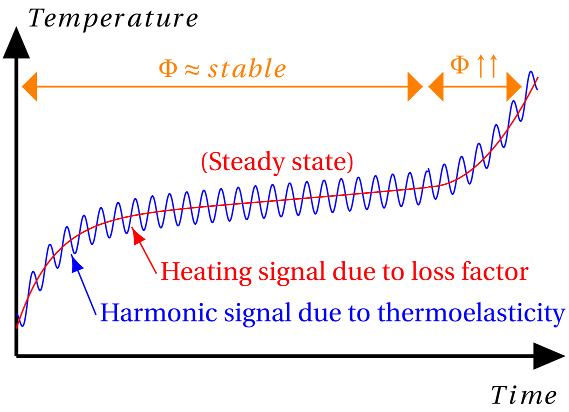

Figure 2.2: Schematic temperature evolution during a fatigue test at constant environmental temperature.

where f is the frequency, Φ is the loss factor during the cyclic loading and $W_{1-2}^{load-rev}$ is the change in elastic strain energy during the cycle, defined as,

$$W_{1-2}^{load-rev} = \frac{\sigma_2^2 - \sigma_1^2}{E} \tag{2.6}$$

where σ_2, σ_1 are the stresses in the maximum and minimum cycle states and E is the elastic modulus.

Additionally, the thermo-elastic contribution dependent on the thermal expansion coefficients causes an harmonic temperature variation with the load. In figure 2.2 a schematic is shown of the temperature evolution during dynamic loading at constant environmental temperature, in which the internal temperature development can be divided in three phases. The first increase is related with the transient state (heating up of the specimen). In the second part the temperature of the specimen is in equilibrium with its surroundings and the loss factor remains relatively stable for a large part of the fatigue life of the specimen [117] showing a minor increase. In the final phase, the loss factor increases due to a rapid increase of damage, and the temperature also increases from the steady state temperature until failure.

This characteristic behaviour is relevant for thick Glass Fibre Reinforced Polymer (GRP) laminates, where the thickness and the poor thermal conductivity of the matrix and glass fibre reinforcements can lead to a substantial increase of temperature in the core of the laminate during cyclic loading. If the temperature comes too close to the glass transition temperature, damage can occur as a consequence of the heating.

Since the stiffness of composites decreases dramatically when the temperature of the material exceeds the glass transition temperature, heating in fatigue can lead to premature failure. Ability to forecast the temperature during fatigue is helpful for the design of thick laminate fatigue tests or of composites structures loaded in extreme temperatures conditions. The aim of the present work is to study heating in fatigue experiments on thick laminates. For this purpose fatigue tests for laminate thicknesses between 10 to 30 mm at different loading conditions are reported. A finite element model to forecast the temperature rise during fatigue tests is described and evaluated with experimental data.

ANALYTICAL SOLUTION OF THERMAL DISTRIBUTION

The stationary thermal distribution of a thick, dynamically loaded laminate, can be studied analytically by modelling the composite as a wall with an internal heat generation according to the one-dimensional heat transfer theory [118], based on the following assumptions:

- uniform heat generation
- infinite width and length
- uniform conductivity.

Taking into account these assumptions, the one-dimensional temperature distribution through a conductive wall with internal heat generation as illustrated in figure 2.3 is defined as,

$$T(x) = \frac{\dot{Q}^{generated} \cdot (L/2)^2}{2 \cdot k} \cdot \left(1 - \frac{x^2}{(L/2)^2}\right) + T_s \tag{2.7}$$

the internal heat that leaves the wall is balanced by the energy leaving via convection (where h and A are the convection coefficient and the interchange surface area respectively),

$$\dot{Q}^{generated} \cdot (L/2) \cdot A = h \cdot A \cdot (T_s - T_\infty) \tag{2.8}$$

Merging eq. 2.7 at the middle ($x = 0$) and eq. 2.8 with the internal heat generation from eq. 2.5, in a 1D model the core temperature is calculated as,

$$T_m = f \cdot \Phi \cdot W_{1-2}^{load-rev} \cdot \left(\frac{L^2}{8 \cdot k} + \frac{L}{2 \cdot h}\right) + T_\infty \tag{2.9}$$

where k, T_m, T_s, T_∞, are the thermal conductivity, the core or middle temperature, the surface temperature and the surrounding air temperature, respectively.

As an example, table 2.1 was built according to eq. 2.9 for a thick glass fiber laminate. This table shows an estimation of the core temperature in thick laminates under the above mentioned 1D assumptions.

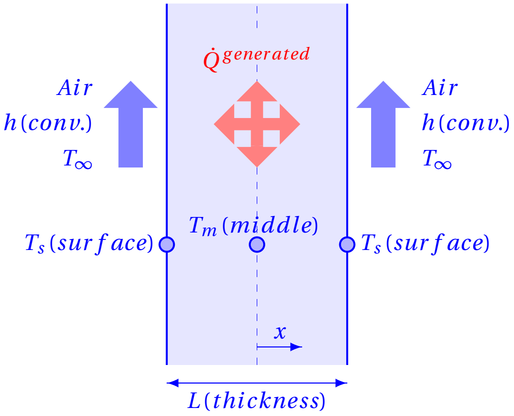

Figure 2.3: Plane wall with uniform heat generation (1D diagram).

Based on the 1D assumptions and the lumped capacitance method [118], it is possible to calculate the required time t_s to arrive to the steady state temperature profile. The lumped capacitance method assumes that the entire body is at the same temperature at each time step, so conduction is neglected. This leads to,

$$t_s = \frac{\rho \cdot (L/2) \cdot c_p}{h} \cdot \\ log_{10}\left(\frac{\dot{Q}^{generated} \cdot (L/2)}{h \cdot (T_\infty + 0.95 \cdot T_s) + \dot{Q}^{generated} \cdot (L/2)} \right) \tag{2.10}$$

where ρ is the density of the laminate, c_p is the specific heat capacity, T_s is the steady surface temperature from eq. 2.7 and $\dot{Q}^{generated}$ is the internal heat flow from eq. 2.5. However, the validity of equation 2.10 is limited to Biot numbers smaller than 1. When Biot numbers are higher than 1, equation 2.10 will lose accuracy. The Biot number (Bi) is a dimensionless index. This index describes the relevance of the thermal gradient in the body while the body heats or cools over time by convection. This number is described by equation 2.11 where h is the convective heat transfer coefficient, L_c is a characteristic length and k is the body conductivity.

$$Bi = \frac{h \cdot L_c}{k} \tag{2.11}$$

This 1D analytical solution offers only a rough estimate of the internal heating, but it provides an intuitive understanding of the problem. For a realistic geometry, for non-isotropic thermal and mechanical properties and for transient situations, however, a finite element (FE) approach is required to obtain more accurate results. This method is discussed in the following sections.

Max Load (MPa)	105	135	165	195	225
Min Load (MPa)	11	14	17	20	23
Load as a percentage of quasi-static tensile strength [%]	35	45	55	65	75
Thickness [mm]	$\Delta T_{max} = T_m - T_\infty$ **(°C)**				
2	0.5	0.8	1.2	1.7	2.3
5	1.3	2.1	3.2	4.4	5.9
10	2.7	4.4	6.6	9.2	12.3
20	5.8	9.6	14.4	20.1	26.7
30	9.5	15.6	23.3	32.6	*
40	13.6	22.4	33.5	*	*
50	18.1	30.0	44.8	*	*

Table 2.1: ΔT_{max} 1D analysis. Glass fibre coupon with main fibre direction at 90° w.r.t. loading direction, fatigue load ratio R=0.1, modulus 14 GPa, Max. tension 300 MPa, loss factor 0.05, frequency 0.5 Hz, conductivity 0.512 $\frac{W}{m \cdot {}^\circ C}$, convection 20 ($\frac{W}{m^2 \cdot {}^\circ C}$), ambient temperature 23°C. (*Unrealistic)

FE METHOD FOR HEATING FORECAST

In the finite element simulation of internal heating in fatigue, the mechanical calculation is related to the thermal calculation via the loss factor (eq. 2.13). In addition, the loss factor may vary per element due to ply orientation and damage evolution [117]. Hence for each element, a different loss factor might be used based on material and ply orientation.

The simultaneous study of the thermal and mechanical problem presents two problems: First, the time scales of the mechanical and the thermal phenomena are of a different order. While the mechanical time scale (defined by the cyclic loading frequency) might vary between 0.5 to 2 Hz, thermal stability is achieved in time scales from 10 minutes to 2 hours, therefore time steps differ by an order of two. Performing a thermal simulation before or after every mechanical simulation might result in excessive calculation efforts that are unnecessary.

The second challenge is that some FE solvers do not allow to impose an internal heat flow load that depends on the strain energy in each time step.

To circumvent these problems, the mechanical and thermal problem can be solved separately (uncoupled) using the following scheme [119] (see figure 2.4):

- Solve the mechanical problem for one loading cycle as a quasi-static simulation with a representative time step for the mechanical frequency.
- Extract the strain energy scalar field.
- Integrate the strain energy for a half cycle (elastic strain energy) and each element of the mesh, for all the tensor components.

$$W_{1-2}^{load-rev}(x,y,z) = \int_1^2 \sigma(x,y,z)\cdot d\epsilon,\ \forall x,y,z \tag{2.12}$$

- Multiply this result by the loss factor $\Phi(x,y,z)$ to obtain the internal heat generation. While $\Phi(x,y,z)$ is a function of spatial coordinates, in the current implementation it is considered spatially constant as Φ and chosen equal to the energy loss factors measured experimentally from the hysteresis cycles.

$$\dot{Q}^{gen}(x,y,z) = f\cdot\Phi\cdot W_{1-2}^{load-rev}(x,y,z) \tag{2.13}$$

- Build the thermal model with the same mesh.
- Import the internal heat generation as a volumetric internal heat load at each mesh element of the thermal model.
- Solve the thermal problem with a representative time step of the temperature evolution in comparison with the steady state arrival time.
- Perform the same steps for the next loading cycle type.

This method is based on the assumption that changes in the loss factor and changes in the strain energy do not affect the thermal problem significantly.

The method was implemented in the MSC Marc 2010 solver in which the strain energy density solution of the mechanical simulation is output to a report file. The input to the thermal simulation is generated with a Python code as a file with spatial coordinates and heat scalar values that can be translated to a volumetric heat load to the thermal model.

EXPERIMENTS AND SIMULATIONS

Temperature build up in thick laminates is driven by the internal volumetric heat generation described by eq. 2.5. The main factors in eq. 2.5 are the frequency, the loading ratio, the ratio of strain energy transformed into heat (Φ, loss factor) and the boundary conditions. In order to observe the variation in fatigue life with the heating effect, two different types of coupons, referred to as 'S20' and 'S77' coupons were tested in fatigue under different loading ratio conditions, testing frequencies and thermal boundary conditions.

TEST METHODS AND MATERIALS

Two different fatigue test configurations were experimentally tested and analysed with the FE method as follows:

- Compression fatigue tests on 30 mm thick coupons of geometry 'S77' with transverse reinforcement.

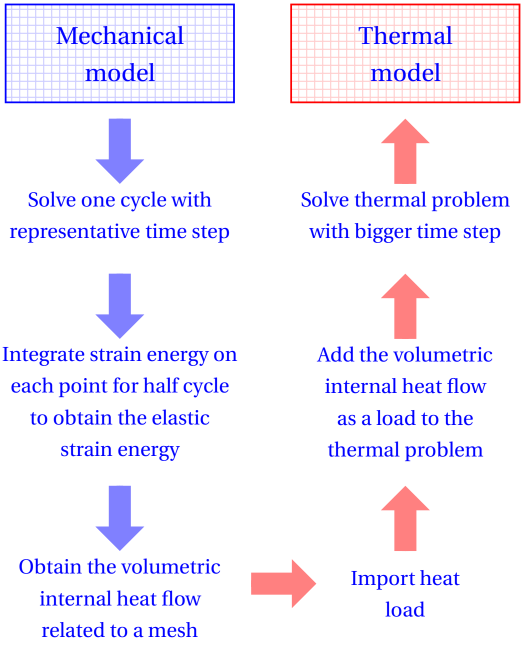

Figure 2.4: Heating temperature FE forecast method flow task diagram.

- Compression fatigue tests on coupons of ’S20’ geometry and 10 or 20 mm thickness with reinforcement at 0° w.r.t. loading direction.

The ’S77’ coupons were tested in fatigue at constant amplitude of force and a loading ratio $R = 10$ at frequencies of 0.25 Hz and 0.5 Hz in a 1 MN maximum load capacity hydraulic test frame. The specimens were gripped in the tab area and thus the test frame load is introduced to the specimen by shear loading. In a similar manner, the ’S20’ compression coupons 10 and 20 mm thick were tested in fatigue at $R = 10$ at a test frequency of either 1.5 Hz and 2.5 Hz. A third set of ’S20’ coupons was tested at 1.5 Hz, and the surface was covered by an insulation foam (conductivity $k = 0.023$ [W/m°C]) with the aim to reduce the heat generation disssipation into the atmosphere aproching a quasi-adiabatic state. All sets of coupons were tested in a 400 kN test frame in end loading compression test set-up.

In all experiments (except for the specimens covered in insulation material), surface temperatures were monitored with an IR camera, in order to compare experimental measurements with the model results. In addition the temperature was measured with a thermocouple at one side of the coupon (see figure 2.5 and figure 2.6).

The loss factors were measured during the tests based on the hysteresis areas described by the force and displacement signals. Sampling rates of 400 Hz were used on

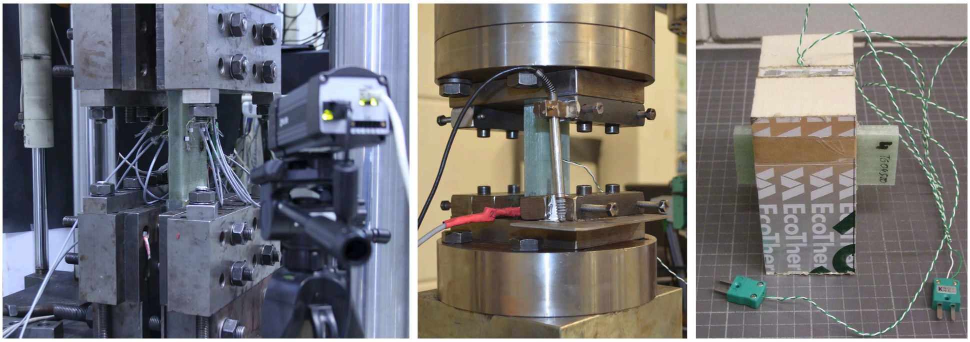

Figure 2.5: S77 coupons setup (left), 20 mm end-loaded coupons setup (middle), insulated end-loaded coupons setup (right).

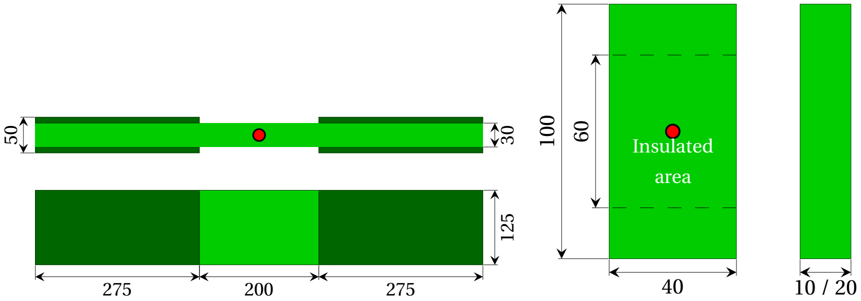

Figure 2.6: S77 coupon geometry (top). S20 coupon geometry (bottom). A red dot indicates the location of the thermocouple. Dimensions are in mm.

	Modulus E [GPa]			Poisson ν [-]			Shear modulus G [GPa]		
	11	22	33	12	23	13	12	23	13
UD	39.9	13.5	13.5	0.26	0.20	0.08	3.5	3.5	3.5
Biax	25.0	25.0	13.1	0.15	0.15	0.08	3.5	3.5	3.5

Table 2.2: Material properties used in FE analysis [14].

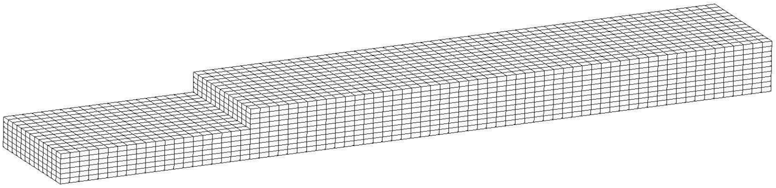

Figure 2.7: FE model mesh 11465 nodes and 8710 elements.

the recording of such signals.

Dynamic mechanical analysis (DMA) is a technique used to study materials where a low amplitude sinusoidal strain is applied and the stress in the material is measured while the temperature or the frequency changes. On the other hand, differential scanning calorimetry (DSC) is a thermoanalytical technique where the amount of heat difference required to increase the temperature of a sample and reference is measured as a function of temperature. Dynamical mechanical (DMA) tests and differential scanning calorimetry (DSC) tests were carried out in a range between -40°C and 100°C for UD 0° and 90° coupons manufactured with the same reinforcement and resin material. The storage modulus and DMA glass transition temperature T_g were defined according ISO 6721, and the DSC glass transition temperature T_g was defined according ISO 11357. The results of these tests are shown in figure 2.8 and figure 2.9. It can be observed that DMA glass transition temperatures are found of ca. 55°C. Note that the glass transition temperatures T_g, determined with the dynamical scanner calorimeter (DSC) method ranged between 80-85°C.

’S20’ coupons were manufactured from plates infused with a common wind energy epoxy resin (Hexion RIM 135) and glass fibre type E with 600 gr/m^2 non-crimp UD fabric. ’S77’ coupons were manufactured from plates infused with SP Prime 20 resin. An average fibre weight ratio of 70% and void contents less than 0.1% were measured.

FE ANALYSIS

The ’S77’ coupon was modelled using the above-described FE method to predict the material heating. The coupon geometry was reduced to one eighth with three symmetry planes imposed with displacement constraints. The shear loading carried out by the grips was modelled as an equivalent shear load distributed over the gripping surface. The material properties used in the FE analysis are shown in table 2.2, where the principal modulus correspond to strain gauge measurements carried out during the tests.

The mesh was based on Marc hex8 elements with 11465 nodes and 8710 elements (see figure 2.7), with a constant element size of 5 mm in length and 2.5 mm in height. The computational scheme followed in the FE analysis is described in section 2.3. The

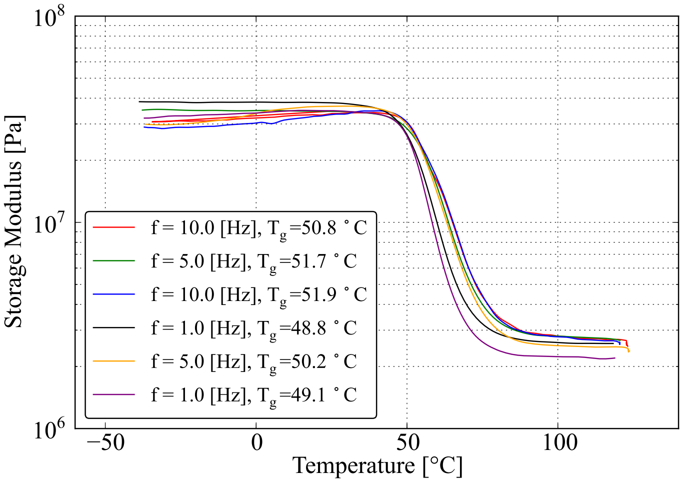

Figure 2.8: Dynamic mechanical analysis (DMA) tests for 0° oriented laminates between -40° to 100°C and 1 to 10 Hz (according ISO 6721).

stress and strain fields obtained from the mechanical FE model were processed with a Python code in order to calculate the strain energy dissipation for a whole cycle. The three directions stresses and strain components as well as the shear components were taken into account in order to calculate the total energy strain density. An average loss factor of 0.06 was used, which corresponds to the loss factors computed from measured hysteresis areas during the experiments. The material for the thermal model was defined as isotropic with a conductivity of 0.512 W/(m°C) and a specific heat of 1044 J/(kg°C). These values were calculated according to a rule of mixtures-based approach proposed by Cugnet [120]. The boundary conditions for the thermal model were defined as follows:

- A convection boundary condition at all the surfaces with no symmetry planes or gripping surfaces. A sensitivity analysis for different convection coefficient values was carried out between 5 to 15 $\frac{W}{m^2 \cdot {}^\circ C}$, using the guidelines from [121].

- In the gripping area, a contact resistance condition with a solid at 20°C was imposed. The value of the contact resistance was chosen to be $2 \cdot 10^4 \frac{m^2 \cdot {}^\circ C}{W}$ [122], after a sensitivity analysis for this value was carried out, showing differences in the temperature results not higher than 2 degrees for a contact resistance four orders of magnitude different.

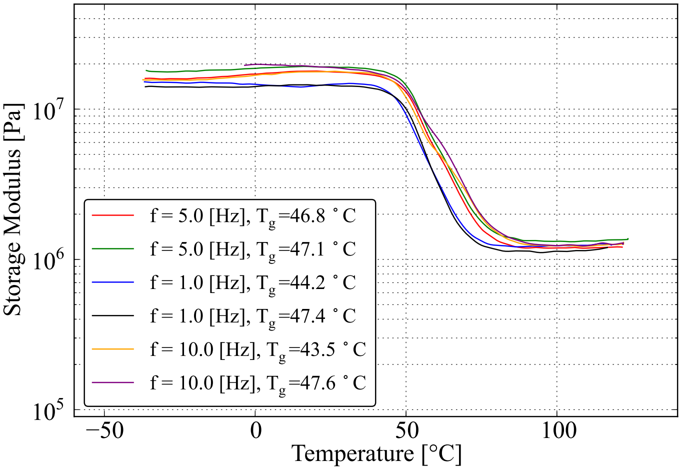

Figure 2.9: Dynamic mechanical analysis (DMA) tests for 90° oriented laminates between -40° to 100°C and 1 to 10 Hz (according ISO 6721).

RESULTS AND DISCUSSION

FATIGUE EXPERIMENTS

In the 'S20' and 'S77' fatigue tests it was observed that the surface temperature increase is mainly dominated by the maximum stress σ_{max} and the frequency. Core temperatures exceeding the surface temperatures are expected due to material heating. In case the temperature comes too close to the glass transition temperature, rigidity drops, potentially leading to increased damage.

'S20' specimens with fibres in loading direction of 10 mm thick were tested under insulated (quasi-adiabatic) and non-insulated conditions at 1.5 Hz (see table 2.3). A maximum surface temperature increase of 15°C was observed in insulated coupons tested at the higher σ_{max} cases. The temperature remained significantly lower than the glass transition temperature, and the fatigue lives were similar to the non-insulated specimens which exhibited a lower temperature increase, see the S-N curves of figure 2.10.

While 10 mm thick 'S20' coupons surface temperatures were significantly below the glass transition temperature and no change in fatigue life was observed, this was not the case for all 20 mm thick 'S20' coupons. Similar 'S20' coupons of 20 mm thickness were tested under insulated and non-insulated conditions at 1.5 Hz, and also under non-insulated conditions at a higher frequency of 2.5 Hz (see table 2.3). While non-insulated coupons tested at 1.5 Hz showed a maximum surface temperature increase of 17°C, the coupons tested at 2.5 Hz showed a maximum surface temperature increase of 25° C. More-

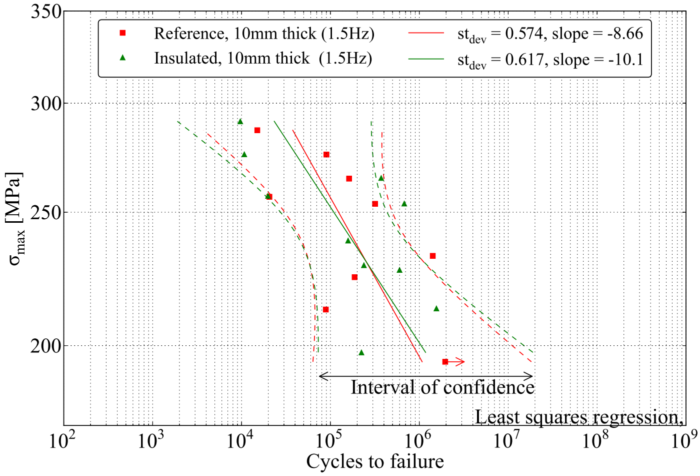

Figure 2.10: S-N curves (Insulated, non-insulated) 10 mm thick.

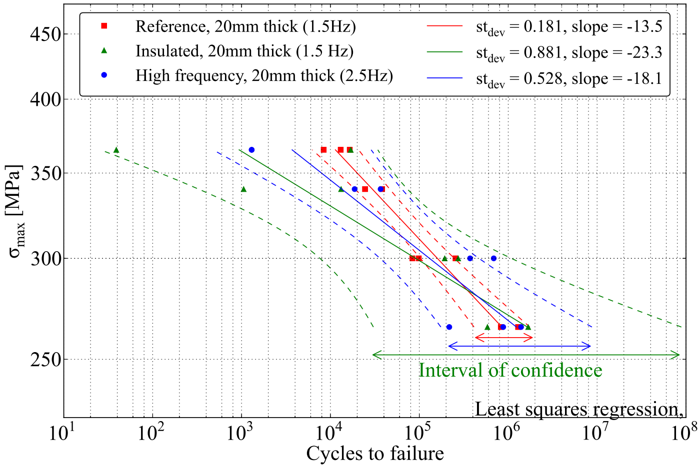

Figure 2.11: S-N curves (Insulated, Non-Insulated, High Frequency) 20 mm thick, interval confidence at 95 %.

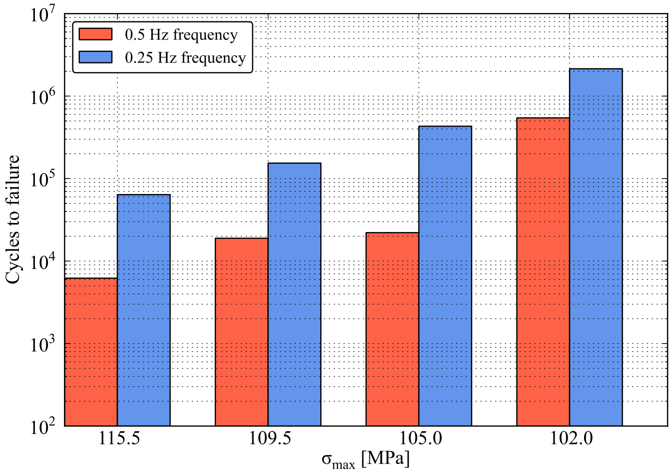

Figure 2.12: 'S77' 30 mm thick 90 degrees oriented tests at different frequencies.

over, the coupons tested under insulated conditions at 1.5 Hz showed a higher temperature increase of up to 33°C, which is closer to the operational range limit. The S-N curves (see figure 2.11) of the 20 mm thick coupons exhibit a strong variation for the high loading cycles. In both cases, the frequency increase or the application of the insulation resulted in an increase of the scatter and wider intervals of confidence. The observed change in fatigue life performance can be related to the increase of the coupon temperature since surface temperature and core temperature for high-frequency and insulated tests come close to the range of glass-transition temperatures of the matrix and can thus be expected to have an effect on the overall performance of the laminate.

Figure 2.12 shows 90 degrees oriented 30 mm thick coupons of type 'S77', tested at dif-

Thick-ness	Freq.	Insu-lated	Orien-tation	Surface ΔT_{max}	Φ_{mean}
[mm]	[Hz]	[-]	[°]	[°C]	[%]
10	1.5	No	0	8	2.5 to 4
10	1.5	Yes	0	15	2.5 to 4
20	1.5	No	0	17	2.5 to 4
20	2.5	No	0	25	2.5 to 4
20	1.5	Yes	0	33	2.5 to 4
30	0.25	No	90	16	5.5 to 6.5
30	0.5	No	90	40	5.5 to 6.5

Table 2.3: Summary table of experimental data.

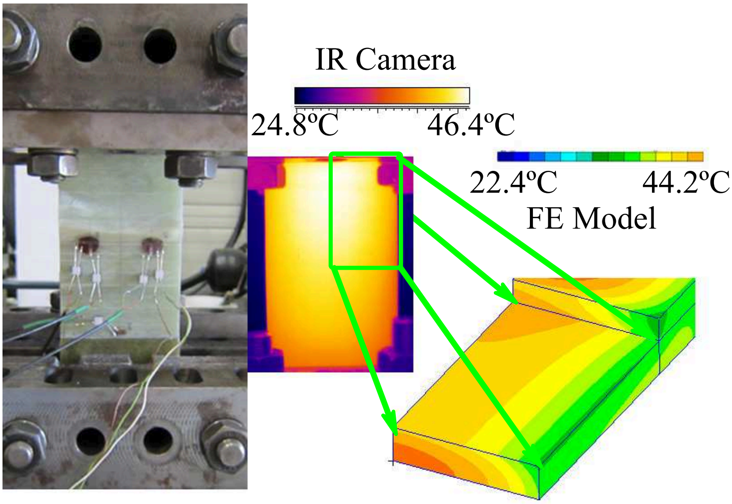

Figure 2.13: 'S77' coupon temperature field and FE model ($h = 10\ \frac{\text{W}}{\text{m}\cdot{}^\circ\text{C}}$).

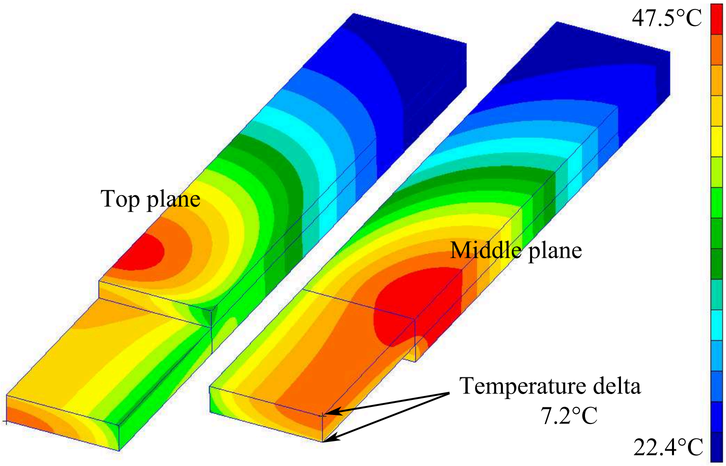

Figure 2.14: 'S77' temperature field in the steady state (convection factor 10 $\frac{\text{W}}{\text{m}^\circ\text{C}}$, Units: °C, 0.5 Hz 10.000 cycles, model show from two sides).

Freq.	Convection coeffcient	Temp. side FE model	Temp. surface FE model	Temp. middle 1D theory	Temp. experimental IR image
[Hz]	[W/m°C]	[°C]	[°C]	[°C]	[°C]
0.25	5.	37.	41.	33.	34-36
	10.	28.	31.	27.	
	15.	25.	27.	25.	
0.5	5.	55.	61.	46.	45-47
	10.	36.	42.	34.	
	15.	30.	35.	30.	

Table 2.4: Comparison between analytical, FE model and experimental data.

ferent maximum stresses σ_{max} and at two different frequencies, 0.25 and 0.5 Hz. While the mentioned testing frequencies did not influence thinner coupons fatigue life, 30 mm thick coupons tests showed that fatigue life was reduced one order of magnitude by doubling the frequency. During the test, differences in surface temperatures between both frequencies of around 15°C to 20°C were recorded, with maximum surface temperatures close to 40-50°C. Based on these surface temperatures, core temperatures up to 55-65°C were calculated. As the dynamical mechanical test showed, this is in the same range as the glass transition temperature, leading to the expectation of temperature-induced stiffness reduction or damage development. The glass transition temperatures measured with the DMA seem more relevant for the explanation of the influence of temperature on fatigue behaviour than the T_g values from the DSC method.

TEMPERATURE ANALYSIS WITH FE METHOD

In order to validate the FE method (see section 2.3) the temperature distribution during a fatigue tests was evaluated for 'S77' coupon type tested at 105 MPa. The temperature distribution was modelled and compared with the experimental data.

The temperature predicted 'S77' coupon model rises up to 27.5°C above the ambient temperature due to the fatigue heating process. Such temperature gradients agrees with the experimental observations carried out with the thermo camera (see figure 2.13 and table 2.4). The FE method models the temperature increase with a volumetric heat that is equal to the fraction of the strain energy dissipated, as defined by the energy loss factor Φ. This assumption was validated since the energy loss factor used in the model corresponds to the energy loss factor measured during the experimental tests with the hysteresis areas method.

By calibrating the results with the convection coefficient (h), it was possible to find an agreement between the experimental temperatures and the modelled temperatures with maximum difference of ±2°C. Table 2.4 shows the computed temperatures for three different convection coefficients between 5-15 $\frac{\mathrm{W}}{\mathrm{m}\cdot{}^{\circ}\mathrm{C}}$ at both testing frequencies. The temperatures on the surface area are compared with the IR images measurements. The best match with the experimental temperatures in the steady state and the transient state arrival time is for a convection coefficient of 10 $\frac{\mathrm{W}}{\mathrm{m}\cdot{}^{\circ}\mathrm{C}}$. This coefficient is in the order of the ones reported in the literature [118] for a non-forced wall convection case.

The temperature difference between the middle section and the outer section of the model is around 7°C, which is of the same order of magnitude as the analytical model results. Figure 2.14 shows the temperature obtained from the model. Such a full-field temperature overview can help test design in terms of selection of the best location of the thermocouple. Therefore, and because of the large temperature gradients, the IR camera was preferred over using thermocouples as temperature inspection method. In both cases, the surface temperature gradient described by the model (see figure 2.14) and the IR experimental recordings (see figure 2.13) shows that higher temperatures occur in the gripping area next to the measurement section. This is related to the stress concentrations in that area due to the geometry and clamping.

The model in figure 2.14 shows cross sections with core temperatures close to 50°C for the ’S77’ coupons tested at 0.5 Hz. According to the DMA results (see figures 2.8 and 2.9), the stiffness reduction associated with the glass transition temperature event occurs at 50°C. While the model shows cross section temperatures close to the glass transition temperatures for test frequencies of 0.5 Hz, the same model predicted maximum temperatures 12°C lower than the glass transition temperature at a test frequency of 0.25 Hz. Therefore the model indicated that self-heating a reasonable explanation of the reduction of the fatigue performance observed for the ’S77’ coupons during the experiments between test frequencies of 0.25 and 0.5 Hz (see figure 2.12). In this way, the FE method allows to tune safely the frequency of the tests when the interaction between the heating due to fatigue and the glass transition temperature limits downgrade the material performance.

CONCLUSIONS

Fatigue tests for laminate thicknesses between 10 to 30 mm are reported at different frequencies and thermal boundary conditions (tests on thermally insulated specimens or specimens without thermal insulation) were carried out for GRP laminates. A change in fatigue performance was observed in 20 mm and 30 mm thick laminate fatigue tests, for temperature increases that were related to the test frequency or thermal boundary conditions.

A finite element method to analyse the temperature distribution in the thick laminates fatigue test was described, linking the hysteresis area loss factor and the strain energy density with the internal volumetric heat that cause the material heating. This assumption was validated, since the temperatures were accurately forecasted using the loss factors measured experimentally during the tests with the hysteresis areas described by the load and displacement signals.

The 30 mm thick coupons tested in fatigue were modelled be means of the FE method and compared with the experimental observations of the IR camera. According to this model, the coupons tested at high frequencies showed temperatures close to the glass transition temperatures in comparison to the coupons tested at lower frequencies. This explains the premature failures observed in the experimetal tests due to the heating generated during fatigue.

It is concluded that the methodology was confirmed to be accurate in comparison with the experimental observations. It allows to forecast the temperature raise due to fatigue, and to compare it versus the glass transition temperatures.

3

THICKNESS SCALED COMPRESSION TESTS

To determine the properties of thick laminates and compare them with thin laminates is necessary to tests them first. However, coupon geometry and test conditions influence the final static and fatigue test results and might blur the conclusions. This chapter describes the design and engineering of scaled thick laminates compression test. Static and fatigue test on 4, 10 and 20 mm thick coupons are reported and discussed.

INTRODUCTION

Concerns about size effects were already reported in the 15th century, when it was suspected that among cords of equal thickness the longest is the weakest [15]. Since then until our times different size effects in composites and other materials have been studied. In Bažant's [16] review on size effects on structural strength, the size effect in solid mechanics is understood as the change of the nominal strength of the structure when geometrically similar structures are compared.

In review papers by Zweben [17], Sutherland's et al. [19] and Wisnom [32], evidence and supected causes for the existence of size effects are reported. The causes reported in those references are the influence of test configuration, the manufacturing defects, the difficulty of scaling fibers and the scaling of ply thicknesses.

Moreover, Wilkins [26] reviews the nature of scaling effects with special emphasis on the use of the Weibull theory, which states that the probability of occurrence of defects increases as volume increases. Weibull theory is also used to represent the inherent scaling effect that composites exhibit due to the impossibility of scaling fibre diameters and geometries. Wang [27] defends that there is a dependence of material strength on volume

---

This chapter was extracted integrally from [123], with omission of parts that discuss the influence of manufacturing process, which can be found in Section 5.4 of this thesis.

that should be understood as a scaling effect of material properties.

Regarding scaled compression tests, Camponeschi [23] reported the effect of the thickness of carbon reinforced polymer (CFRP) laminates up to 7 mm thick concluding that in most cases there is a drop in the compression strength with thickness increase, which can be related to the material quality or testing side effects. Bing [25] studied the size effect on end loading compression coupons for off-axis tests, observing a decrease of strength with an increase of thickness. This strength decrease was found to be more pronounced when the off-axis angles are close to 0 degrees.

Hsiao [124] performed static tests on unidirectional (UD) CFRP coupons up to 10 mm thickness observing no significant reduction of the ultimate strength for increasing thickness and a reduction of the coefficients of variation. On the contrary, Lee and Soutis [125] performed several series of static thickness scaled open hole compression tests on CFRP laminates with thicknesses up to 8 mm, observing a reduction of the ultimate strength. However, in these tests, instead of scaling the geometry as the thickness increases, the same geometry with different thicknesses was used in all the cases. In a similar manner, un-scaled CFRP coupons were statically tested by Baldini et al. [126] with thicknesses up to 5.5 mm showing a decrease of the ultimate stresses. In addition, Cordes [127] performed a series of compression tests on 10 mm thick specimens with different cross-ply lay-ups, where it was concluded that the quasi-static behaviour of the cross ply composites is dominated by the zero degree layers.

Common practice to determine static design limits of composite glass fibre reinforced parts such as wind turbine blades is to reduce the test material characteristic values (stresses and strains) to a probability of failure of the 5% according to a normal distribution. Later such characteristic value is divided by a safety factor in order to obtain the static design limits. Such safety factor can be obtain from previous experimental tests [52] or standards such as Germanischer Lloyd guidelines [3].

A similar approach is used to determine fatigue limits with standards such as Germanischer Lloyd guidelines [3]. To predict durability due to fatigue a Miner's rule or a residual strength model [53] is used, in conjunction with the Goodman diagram [54, 55]. It allows to predict the cycles to failure as a function of mean stresses and amplitude stresses. Such models are constructed based on test material characteristics values (stresses and strains), S-N curve slopes and safety factors defined by the standards.

In both static and fatigue design limits, the test material characteristic values are based on specimens which are not thicker than 4 mm. Therefore, scaling effects, manufacturing effects and aging effects that are present in the final structural behaviour are considered via safety factors.

Taking into account that limited references are available in literature related to static scaled compression tests on composites, and even less in the case of fatigue properties,

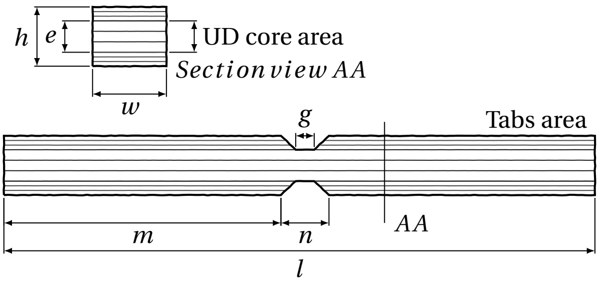

Figure 3.1: Parametric coupon geometry.

the aim of this work is to study the size effect in static and fatigue properties with thickness scaled compression tests on unidirectional glass fibre reinforced polymers (GFRP). Measurements are compared with the reduced fatigue capacity given by design guidelines as a reference.

MATERIALS AND METHODS

The aim of this study is to investigate the influence of thickness on compressive failure of unidirectional GFRP. To ensure that the desired failure mode occurs in all cases, the experiments are engineered with care. Special attention is paid to the coupon geometry, the manufacturing process and the test setup.

COUPON GEOMETRY

The coupon geometry is described by the parameters shown in figure 3.1. The specimen can be loaded in three different ways: by end loading (ASTM D695, DIN 65375), by shear loading (ASTM D3410) or combined loading compression (CLC) setup which is a combination of the first two (ASTM D6641). In this work, a CLC setup is considered, where the total load exerted by the test frame actuator is divided into a shear load and an end load according to a distribution coefficient that varies with the clamping pressure. In order to pre-dimension the geometry, four different failure modes (see figure 3.2) were considered: compression failure in the gauge section, shear failure in the tab section, crushing at the end section and buckling of the gauge section. Of these, the first is the desired failure mode.

Compression failure of the gauge section is the design failure parameter, and for a glass fibre UD composite a maximum stress of 800 MPa was considered. Thus for a certain thickness e and a certain width w the main load F_{load} required can be calculated. The shear failure mode in tab section was designed for a maximum shear τ_{tab} of 10 MPa, thus the tab length (m) can be dimensioned as,

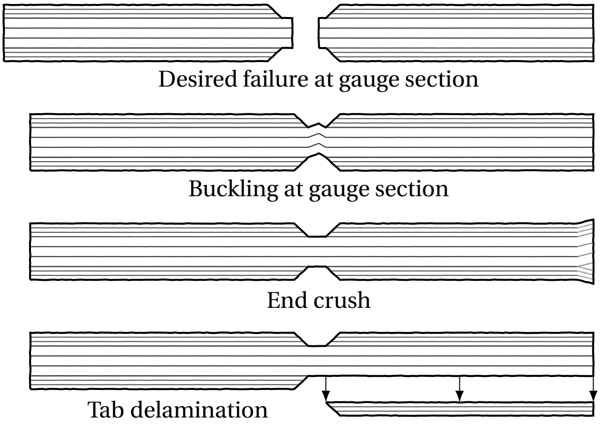

Figure 3.2: Failure modes considered in the analytical geometry pre-dimension.

$$m > \frac{F_{load}}{\tau_{tab} \cdot w \cdot 2} \tag{3.1}$$

The end loading failure mode is driven by the bearing stress $\sigma_{bearing}$, which was considered as 200 MPa for dimensioning purposes. Thus the tab thickness (t) can be sized as,

$$t = \frac{h-e}{2} > \frac{1}{2} \cdot \left(\frac{F_{load}}{\sigma_{bearing} \cdot w} - e \right) \tag{3.2}$$

The buckling failure mode was considered according to the Euler formula, in such way that the gauge section thickness exceeds the critical thickness by at least 20%. Based on these analytical failure modes, the geometry was pre-dimensioned and refined with a FEM parametric analysis [128].

Such FEM parametric analysis showed that due to the combined loading, a stress gradient occurs through the thickness where the middle layers are on lower stresses levels than the outer layers. Assuming that a maximum stress allowable is equal for each layer, stresses between the outer layers and the middle layers should be as even as possible in order to promote a synchronized failure through the gauge section thickness, leading to higher failure forces.

The increase in the coupon length (parameter l) does not influence the behavior of the gauge section, but does reduce the mean shear stress between the tab and the UD core.

The increase in the gauge section length (parameter g) reduces the through-thickness stress gradient. In the same way the increase in parameter n related with the tab taper angle or the reduction of the tab modulus, reduces the stresses gradient through the thick-

	l	m	n	g	e	h	w
Geometry	[mm]	[mm]	[mm]	[mm]	[mm]	[mm]	[mm]
1 (S21)	140.0	65.0	10.0	3.0	4.0	8.0	10.0
2 (S22)	400.0	187.5	25.0	10.0	10.6	20.0	25.0
3 (S23)	760.0	362.5	35.0	15.0	20.0	32.6	55.0

Table 3.1: Scaled coupon nominal dimensions.

ness. The increase in the gauge section length and the reduction of the tab taper angle, both increase the possibility of the desired failure due to the cross sectional main stress. However, the freedom to select these parameters is limited by the risk of buckling of the gauge section.

The load distribution coefficient between the end load and the shear load implies a small variation of all indicators. However it has to be taken into account that in the real test case the load introduction by shear in a clamp is not as evenly distributed as in the model due to surface tolerances, surface roughness and grip marks. Therefore, a certain amount of end loading cancels the possibility of slippage in the grips and allows to freely setup the grip pressure. Thus, combined loading was the preferred choice.

The parameter h related with the tab thickness shows that higher tab thicknesses influence the stress gradient through the thickness. A tab thickness increase promotes higher probability of failure in the middle cross section and reduces the influence of the clamping pressure in the tab-core interface.

Final coupons (see figure 3.6) were obtained from a FEM design process as described above and dimensions are shown in table 3.1. Dimensions obtained from the design process were accommodated, due to practical restrictions, to the closer possible dimensions that agree with a direct up-scaling. Since the type of fabric and the fabric grams per square meter determines the layer thickness, the final coupon thickness is the number of layers multiplied by the average layer thickness. Therefore, in practical terms it was difficult to arrive at an exact scaling of the parameters related with the thickness. In case of parameter g scaling was limited in order to avoid buckling of the external layers, since failure due to buckling is not desired.

MANUFACTURING PROCESS

The manufacturing process was developed aiming to reduce the manufacturing influence when coupons of different sizes and thicknesses were produced. For connection between the core and the tabs, adhesive bond would be the most common choice. However, as the scale of the coupons increases, the adhesion surface also increases, which presents some

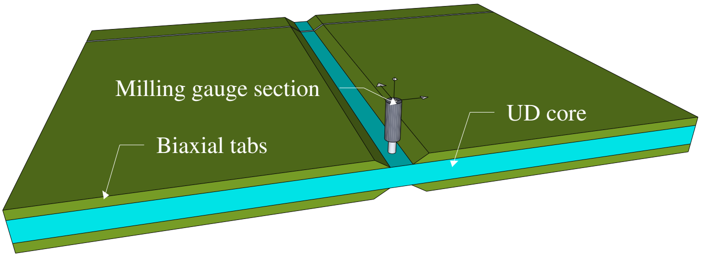

Figure 3.3: Plate milling into coupons.

processing challenges in order to keep the quality of the adhesive surface free of voids. Instead of bonding the tab, coupons were therefore manufactured at once with integrated tabs that were milled to create the gauge section (see figure 3.3).

Vacuum infused plates were manufactured with an epoxy resin commonly used for wind energy applications (Hexion RIM135). The core material was a UD glass fibre type E of 600 gr/m^2 non-crimp fabric, and the tab material was a biaxial glass fibre type E of 400 gr/m^2 non-crimp fabric. For all manufactured plates, fibre content and glass transition temperature were measured. Averaged fibre weight ratios were 70% (averaged fibre volume contents of 53%), void content was under 0.1% and DSC glass transition temperature (T_g) was around 80-85°C.

Panels of 4 and 10 mm thickness were cured with a curing cycle prescribed by the resin manufacturer for the epoxy resin. The curing cycle was divided into two main stages. The first stage was the hardening stage, where the exothermal reaction of the resin takes place with a setup mould temperature of 45°C. The second stage was the post-curing stage, where the resin finalize the curing process with a setup mould temperature of 80°C. For the panels dedicated to 20 mm thick coupons, the initial hardening stage mould temperature was reduced to 30°C to avoid excessive temperatures due to the exothermic reaction and the thickness of the plate. Temperatures through the thickness were measured with embedded thermocouples during the curing. From these temperatures the maximum heating rates during the hardening stage ($max(dT/dt)$) were computed.

The plates were milled in thickness direction to create the gauge section and coupon shape. The shape of the coupon was milled over the width of the plate and finally cut lengthwise with a diamond saw. In this way, all geometrical tolerances could be referenced to one origin, since it was performed in a 3D axis milling machine.

While milling of the gauge section, a layer of material in the order of microns is damaged by the milling blades. To study the impact of this effect, the 4 mm thick coupons were compared in a fatigue test with coupons with bonded tabs which were not milled. A similar comparison was not carried out for higher thicknesses, since the hypothetic fatigue life reduction that might be caused by the milling process is more significant for thinner coupons than for thicker coupons. Therefore, R08 type [14] rectangular 4 mm thick UD coupons with 20 x 20 mm gauge section and bonded tabs of 55 mm in length were prepared with the same material and manufacturing process for comparison purposes.

TEST SETUP

Coupons with 4, 10 and 20 mm gauge section thick were tested in static tests and in fatigue tests at a stress ratio $R = 10$. The 4 mm coupons were tested on an MTS servo hydraulic 100 kN test frame, static tests were performed in a CLC fixture according to ASTM D6641 and fatigue tests were performed with the standard machine clamping system. Coupons of 10 and 20 mm thickness were tested on 400 kN and 1 MN test frames respectively equipped with an assembly of clamping steel plates and hydraulic clamping (see figure 3.5).

Static tests were carried out at a test speed of 1 mm/min. Fatigue test frequencies were reduced as the thickness increased in order to minimize the influence of internal heating [110]. Coupons were monitored with thermocouples and infrared (IR) cameras. A frequency of 2 Hz was used for the 4 mm thick coupons, 1 Hz for 10 mm and 0.5 Hz for 20 mm thick coupons, which was sufficient to avoid surface temperatures higher than 30°C.

The 10 and 20 mm coupons were instrumented with cross gauges in the four gauge section faces in order to measure the elastic modulus in the outer surfaces and in the middle axial section (see figure 3.4). The use of cross gauges enabled the measurement of Poisson coefficients ν_{12} and ν_{13}.

RESULTS AND DISCUSSION

STATIC TESTS RESULTS

Thickness scaled static tests were carried out in a combined loading setup. It was observed that the clamping pressure in the tests has a strong influence on the final ultimate stresses. For example, figure 3.7 shows an influence of the grip pressure on the ultimate stress in the 4 mm thick coupons. Therefore, different tests were carried out to find the optimal pressure at which the highest ultimate stresses are found. 4 mm thick coupons showed that the optimal clamping pressures was around 17.9 MPa (see figure 3.7). In the case of 10 mm and 20 mm thick coupons the clamping forces were determined according to this clamping pressure and the tab areas. In addition tests with modified clamping

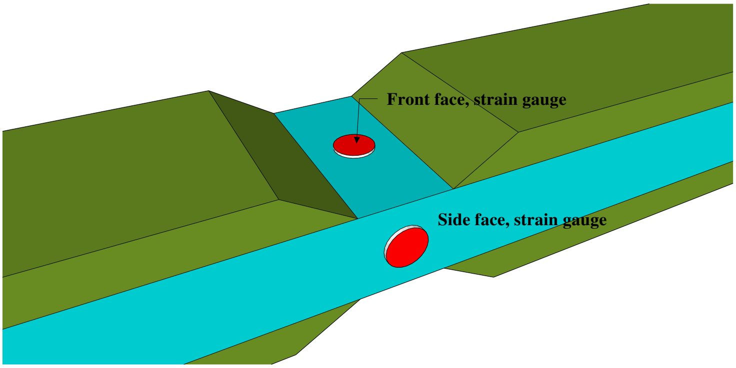

Figure 3.4: Strain gauges setup for 10 and 20 mm thick coupons.

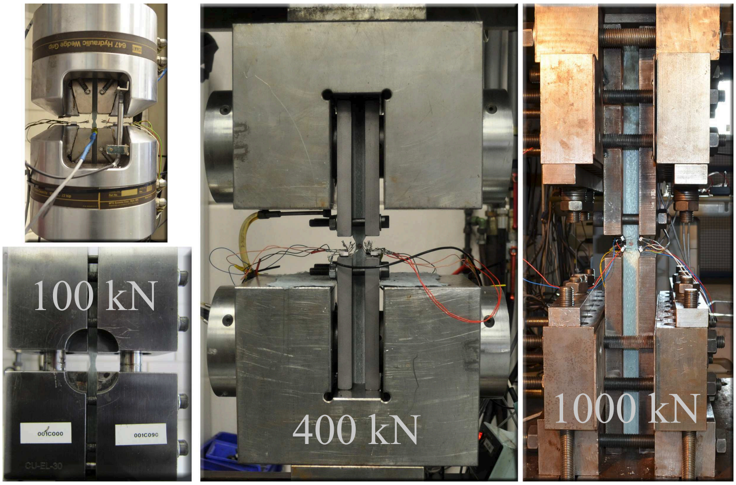

Figure 3.5: Test setup with 100 kN, 400 kN and 1 MN test frames.

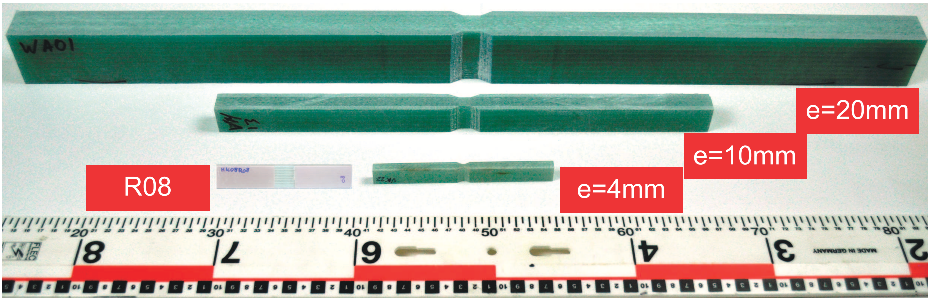

Figure 3.6: Thickness scaled coupons with integrated tabs and R08 coupons with bonded tabs.

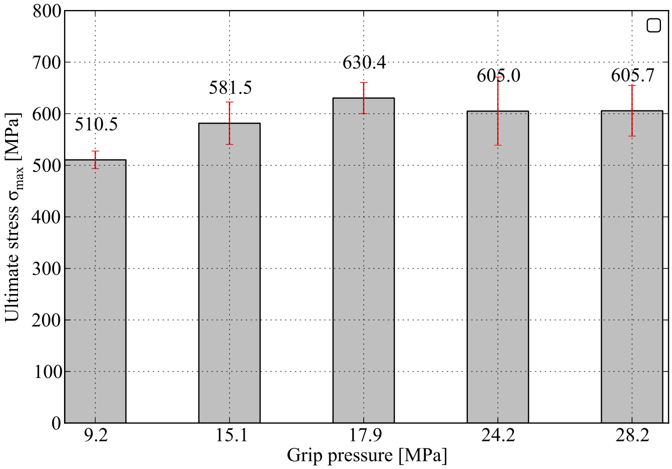

Figure 3.7: Ultimate stress versus grip pressure. 4 mm thick coupons. Number of coupons per pressure N=5.

pressures and bolt torques were carried out in order to ensure the right setup at the different thicknesses.

Static tests force versus displacement curves for the three thicknesses are shown in figure 3.8. Such curves show no remarkable load drops, but small peaks caused by the relocation of the coupon at the grip. In addition, no visual damage was observed until failure. Failure occurred at maximum force, with a rapid collapse of the cross section and a force drop larger than 5 %. Ultimate stresses were calculated dividing the maximum force by the cross-sectional area. In figure 3.9 it is shown how the ultimate stresses describe a slight enhancement with thickness and a small reduction of the coefficient of variance (COV) when the clamping pressure is optimal. This behaviour agrees with Hsiao [124] finding in CFRP static compression tests which showed no significant reduction of the ultimate stresses as well as a reduction of the COV. On the other hand, when the clamping pressures are not optimal, strong reductions in the ultimate stresses can be observed (see figure 3.9) which are related to the testing configuration rather than to scale effect. Such testing configuration phenomena and the lack of scaling of the tab dimensions might explain the size effect reported by Camponeschi [23] and Bing [25].

Because the 10 mm and 20 mm thick coupons were equipped with cross strain gauges on the front faces and on the side faces (see figure 3.4), the elastic modulus and Poisson ratios in the 12 and 13 planes were measured. While strain measurements at the front faces correspond to the outer layers of the gauge section, strain measurements at the side faces correspond to the middle layers of the gauge section. When strain measurements

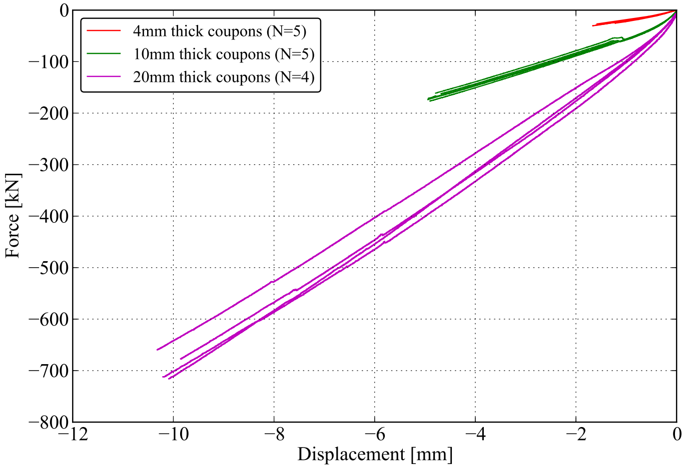

Figure 3.8: Static test results. Force versus displacement curves.

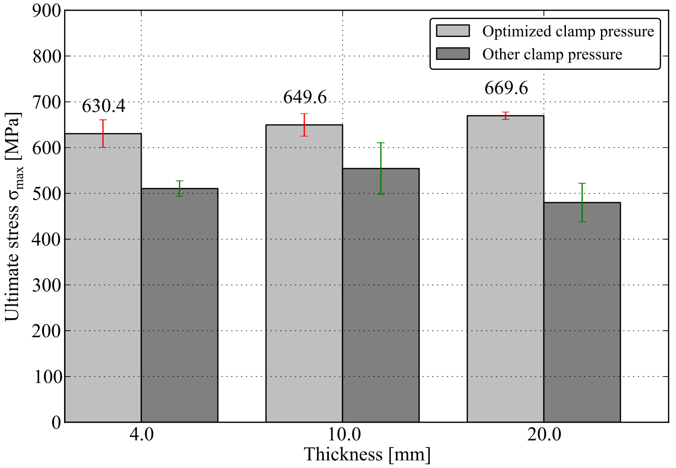

Figure 3.9: Static test results. Optimal and other clamping pressures. Numbers of coupons per pressure and thickness N_{4mm}=5, N_{10mm}=5 and N_{20mm}=4.

e [mm]	F_{max} [kN]	δ_{max} [mm]	σ_{max} [MPa]	E_{front} [GPa]	E_{sides} [GPa]	ν_{12} [$-$]	ν_{13} [$-$]
Reference	-	-	**546.9** (11.8%)	39.0 (11.6%)	-	-	-
4.0	28.1 (7%)	1.5 (11%)	**630.4** (5%)	-	-	-	-
10.0	169.1 (4%)	4.9 (3%)	**649.6** (4%)	36.3 (12%)	46.1 (18%)	0.283 (12%)	0.198 (21%)
20.0	691.4 (4%)	10.1 (2%)	**669.6** (1%)	41.9 (14%)	49.0 (5%)	0.235 (8%)	0.204 (14%)

Table 3.2: Thickness scaled static properties. Values between parentheses are the COVs. (δ: displacement, σ: stress, E: elastic modulus, ν: Poisson coefficient). Reference: average of 136 coupons with different geometries for the same material [14].

from the outer and middle layers were compared, it was observed that outer strains were 15% to 20% larger than middle strains. This variation also explains the difference between the modulus measured in the front faces and the side faces (see table 3.2) and agrees with the FEM results where a stress gradient through the thickness was predicted. In addition, table 3.2 shows the Poisson ratios measured in the front and side surfaces, which correspond to the Poisson ratios ν_{12} and ν_{13}, showing similar values for both planes.

A reference ultimate stress available in the literature for the same material is shown in table 3.2. From the Upwind Optimat Database [14], measurements were considered from 136 coupons tested in compression with different geometries for the same material and thicknesses below 5 mm. The average ultimate stress of these coupons is 546.9 MPa with a standard deviation of 64.5 MPa (COV 11.8 %). The measured values found in the current study are in the higher end of the range of values in the Upwind Optimat Database.

FAILURE MODES

The failure mode and position of failure were investigated post-mortem. In figure 3.10 the different failure modes of the coupons are summarized, as well as the failure positions according the ASTM D6641. While in the static tests the percentage of failures modes is evenly distributed between through-thickness and brooming (see figure 3.12), in the fatigue tests the through-thickness failure mode is dominant. No end crushing failures were observed in any of the tests.

Similar distributions of failure modes were observed for all coupons thicknesses, which suggest equivalent behaviour between the different scaled geometries (see figure 3.11). This was the main reason why the coupons geometry were scaled rather than only

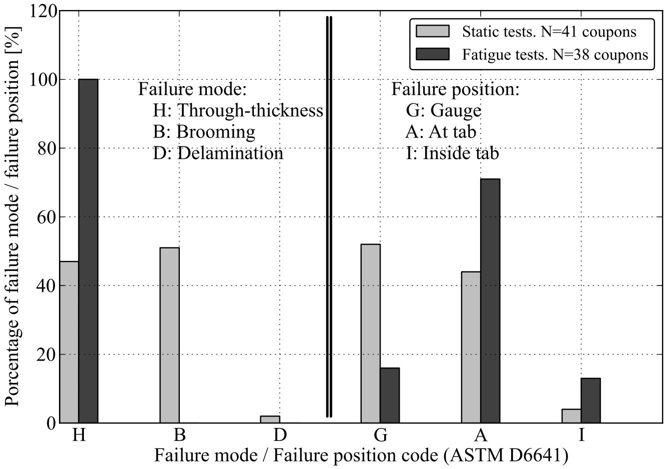

Figure 3.10: Failure modes and position statistics for 4, 10 & 20 mm.

the thickness, in order to have equivalent stress gradients independently of the thickness for a fair evaluation of the thickness effect.

A total of 91% of the coupons failed in the gauge section or at the tab, both of which failure cases are accepted by the standard. The remaining 9% of the coupons failed inside the tabs. Measurements from these coupons were discarded. Figure 3.10 shows that, while in the case of the static test the failure position is evenly distributed at the gauge and the tab, fatigue tests show an increase of failures at the tab and a slight increase of failures inside the tab.

Due to the in-plane shear stresses between the tab and the core, fatigue tests exhibited a partial delamination of the tabs, which did not propagate to more than 15% of the total tab length in the worst cases. The fact that none of the coupons with integrated tabs showed a total delamination of the tabs, which would invalidate the test, is an improvement in comparison with previous experiences of coupons with bonded tabs, in particular for thick gauge section coupons [9].

In all cases failure was instantaneous and catastrophic and were accompanied by an acoustic event. Matrix cracking, fibre compressive failure and micro-buckling are possible triggers of the failure mechanism. However, in order to investigate the failure mechanism, techniques such as high speed photography must be employed.

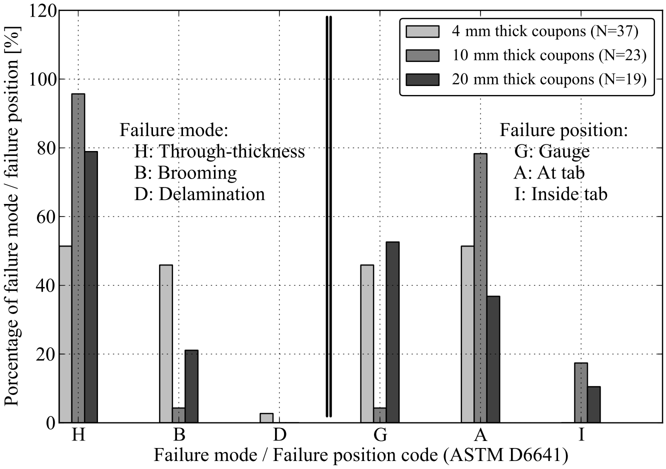

Figure 3.11: Failure modes and position statistics for 4, 10 & 20 mm. Chart by thickness.

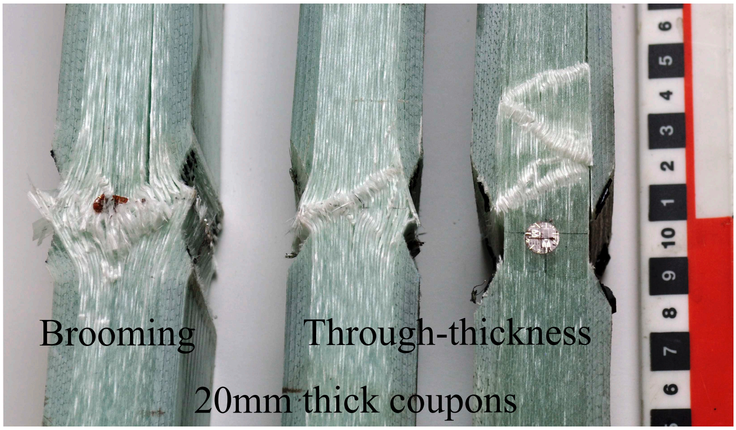

Figure 3.12: Failure modes photos in 20 mm thick coupons.

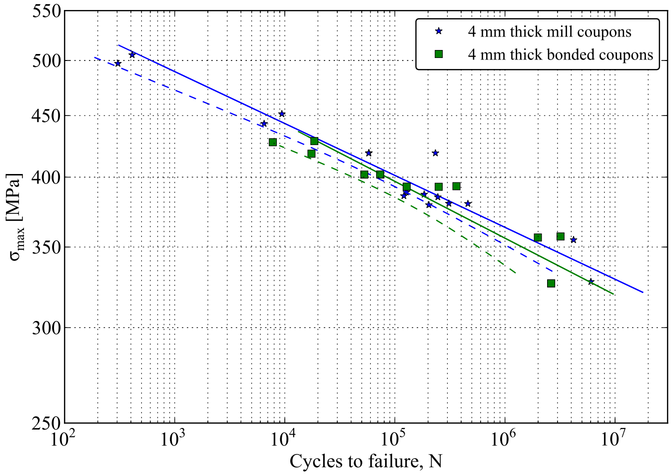

Figure 3.13: 4 mm thick coupons with bonded tabs and milled gauge section. S-N curves (R = 10).

FATIGUE TESTS RESULTS

Figure 3.13 shows the S-N curves for the 4 mm thick coupons with bonded tabs and with milled gauge sections. Both S-N curves show a very similar behaviour both in terms of slopes, intervals of confidence (95 % level of confidence) and stress levels. The use of coupons with milled gauge sections in comparison with coupons with bonded tabs, allowed to perform fatigue tests at higher stresses levels and could be used in fatigue or static tests without modifying the geometry.

While the scaled static tests did not show a size effect in the ultimate strength, fatigue tests carried out for 4, 10 and 20 mm thick specimens showed a significant decrease in the fatigue life for increasing thickness. Figure 3.14 shows the S-N curves for the three different thicknesses, as well as the design S-N curve determined according to GL 2010. When the S-N curves for the three thicknesses are compared, a decrease in fatigue life with the thickness as well as an increase in scatter for increasing thickness is observed. However, the decrease in fatigue life with thickness does not seem to be proportional with the thickness, and in particular for the 20 mm thick coupons where the stress levels for the high cycles seem to be inconsistent with the static compressive strength. Recent tests on thick laminates [110] for the same material has shown that, the lamina properties through the thickness are not equal but showed a distribution through the thickness, and different thicknesses positions showed different fatigue life S-N curves in compression for a 60 mm thick laminate. According these findings, a plausible hypothesis that explains the reduction of fatigue life with the thickness is that static and fatigue compres-

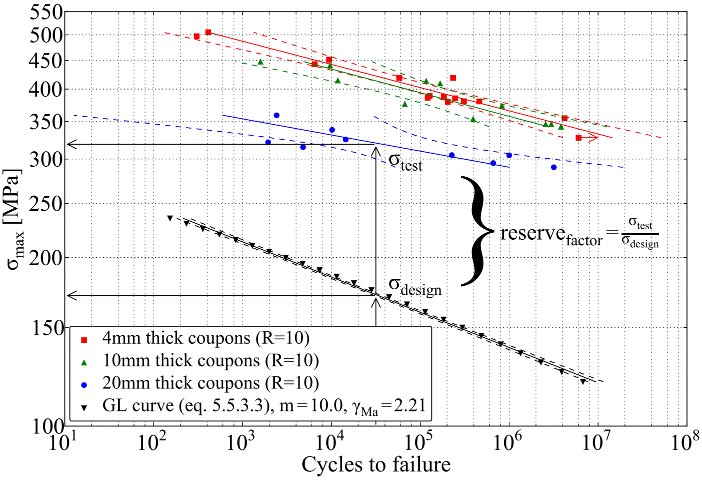

Figure 3.14: Thickness scaled S-N curves. Comparison with GL standard design curve.

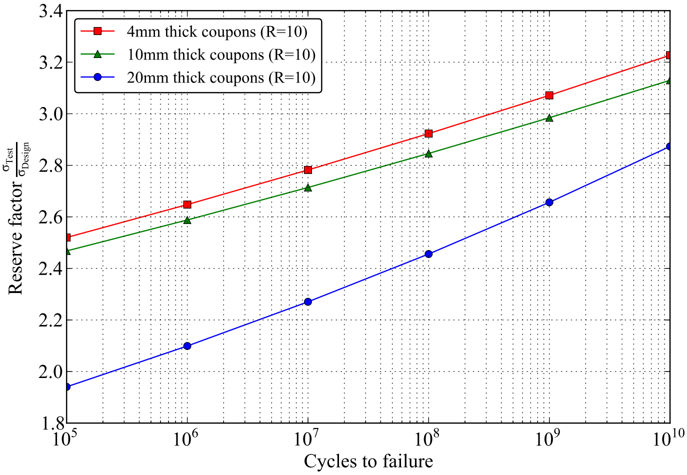

Figure 3.15: Reserve factor versus cycles to failure for each sample of coupons.

sion properties through the thickness are not equal, and failure is dominated by the worst scenario of fatigue life that can be found through the thickness.

Figure 3.14 shows the S-N curve determined according to GL 2010 guidelines (eq. 5.5.3.3 [3]), which was calculated for a slope $m = 10$, partial safety factors $\gamma_{Ma} = 2.21$, $\gamma_{Mb} = 1.63$ and the static compression properties from table 3.2 for the 4 mm thick coupons. Since the design S-N curve can be considered as a fatigue design limit for this type of material, and the S-N curves for each thickness correspond to the experimental limits, it is possible to define the reserve factor as the ratio between the experimental stresses and the design stresses for each number of cycles to failure (see figure 3.14). In figure 3.15 the reserve factors versus the cycles to failure are presented. The experimental curves do not cross with the design S-N curve since their slopes are higher. Therefore, the reserve factors follow a fail-safe incremental trend as the cycles to failure increase. In the worst scenarios (up to 20 mm thick), reserve factors values evolve from 2.0 for the lowest fatigue cycles to a reserve factor of 2.4 at 10^8 cycles. However based on this data, performance of very thick laminates might be doubtful.

CONCLUSIONS

In order to study the thickness effect, scaled coupons were designed aiming to reduce the test influence. Coupons were engineered with a parametric FEM analysis. A combined loading setup was chosen, and it was concluded that longer coupon lengths, higher tab thicknesses and acute tab angles increase the probability of failure in the gauge section.

Coupons were manufactured with partially milled integrated tabs in order to avoid the use of adhesive bonds. It was found that compression specimens with integrated tabs had similar fatigue lives to specimens with bonded tabs, while showing less premature tab failure. From a total of 79 coupons tested, only 9% of the coupons failed inside the tab. Brooming and through-thickness were the most common failure modes observed. It was observed that different clamping pressures can promote a decrease in the compression strength.

Static tests of scaled compression coupons for 4, 10 and 20 mm thick gauge sections were carried out. No size effect in the ultimate strength was observed in the static tests, provided that the optimal grip pressure was selected. The resultant ultimate stresses were compared with previous compression tests performed for the same material with different coupons geometries, resulting in a superior performance with average differences higher than 15%.

S-N curves did show a decrease in fatigue life for increasing thickness as well as an increase of the scatter. When experimental S-N curves were compared with the guideline design S-N curve, reserve factors larger than 2.0 were observed for the 20 mm thick coupons.

The decrease in fatigue life for thick specimens is suspected to be related to the manufacturing process and is further investigated in chapter 5.

◆

4

TEST SETUP AND SIZE EFFECTS IN TENSION TESTS

Different tension test configurations were investigated via FE analysis and experimentally tested to determine the test setup influence and size effects in tension. Furthermore, tension tests were carried out on laminates with thicknesses between 4 and 20 mm.

TENSION TEST COUPONS

Tension tests methods for UD composites are defined by different international standards namely ISO 527 and ASTM D3039. These standards consider coupons with a thin gauge section. However, if the gauge section thickness is increased without modifying the geometry a decrease in the overall performance of the thick laminate is found [9]. To avoid any undesirable test effect due to stress concentrations, different tension coupon geometries were studied using a parametric FE methodology. Thickness scaled static and fatigue experimental tests were performed, to investigate the size effect in tension tests.

Contrary to compression tests, tension tests are loaded in shear at the grip area where the tabs are located. Ultimate stresses, elastic modulus E and Poisson ratio ν are data that are obtained from a static tension test. Moreover, fatigue tests allow to plot S-N curves. Ideally, to study size effects the tests results should be independent of the coupon geometry for the same material and layup. Therefore, different coupon geometries, tab material and shapes (straight and dog bone) were considered.

The geometrical parameters of straight tension coupons are described by the parametric model shown in figure 4.1. The tension coupons considered in this chapter are composed of two parts: the UD core material and the tab material. Contrary to the compression coupon the tab length is divided in two parts and described with two parameters, the k parameter that corresponds to the grip area and the m parameter that gives the length over which the tabs are not gripped.

In a similar manner as the compression coupons (see chapter 3) two different failure modes are considered: tension failure in the gauge section and shear failure in the tab section. Analytically the shear failure mode in the tab section is determined by the maximum shear stress at the tab τ_{tab}, and the tab length $(m+k)$ can be dimensioned as,

$$m+k > \frac{F_{Total}}{2\cdot\tau_{tab}\cdot w} \tag{4.1}$$

where w refers to the coupon width, F_{Total} is the axial load applied by the test frame, τ_{tab} is the minimum tab shear strength and m, k are the coupon geometrical parameters (see figure 4.1).

GEOMETRICAL PARAMETERS

Tension coupon geometries were engineered with an FE parametric analysis using MSC Marc software.

PARAMETRIC FE DESIGN MODEL (STRAIGHT TENSION)

The parametric FE analysis was performed for the 4 mm thick coupons. Based on figure 4.1, one geometrical parameter per case was modified to analyse its influence (see table 4.1 and C.1). One-quarter of the coupon was simulated. Meshes with and without cohesive elements between the layers were evaluated to investigate possible delaminations close to the end of the tabs due to stress concentrations at that location. Models with around 4000 8-node hexahedral elements were considered.

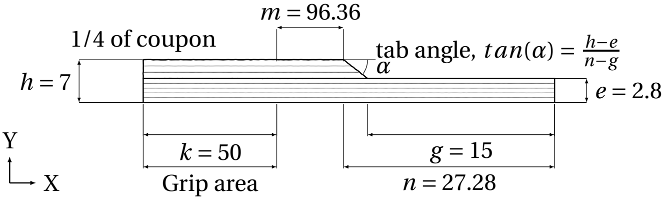

Figure 4.1: Tension coupon parametric geometry sketch (dimensions in mm).

Parameter	Cases	Values
g $[mm]$	0 / 1 to 6	15 / 30 / 60 / 120 / 160 /180
Tab angle α	0 / 7 to 10	18.9 / 5 / 10 / 25 / 30
h	0 / 11 to 14	5.8 / 7 / 8.8 / 11.8 / 14.8
Tab material	NA	UD / Biax / aluminum

Table 4.1: Parametric cases (see Appendix C)

The model is solved as a quasi-static problem, where the coupon is loaded up to a maximum load corresponding to 1000 MPa at the gauge section (surface between point 15-14 in figure 4.3). Furthermore, a clamping surface grip pressure of 200 bars along the grip area is applied over length *k*. The shear load is applied with nodal ties along the tab surface over length *k*. Furthermore, symmetric boundary conditions are used in the X and Y direction layers.

Each ply is modelled with two rows of 3D solid elements. The parametric cases are reported in table 4.1 and the material properties in table 1.1.

To compare the different parametric cases the Tsai-Wu [129] failure index was used and the delamination index (shear stress divided by shear allowable) is evaluated at representative locations as indicator of the geometry performance. The Tsai–Wu failure criterion is a phenomenological material failure theory used for anisotropic composite materials which considers different strengths in tension and compression, as well as shear strengths. The failure index was computed at different locations given in figure 4.3. These locations are:

- The tab interface defined as the segment in figure 4.3 between points 8 to 11.
- The middle interface defined as the segment in figure 4.3 between points 7 to 12.
- The middle section defined as the segment in figure 4.3 between points 14 to 15.
- The start of the gauge section defined as the segment in figure 4.3 between points 10 to 11.

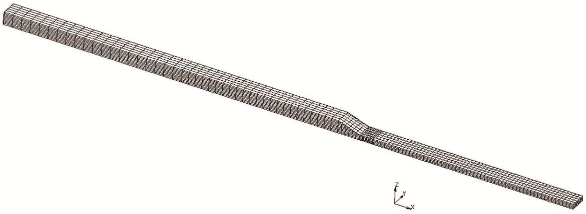

Figure 4.2: Tension coupon mesh model.

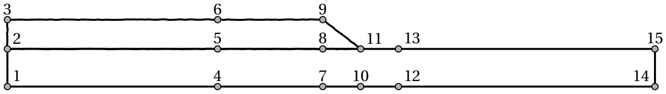

Figure 4.3: Tension coupon parametric geometry analysis points.

PARAMETRIC FE DESIGN ANALYSIS. STRAIGHT TENSION COUPONS

Contrary to the compression tests, the gauge section length (parameter g) does not play a role in the final failure of the tension coupons. However, a large gauge section allows to achieve uniform stresses at the middle of the gauge section, with minimal or no influence of the stress concentrations that appear close to the clamping and tab areas. This allows to measure the elastic modulus using strain gauges in the middle of the gauge section. For that reason large gauge sections are recommended (parameter g).

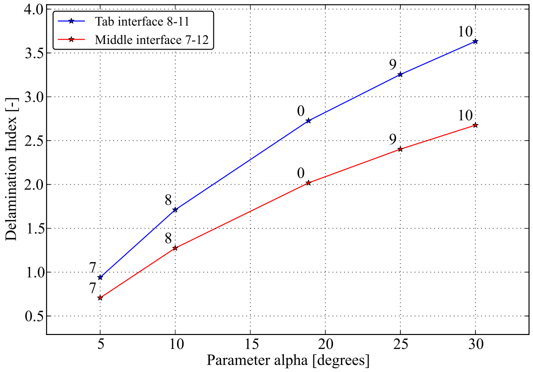

Figure 4.4: Delamination index versus the alpha tab taper angle (UD tabs). Shown for tab interface (between point 8 to 11) and middle interface (between point 7 to 12) according to figure 4.4. Load cases 0,7,8,9 and 10, see Appendix C.

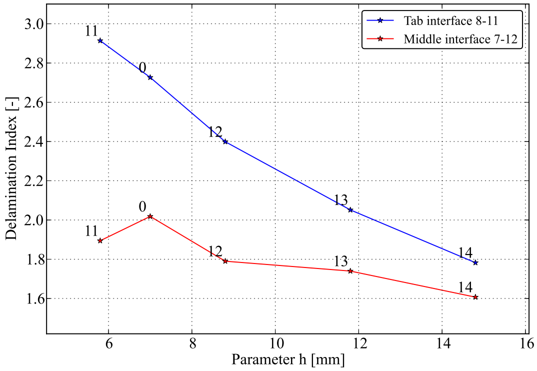

Figure 4.5: Delamination index versus the tab thickness h (UD tabs). Shown for tab interface (between point 8 to 11) and middle interface (between point 7 to 12) according to figure 4.4. Load cases 0,11,12,13 and 14, see Appendix C.

The increase of the tab taper angle α increases the chance of delamination at the tab interface. Figure 4.4 shows how the delamination index increases with tab taper angle. On the other hand, thicker tabs (parameter h) reduce the stress concentrations close to the end of the tab and clamping section and promote a better performance of the coupon. Figure 4.5 shows that thicker tabs reduce the chance of delamination at the tab interface. This trend is also confirmed by figure 4.6 where the Tsai-Wu failure index decreases with the tab thickness, due to the reduction of the concentration of stresses that thicker tabs promote close to the end of the tab and clamping area.

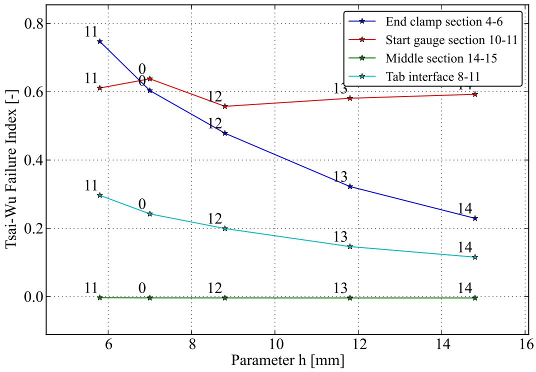

Figure 4.6: Tsai-Wu failure index versus the tab thickness h (UD tabs). Shown for tab interface (between point 8 to 11), middle section (between point 14 to 15), start gauge section (between point 10 to 11) and end clamp section (between point 4 to 6) according to figure 4.4. Load cases 0,11,12,13 and 14, see Appendix C.

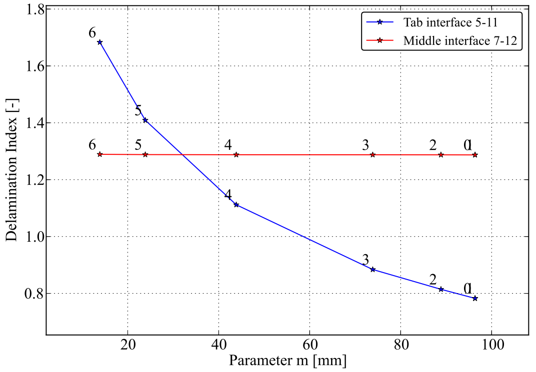

Figure 4.7: Delamination index versus tab length m (biax tabs). Shown for tab interface (between point 5 to 11) and middle interface (between point 7 to 12) according to figure 4.4. Load cases 6,5,4,3,2 and 0, see Appendix C.

The tab length (parameter m or $k+m$) plays a significant role in the delamination of the tab; longer tabs reduce the average shear stress at the tab interface and the chance of delamination. Figure 4.7 shows the evolution of the delamination index with the increase of the tab length *m*; the figure shows that when the tab length *m* increases the delamination index decreases. However, the increase in tab length also causes the assumption of constant shear stress at the tab interface less likely.

TENSION TESTS

Static and fatigue tension tests were carried out for different geometries with a nominal gauge section thickness of 4 mm. Static tests were carried out at 2 mm/min in 100 kN tests frames.

Seven different geometries were considered as shown in table 4.2. Figure 4.10 shows the WC geometry characterized by a waisted width dog bone shape. The WM geometry shown in figure 4.8 is defined by the ISO 527 standard and is characterized by straight shape and bonded tabs. Sub-laminate 5 from plate C from chapter 5 was used as WM dataset. Figures 4.12 and figure 4.9 show WD4 and WD geometries, both are straight shaped and have been manufactured by milling the gauge section. The difference between both is that the WD4 geometry has a width of 8 mm and the WD geometry of 15 mm. WK, WL and WS are the thickness scaled geometries from 4 to 20 mm (see Figure 4.14 to figure 4.16 respectively), they are manufactured as single plates where the tabs have been bonded. In the case of WK and WL geometries, the tab material is aluminium, while for WS geometries the tab material is biaxial laminate due to manufacturing limitations.

ID	**Shape**	**Tabbing**	**Thickness**	**Width**	**Study parameter**	**Test type**	**Geometry**	**Tab**
[-]	[-]	[-]	[mm]	[mm]	[-]	[-]	[-]	[-]
WM	straight	tabbed	3.5	15	control	Static / fatigue	Fig. 4.8	Biax
WC	dog-bone	milled	3.5	10	shape	Static / fatigue	Fig. 4.10	Biax
WD	straight	milled	4	15	width	Static / fatigue	Fig. 4.9	Biax
WD4	straight	milled	4	8	width	Fatigue	Fig. 4.12	Biax
WK	straight	tabbed	3	10	thickness	Static / fatigue	Fig. 4.14	Al
WL	straight	tabbed	7	15	thickness	Static / fatigue	Fig. 4.15	Al
WS	straight	tabbed	20	20	thickness	Static	Fig. 4.16	Biax

Table 4.2: Tension coupons geometries test program overview.

The coupons were manufactured with the resin and fibers used for all experiments and models described in this thesis (see table 1.1) aiming at a nominal thickness of 4 mm, except from the case of the WL and WS geometries. All 4 mm thickness geometries were tested in static and fatigue 100 kN test frames, while the WL and WS geometries were tested in a 400 kN and 1000 kN test frame, respectively. Static test specimens were equipped with strain gauges to measure the elastic modulus and Poisson ratios. Figure

4.11 shows the tests setups for the WC, WD and WK geometries. In the case of WK geometries, a fixture at the end of the tabs was added to avoid the peeling since the grip length was smaller than the tab length. Test setups of the thicker WL and WS geometries are shown in figure 4.13.

For each static test, 8 coupons were tested, and data was analysed according to ISO 527 and ASTM D3039 procedures. The elastic modulus and Poisson ratio were computed between 1000 and 3000 microstrains according to the modulus chord method. Moreover, ultimate strengths were calculated based on the maximum force recorded during the static tests divided by the cross-sectional area.

Fatigue tests were carried out for each one of the previously mentioned geometries, except geometry WS due to machine restrictions. Tests were conducted at a constant force, and a frequency of 2 Hz and a R=0.1 stress ratio. The temperature was measured with thermocouples to monitor self-heating. A limited number of force and displacement signals were recorded as data files at different lifetimes. Grip pressures were chosen as 8 MPa for the 4 mm nominal thickness coupons and increased up to 10 MPa to overcome undesirable slippage at the grips. The same procedure was followed for the WL geometry where the grip area was scaled to achieve higher loads with similar grip pressures. However, in the case of the WS geometry it was not possible to scale the tab length as necessary due to machine limitations, and a pressure close to 12 MPa was necessary to avoid slippage.

Fatigue coupons were tested up to ultimate failure, which was characterised by a total coupon separation into different parts. The achieved number of cycles was recorded and plotted versus the maximum stresses to obtain the S-N curves. A linear regression analysis was used to find the logarithmic model that describes the fatigue life of each geometry.

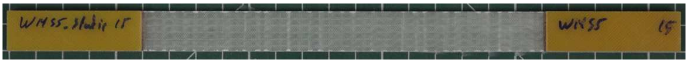

Figure 4.8: WM S5 coupon geometry with straight gauge section. Standard ISO 527 geometry.

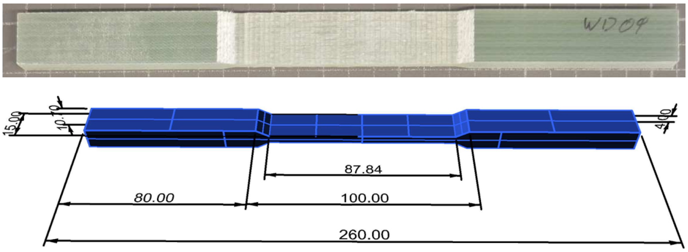

Figure 4.9: WD coupon geometry with straight gauge section. Width 15 mm.

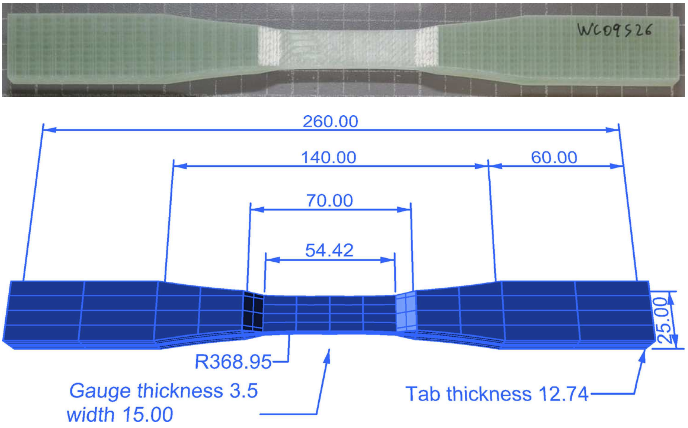

Figure 4.10: WC coupon geometry with waisted gauge section.

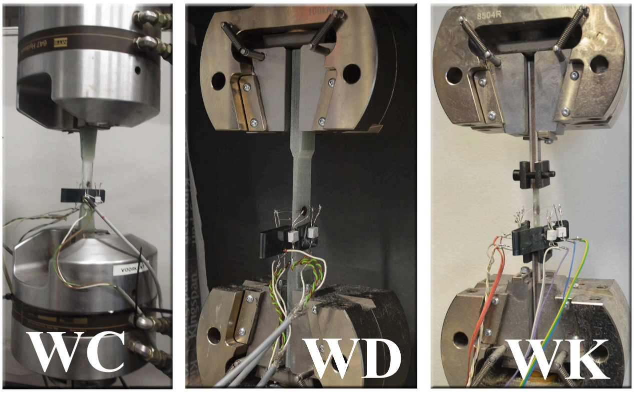

Figure 4.11: WC, WD and WK coupon geometry test setup in a 100 kN test frame.

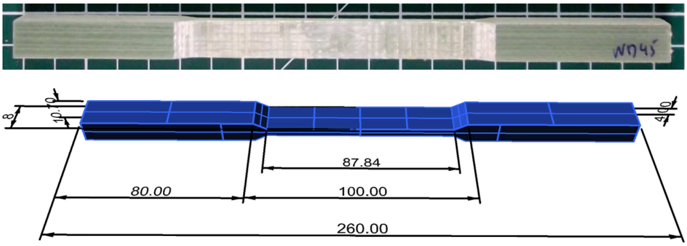

Figure 4.12: WD4 coupon geometry with straight gauge section. Width 8 mm.

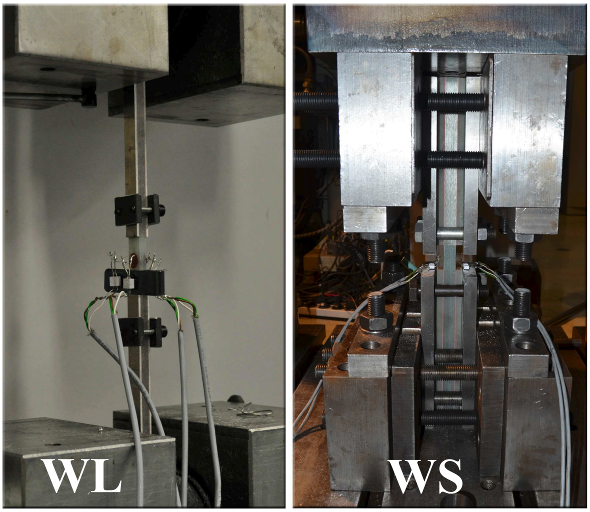

Figure 4.13: WL, WS coupon geometry test setup in a 400 kN test frame.

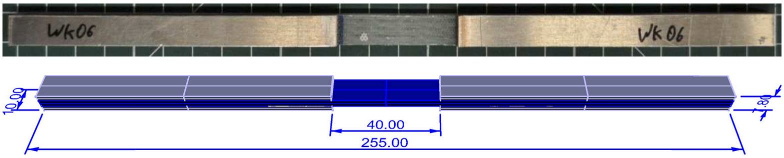

Figure 4.14: WK coupon geometry with straight gauge section and bonded aluminium tabs. 3 mm thick.

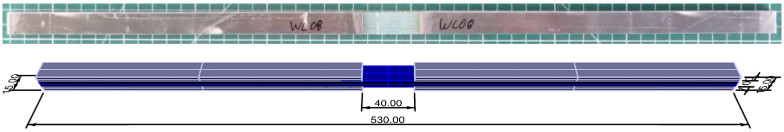

Figure 4.15: WL coupon geometry with straight gauge section and bonded aluminium tabs. 7 mm thick.

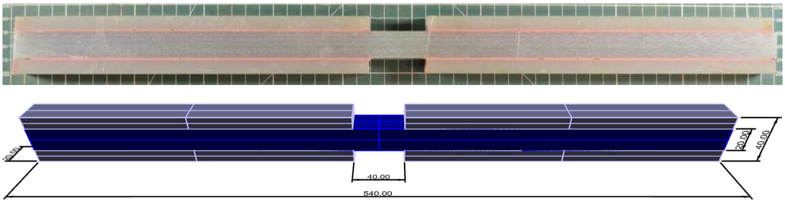

Figure 4.16: WS coupon geometry with straight gauge section and bonded biaxial tabs. 20 mm thick.

TENSION TESTS RESULTS AND DISCUSSION

Table 4.3 and figure 4.18 show a comparison of the ultimate stresses in tension for each of the tested geometries. All 4 mm thick coupons geometries showed similar ultimate stresses. The waisted width geometries show a slight increase of the ultimate stress, but when the intervals of confidence (at 75 % of confidence) are compared with the other geometries, there is overlap, which means that the difference is not statistically representative.

In the case of 4 mm straight gauge sections, a variation in the width (WD, WD4) or the gauge section length (WM, WD, WL) did not show significant influence on the ultimate strengths. Furthermore, if milled tab geometries (WC, WD) are compared with the standard geometry WM ultimate stresses do not show large discrepancies.

The WK geometry with aluminium extended tabs showed the lowest ultimate stress in comparison with the other 4 mm geometries. However, when this design was scaled to WL coupons with 7 mm thickness and larger widths, the ultimate stress revealed to be statistically comparable to the others geometries.

Ultimate strengths between different geometries were comparable. Due to test effects 4 mm thick WK coupons did not show a similar strength as the other 4 mm thick geometries (WC, WD or WM). The WK scaled geometry to WL (7 mm thick) shows a similar ultimate strengths as the 4 mm thick geometries (WC WD or WM), indicating no statistical representative scaling effect between both thicknesses (see figure 4.18). WS 20 mm thick coupons shows a reduction in the ultimate strength in comparison with 4 and 7 mm thick coupons. However, it is believed that this reduction is related to a test effect since it was not possible to test such coupons with similar hydraulic clamping systems and test conditions equal to the others. In particular, WS coupons showed different failure modes, with a preference for the tab failure. To improve the behaviour of thick laminate test tension coupons, it is needed to increase the length of the tabs. However, extended tabs are technically challenging because they require custom grip fixtures of the same length. Further scaling of the geometry to a thickness higher than 20 mm was not done for this thesis because of practical limitations in scaling the clamping system (amount of steelwork).

Table 4.4 and figure 4.19 show the elastic modulus and Poisson ratio for each of the tested geometries. Elastic modulus measurements show similar values for all the coupon geometries. In a similar way, the coefficients of variance is not affected by the change of the geometry or thickness. Similary Poisson coefficient measurements were not influenced by the coupon geometry showing similar values between the different geometries.

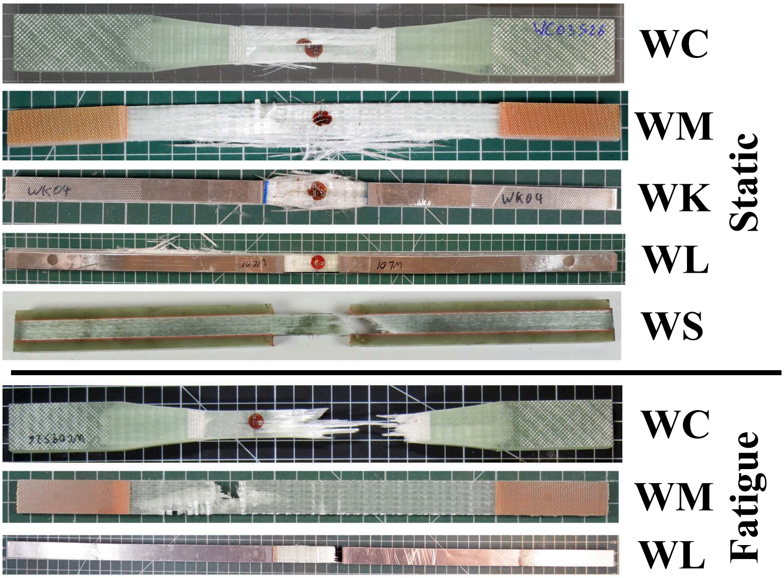

Figure 4.17: Photos of the coupon failure in static and fatigue.

ID	Thickness	Width gauge	N	Strength σ_{max}	
	[mm]	[mm]		[MPa]	COV
WC	3.52	14.43	8	828.4	3.8
WD	4.37	20.79	8	849.4	2.6
WM S5	3.64	14.39	8	850.5	2.4
WK	3.20	9.72	8	724.1	9.6
WL	6.88	14.73	8	815.6	4.6
WS	19.09	19.47	7	717.5	6.2

Table 4.3: Tension coupons geometries static tests (ultimate strength).

Fatigue tests were carried out on specimens with 4 to 7 mm thick tension geometries. Figure 4.20 shows the S-N curves for geometries WC, WD, WD4, WM and WL. A slight enhancement in the fatigue properties can be observed between the standard geometry WM with a slope of 10.3 versus geometry WL with a slope of 6.48. However, all the tested geometries perform at similar levels of stresses and fatigue life, with overlaps between the intervals of confidence of the S-N curves. Self-heating was avoided (see chapter 2) reducing test frequencies from 2 Hz (in the case of 4 mm thick coupons) to 1.5 Hz in the case of WL coupons. The selection of frequencies was based on IR and thermocouples measurements, where temperatures larger than 30°C were avoided. Since stiffness is stable below glass transition temperatures (see figure 2.8), as a criterion temperatures at the middle

ID	Elastic Modulus		Poisson coef.	
	[GPa]	COV	[-]	COV
WC	42.3	3.9	0.382	6.45
WD	39.9	2.4	0.254	10.4
WM S5	39.2	3.9	0.345	4.2
WK	37.9	7.1	0.408	10.7
WL	39.4	3.45	0.345	14.45
WS	40.0	2.22	0.359	11.4

Table 4.4: Tension coupons geometries static tests (modulus and Poisson coef.).

ID	Static tests			Fatigue tests		
Type	Tab debonding	In the tab	Splitting	In the tab	At the tab	At the gauge
WC			8	4	11	
WD			8	13		
WD4					8	
WM S5			8		10	2
WK			8			
WL			8	8	2	
WS	5	2				

Table 4.5: Tension coupons geometries failure modes and locations (ASTM D3039). Numbers of coupons.

thickness below 30°C were considered safe.

The scatter of the S-N curves is of the same order as observed in the Optimat database [14]. Because the scatter of the tests is larger than the differences between the geometries, the observed trends for each geometry cannot be considered as an indication of a size effect, but as statistical disagreement caused by the inherent scatter that composite fatigue tests show.

Failure modes between static tests and fatigue tests showed differences. In the static tests, irrespective of the geometry, the failure type was longitudinal splitting of the gauge section. In the fatigue tests failure occurred as lateral failure across the width at three possible locations: inside the tab, at the tab or at the gauge section. Figure 4.17 shows detailed photos for different types of geometries, with the different failure cases in static and fatigue loading. Table 4.5 describes the number of coupons for each geometry and failure location. Independent of the geometry, the most likely failure location is inside the grip or close to the grip.

The most plausible explanation for the high rate of failures close to the grip or inside the grip is the grip effect. Due to the grip pressure, the highest stresses (τ_{xy} and σ_{yy}) are located at the end of the grip. This is related to the transition between the grip pressure and the gauge area (at net tension) that is located at the end of the grip and gauge section start. At that point the highest stresses can be recorded and therefore this is the most likely location of failure during fatigue.

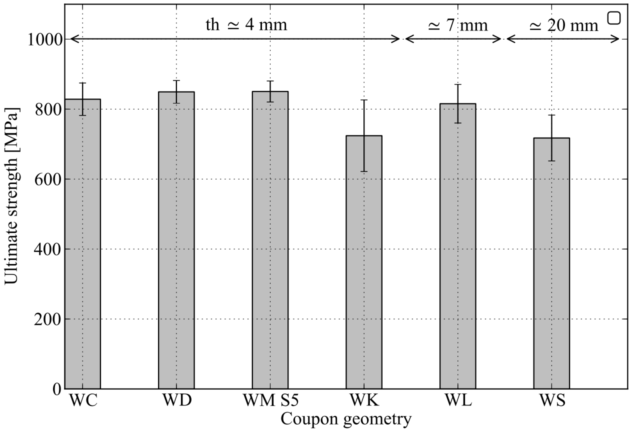

Figure 4.18: Ultimate strengths for each tension coupon geometry.

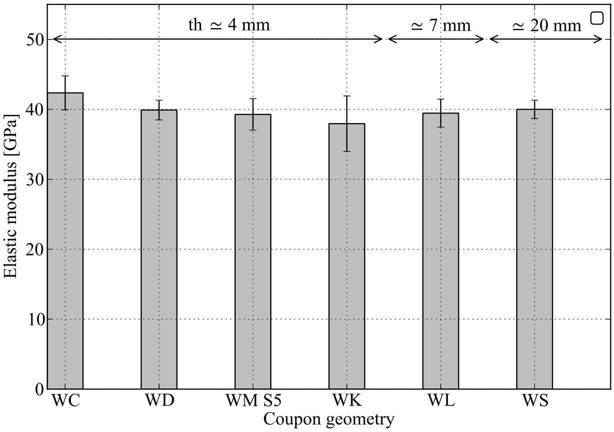

Figure 4.19: Elastic modulus for each tension coupon geometry.

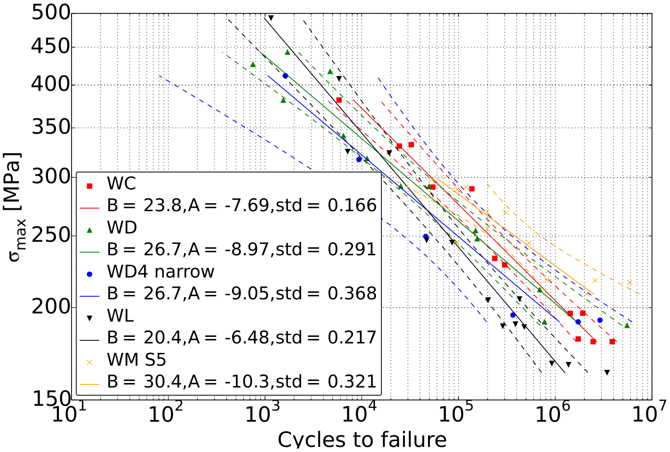

Figure 4.20: S-N fatigue tension curves for WC, WD, WD4, WL and WM. Dotted lines describe 95% intervals of confidence according ASTM 0739-10

CONCLUSIONS

This chapter studies the influence of the coupon geometry and thickness effect in the material tension properties. Different tension geometries and coupon configurations were evaluated based on FE models and experimental tests.

The FE parametric model analysis investigated the role of the different geometrical parameters of a tension coupon during a static test. This can be summarized as follows:

- The gauge section length (parameter g) plays no role in the determination of the ultimate strength, but it plays a role in the modulus measurement.
- Big tab taper angles α increase the chance of delamination in the tab.
- Thicker tabs (parameter h) reduce the stress concentration at the end of the tab.
- Larger tab lengths (parameter m or $k+m$) reduce the average shear stress and the chance of tab delamination.

Six different tension coupon geometries were compared in static tension tests. Waisted width geometries (WC) and milled gauge section coupons (WD) showed a statistically similar performance as standard coupons (WM). Furthermore, the elastic modulus and Poisson ratios were compared statistically. Static tests from thickness scaled coupons (WK, WL & WS) showed non-uniform results. No strength reduction was found when going from 4 to 7 mm thickness. For 20 mm thick coupons a strength reduction was found.

However, for practical reasons the coupon design was different for this thickness, which may have given rise to a test effect in the measurements.

Fatigue tests were performed for five different geometries up to a 7 mm thickness. S-N curves show that slopes vary between 7 to 10. However, the differences between geometries and thicknesses were not found statistically relevant when the interval of confidence regions are compared.

When tests effects as the grip effect are disregarded, no statistically representative thickness or scaling effects were observed for the UD tension tests. The absence of a thickness effect in UD tension tests can be related to the failure modes in which the geometry or the matrix does not play a strong role, and are mainly dominated by net fibre failure.

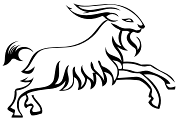

5

THE MANUFACTURING PROCESS INFLUENCE ON THICK LAMINATES MECHANICAL PROPERTIES

This chapter studies the influence of the manufacturing on the through thickness distribution of mechanical properties in thick laminates. For that purpose, a method was developed which allows to extract plates at different thicknesses positions that can be tested as standard coupons. A relation between the mechanical properties and the manufacturing conditions is proposed. This relation was evaluated based on the thickness scaled tests experimental data.

INTRODUCTION

Thick laminates are widely used in wind turbine blades. Specifically cap and root subcomponents can have thicknesses between 40-60 mm in a 40 meter long blade and up to 100-150 mm for a 100 meter blade. A decrease in thick laminates mechanical properties has been reported for carbon fibre pre-pregs [127] as well as for glass fibre infused composites [128]. In addition to scaling effects [32] and self-heating [110] during fatigue, it is suspected that the manufacturing process influences the mechanical properties of thick laminates.

In order to evaluate laminate performance, a laminate has to be manufactured first. Different parameters in the manufacturing process influence the properties such as the curing cycle and the infusion process.

White [98] reported that the curing temperature determines the degree of curing and the ultimate strengths of the resin system. Huang [99] described different interfacial failure properties for two different curing cycles with differences of 20 %. In addition, Ziaee

---

This chapter was integrally extracted from [130] and section 5.4 was extracted from [123].

[100] reported a strong variation of the strength and a decrease of 70 % in the fracture toughness with decreasing cure temperatures for vinyl-ester resins. Moreover, Lee [95] elaborated a series of expressions that can be used in conjunction with cure models in order to evaluate the effects of the curing cycle on strength and stiffness of the composite after manufacturing. Following an experimental approach, a relation between the heat transfer rate and the interlaminar shear strength (ILSS) was observed by Davies [96] and also by Liu [97] for epoxy resin in carbon reinforced composites. In addition, for a vinyl-ester resin Ziaee [100] reported strong differences in the ultimate strength and strain at failure for different curing cycles. Zhang [101] reported a strong influence of the temperature cure cycle ramps on the hardness of an epoxy resin. Lately Boey [105] reported a dependence of the flexural properties on the curing cycle and Shin [106] the process sensitivity of the compression strength. These works report bibliographical evidences on the influence of the thermal history on the final mechanical properties. In addition, the curing rate and temperature profiles are parameters that characterize the thermoset resins cure kinetics and thermal history. The relevance of the curing rate in the resin cure-kinetics has been discussed by several authors [131–133]. Furthermore, Kubota [134] discussed on the relation between curing rates and mechanical properties. However, it was not possible to find a direct bibliographical correlation between the mechanical properties and the cure kinetics parameters.

White and Kim [102] developed and studied the technique of staged curing, in which two or more thin (<6 mm thick) pre-preg laminates are manufactured at once with a similar curing cycle per staged laminate. Later, Ciriscioli [103] reported a technique to determine mechanical properties of thick pre-pregs using a porous film in between. This technique was applied in order to compare the properties of laminates of different thicknesses at the middle thickness position.

While for thin laminates curing temperatures do not show large gradients through the thickness, in thick laminates large gradients are observed [107]. Effectively, this is related to a curing cycle variation through the thickness. This variation can be expected to become more pronounced in thicker laminates, due to the exothermic nature of most curing cycles and the low thermal conductivity of the (uncured) resins and fibers.

Thus, it is postulated that as a result of differences in the local curing cycles at different thickness positions, local mechanical properties in thick laminates vary significantly through the thickness. In this paper, these effects on mechanical properties at different thickness positions (i.e. different curing cycles) in a thick laminate are quantified.

To this end, 60-70 mm thick unidirectional GFRP/epoxy infused panels were monitored during the manufacturing. The thick laminates were divided into sub-laminates with the help of peel-ply layers at different thickness positions. From each sub-laminate, specimens were milled and mechanical static and fatigue tests were performed. The re-

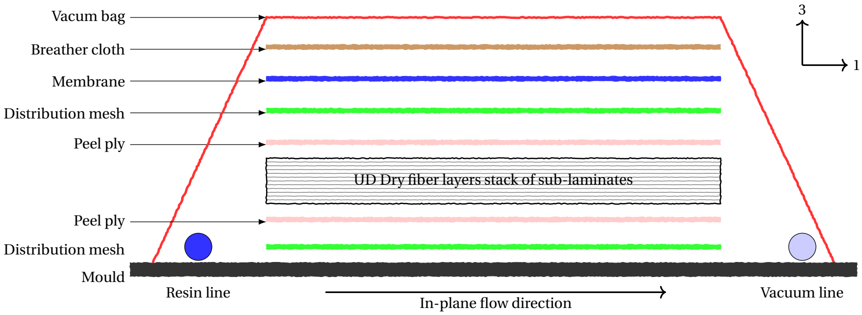

Figure 5.1: Vacuum bagging configuration.

sulting strength and fatigue data were correlated with the local curing cycles.

MATERIALS AND METHODS

The material used for the experimental work was a commonly used wind energy epoxy resin (Hexion RIM 135) and a UD glass fibre type E 600 g/m^2 non-crimp fabric. The experimental work was divided in two main phases: manufacturing of the thick laminates including the sub-laminate extraction and the sub-laminate mechanical tests.

MANUFACTURING PROCESS AND SUB-LAMINATE EXTRACTION

Three panels of 600x600 mm and 65 mm thick were vacuum infused on an aluminium mould [104]. A conventional vacuum infusion process configuration with in-plane flow was used (see figure 5.1), and constant vacuum was applied during the curing cycle. The resin was tempered at 25 $^\circ C$ before the infusion and degassed while infused. The same manufacturing process conditions were arranged for the three plates, apart from the curing cycles. Figure 5.2 shows a scheme of the curing cycle applied to the three panels (see table 5.1). The curing cycle was composed of two temperature stages. The first stage of the curing cycle corresponds to the hardening of the resin and the second stage corresponds to post-curing of the resin at 80 $^\circ C$ (see figure 5.2). While panel A and B were cured with the same curing cycle with a first stage temperature of 35 $^\circ C$, panel C was cured with a first stage setup temperature of 60 $^\circ C$ (see table 5.1).

In order to allow the extraction of the sub-laminate panels, alternate peel ply layers with layers of reinforcement fabrics were stacked up (see figure 5.4 and figure 5.5). For panel A a non-coated standard Nylon peel ply (AirTech© Release Ply A) was used, and for panel B and C a peel ply with hard PTFE coating (AirTech© Release Ease© 234 TFP) was used. The sub-laminates were either 4 layers or 10 layers thick. The 4 layer thick sub-laminates were used to manufacture tensile specimens, the 10 layer thick sub-laminates

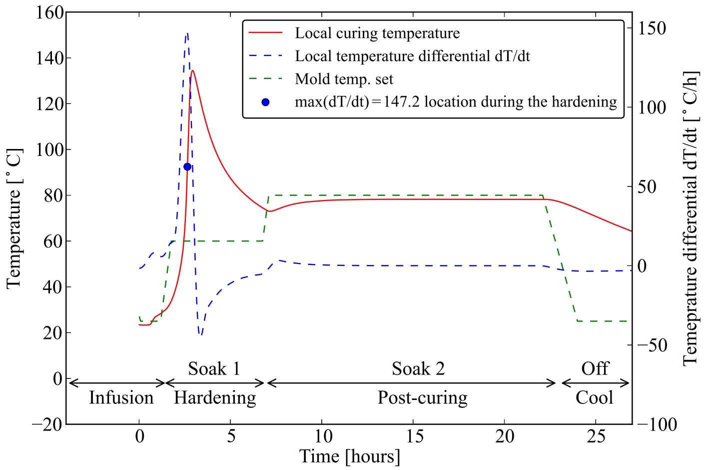

Figure 5.2: Scheme of mould temperature, local curing cycle temperature at a random thickness location and temperature differential dT/dt.

were milled into compression specimens with a reduced gauge section thickness of 4 mm. Interlaminar shear strengths (ILSS) test specimens were cut from the spare and non-tested compression coupons.

Six type K thermocouples were embedded at different thicknesses positions in the laminate in order to monitor the local curing temperatures. In addition, four strain gauges were embedded in panel A, in order to monitor the residual strains during curing (see table 5.1).

Thermocouples and strain gauges were embedded at $x = 200$ mm from one of the side and at $y = 300$ mm from the lateral side as figure 5.3 shows. Both were placed between the fabrics according to table 5.1 and oriented with the unidirectional fiber direction (1).

From the local temperature signals at different thickness positions the maximum temperature rates during the hardening phase $max(dT/dt)$ were obtained (see figure 5.2). Curing temperature rates (dT/dt) were computed using the Savitzky-Golay method [135]. Temperatures and strains signals were recorded every 10 sec.

The resin infusions were carried out at 0.9 bar pressure differential between vacuum port and resin supply line. The infusion times were 25-30 minutes long. The mass mixing ratio of the resin (Hexion RIM 135) and hardener (Hexion RIM 137) was as prescribed by the manufacturer, i.e. 100:30. The curing cycles were applied according to table 5.1. Finally, the panels were released from the mould and divided into sub-laminates.

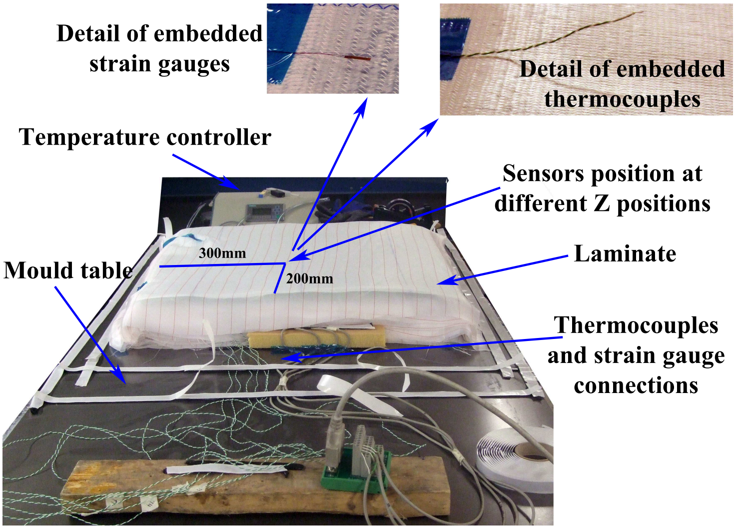

Figure 5.3: Panel A mould and laminate image before closing the vacuum bag. Detail of the embedded thermocouples and strain gauges.

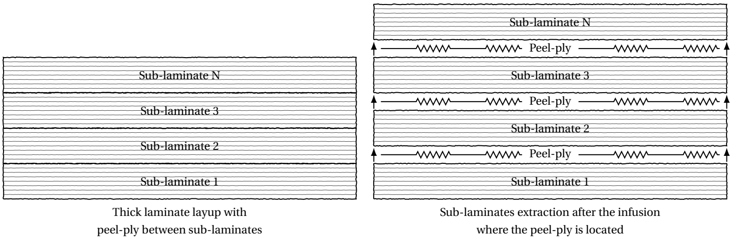

Figure 5.4: Sub-laminates manufacturing and extraction method. The laminate is cured with peel-ply layers in between fabric layers (left). The cured laminate is divided into sub-laminates at peel ply layer locations (right).

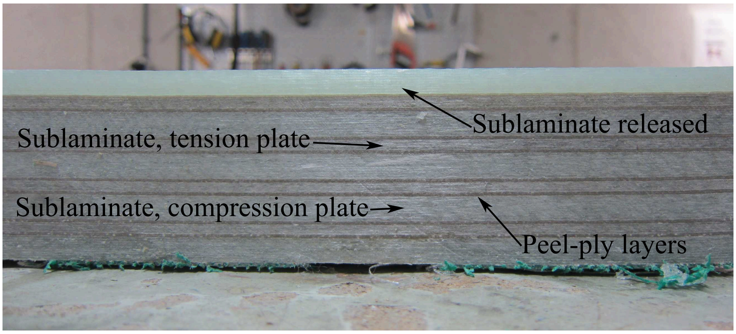

Figure 5.5: Panel B section view, sub-laminates detail.

	Panel A	**Panel B**	**Panel C**
Thickness $[mm]$	55.65 mm (80 layers)	64 mm (80 layers)	64 mm (80 layers)
Layup	5 x (10UD | PP | 4UD | PP) | 10UD		
Peel ply type (PP)	Nylon	PTFE	PTFE
Temperature sensors (T) and strain gauges (S)	T1: layer 1-2 S1, T2: layer 15-16 S2, T3: layer 29-30 S3, T4: layer 45-46 S4, T5: layer 59-60 T6: layer 73-74	T1: layer 1-2 T2: layer 15-16 T3: layer 29-30 T4: layer 45-46 T5: layer 59-60 T6: layer 73-74	T1: layer 1-2 T2: layer 15-16 T3: layer 29-30 T4: layer 45-46 T5: layer 59-60 T6: layer 73-74
Sub-laminates identification. Compression panels as C, tension panels as Ten.	C1: layer 1-10 Ten1: layer 11-14 C2: layer 15-24 Ten2: layer 25-28 C3: layer 29-38 Ten3: layer 39-42 C4: layer 43-52 Ten4: layer 53-56 C5: layer 57-66 Ten5: layer 67-70 C6: layer 71-80	C1: layer 1-10 Ten1: layer 11-14 C2: layer 15-24 Ten2: layer 25-28 C3: layer 29-38 Ten3: layer 39-42 C4: layer 43-52 Ten4: layer 53-56 C5: layer 57-66 Ten5: layer 67-70 C6: layer 71-80	C1: layer 1-10 Ten1: layer 11-14 C2: layer 15-24 Ten2: layer 25-28 C3: layer 29-38 Ten3: layer 39-42 C4: layer 43-52 Ten4: layer 53-56 C5: layer 57-66 Ten5: layer 67-70 C6: layer 71-80
Mold curing cycle	Infusion: $25^\circ C$ Soak 1: $35^\circ C$ 380 min Soak 2: $80^\circ C$ 800 min	Infusion: $25^\circ C$ Soak 1: $35^\circ C$ 380 min Soak 2: $80^\circ C$ 800 min	Infusion: $25^\circ C$ Soak 1: $60^\circ C$ 380 min Soak 2: $80^\circ C$ 800 min

Table 5.1: Panels manufacturing parameters and layout.

MECHANICAL TESTS SETUP

From each sub-laminate glass transition temperatures (T_g) were calculated with a Netzsch differential scanning calorimeter DSC according to ISO 11357. The fiber weight ratio (FWR) and void content was calculated by a calcination method according to ISO 1172. Coupons were extracted from the center of the plates, avoiding the extremes, assuming the in-plane temperatures are even in plane 12 and vary significantly in the thickness direction 3. Table 2 shows the static and fatigue test matrix for the sub-laminate tests in tension, compression and inter-laminar shear loading (see figure 5.6).

Compression tests

Compression tests coupons with 4 mm gauge section thickness were used. The compression coupons were tested on an MTS servo hydraulic 100 kN test frame. Static tests were performed with a combined loading compression CLC fixture according to ASTM D6641 and fatigue tests were performed with the standard machine clamping system at an R-ratio of 10. Compression coupons were manufactured from sub-laminates from panel A, B and C according to the test matrix in table 5.2. The compression coupon had a milled gauge section with integrated tabs [123, 128]. Static tests were carried out at a test speed of 1 mm/min and fatigue tests at frequencies of 2 Hz.

Tension tests

Tension coupons according to ISO 527-5/A, 2.5 mm thick and 15 mm wide were manufactured from panel B and C sub-laminates according to the test matrix in table 5.2. Tensile static tests were carried out in a Zwick 100 kN test frame at a test speed of 1 mm/min with coupons equipped with cross strain gauges in order to measure the initial elastic modulus and Poisson ratio. In addition, fatigue tests of tension coupons were carried out at tests frequencies of 2 Hz and tension-tension R-ratios of 0.1.

Inter-laminar shear tests

Inter-laminar shear tests (ILSS) were carried out according to ASTM D2344. Coupons with dimensions 42x14x7 mm from each of the 10 layer sub-laminates were tested in a Zwick 100 kN frame test frame with a 5 kN load cell at 2 mm/min loading speed and a span length of 28 mm.

RESULTS AND DISCUSSION

In the following sections the results from the manufacturing process, static tests, and fatigue tests are discussed in detail. In addition, a manufacturing failure analysis criterion is proposed.

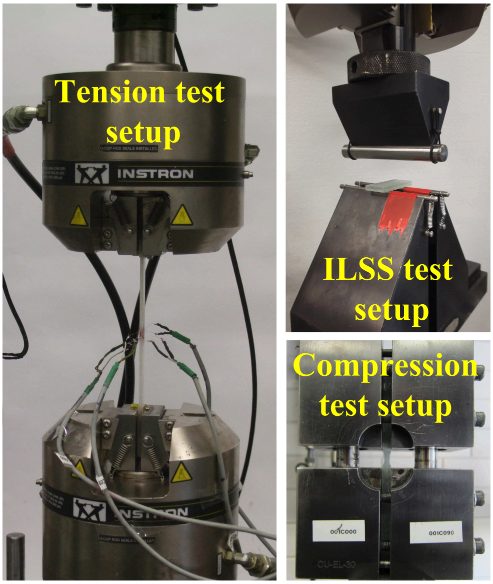

Figure 5.6: Tests setups for compression, tension and ILSS tests.

	Panel A	**Panel B**	**Panel C**
	Sub-laminates		
Static compression test (0°)*	C1 to C5	C1 to C6	C1 to C6
Static tension test (0°)*		Ten1 to Ten5	Ten1 to Ten5
ILSS static test (0°)*		C1 to C6	C1 to C6
Fatigue compression test (0°)**		C1, C3 & C6	
Fatigue tension test (0°)**		Ten1, Ten3 & Ten6	

Table 5.2: Test matrix. * Static tests, 6-8 coupons per sub-laminate. ** Fatigue tests, 10-15 coupons per sub-laminate.

MANUFACTURING PROCESS

Panel A, B and C were cured as a monolithic laminate and subdivided into sub-laminates. For panel A, it was difficult to separate it into sub-laminates due to the use of a standard nylon peel ply. However, the laminate was subdivided into sub-laminates without visible damage. For panel B and C, a PTFE peel ply was used which showed excellent release characteristics, requiring no mechanical effort to sub-divide the thick laminate, this avoiding any possibility of damage while the laminates were subdivided. Panel A was 8 mm thinner than panel B and C due to the difference in thickness of the different peel plies. Because of the low releasing properties of panel A peel ply it was possible only to extract coupons from the five first sub-laminates for the compression coupons. With the PTFE peel-ply for panel B and C all sub-laminates were extracted successfully.

The fibre content and glass transition temperature of the sub-laminates were measured. While panel A showed fibre weight ratios (FWR) of 70%, fibre weight ratios of panel B and C were approximately 5% larger (see figure 5.7) measured at different thickness positions. The void content was below 0.1% for all sub-laminates. Differential scanning calorimeter (DSC) glass transition temperatures (T_g) were around 80-85 °C (see figure 5.8). For the three panels, the fibre weight ratios and void contents did not show a correlation with thickness position. Therefore in the three cases it was considered that the resin was uniformly infused through the thickness during the infusion process. In addition, the glass transition temperatures did not show a strong correlation with the thickness position which indicates uniform levels of curing and similar curing degrees α.

Furthermore, residual strain values varied between 40 to 100 micro strains (0.004 to 0.01% elongations) showing no correlation with the thickness position. Residual strains were very small in comparison with the ultimate strains of more than 2%.

In general, strong temperature gradients through the thickness were observed during the resin hardening stage which means different local curing cycles per thickness position and sub-laminate. Since panel A and B were cured with the same mould curing cycle, the recorded local curing cycles from both were very close, with differences lower than ten degrees celcius. On the other hand, panel C showed maximum temperatures 40 °C larger than panel B or A, which are caused by the increase of 25 °C in the soak 1 mould curing cycle for panel C. Figure 5.9 shows the temperature profiles through the thickness for the three panels, the thickness position Z (Z=0 is the mold side) is plotted versus the temperatures of the embedded thermocouples. While for panels A and B the maximum temperatures occurred at the mid-thickness of the laminates, in case of panel C the maximum temperature was shifted to the outer side. These profiles also depend on the mould system and mould material. The mould used here was made of aluminium. Due to the exothermic curing reaction, the temperature in the laminate exceeds the mould temperature during soak 1. In this stage, the mould acts as a cooling system rather than a heating

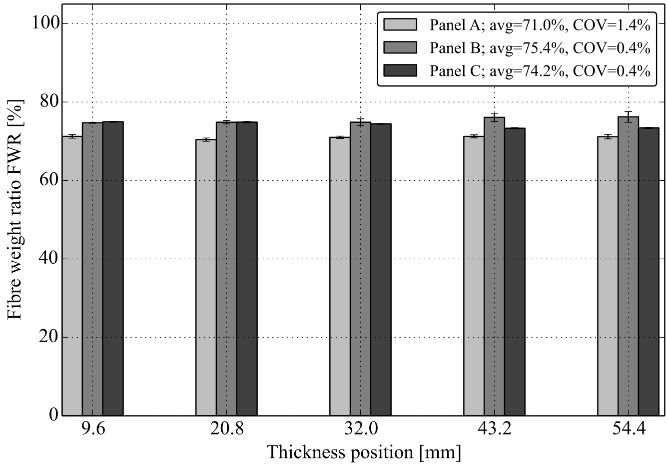

Figure 5.7: Fibre weight ratio at different thicknesses positions for panel A, B and C.

system.

Figure 5.10 and figure 5.11 show the temperature evolution of the embedded thermocouples for panel B and C. Maximum local heating rates during the hardening of the resin were larger for panel C than for panels A and B at all thickness positions. While the maximum heating rates during the hardening for panel A and B were in the range between 0 to 60 °C/h, in the case of panel C they ranged from 60 to 160 °C/h.

MECHANICAL STATIC TESTS

Tension, compression and ILSS static tests on specimens from panels A, B, C were carried out to study the laminate properties through the thickness. Figure 5.12 shows the ultimate tensile strengths and elastic moduli of panel B and C of each sub-laminate through the thickness. Figure 5.12 does not show statistically significant ultimate strength or elastic modulus variations with thickness position. This can be explained by the fact that strength and stiffness in fiber direction are dominated by the fibre properties and fibre volume fraction, which are independent of the curing cycle.

On the contrary, in the case of ILSS tests on specimens from sub-laminates of panel B and C, a correlation between the ILSS property and the thickness position (see figure 5.13) can be observed for panel B and no variation in the case of panel C. This may be explained by the matrix or matrix-fibre interface being influenced by the different local temperature history. Panel B showed lower ILSS values at the outer thickness positions. Panel C ILSS values showed a weaker correlation with the thickness position than panel

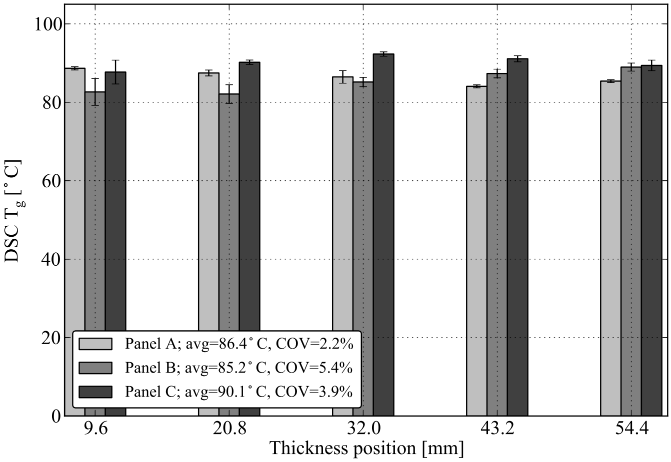

Figure 5.8: DSC glass transitions temperatures through the thickness for panel A and B.

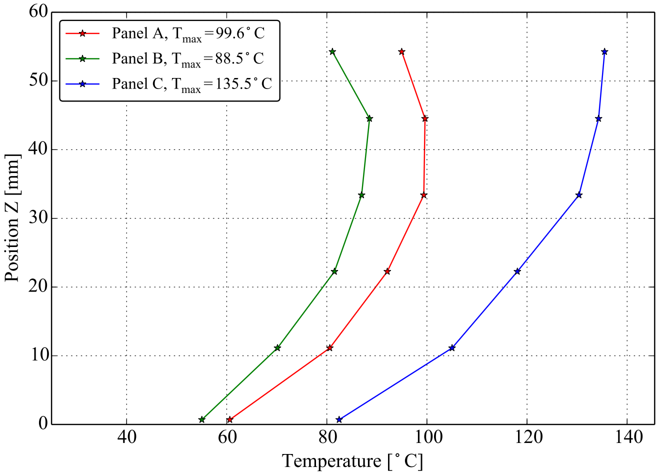

Figure 5.9: Temperature profile of panel A, B and C during curing at the maximum temperature instant.

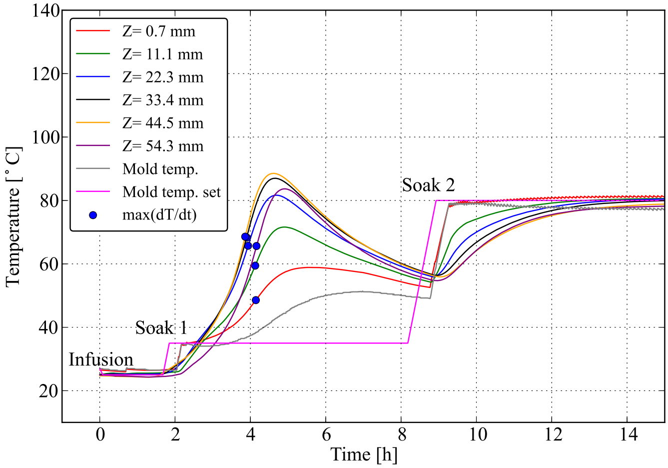

Figure 5.10: Temperature measurements during the manufacturing of panel B. Maximum heating rates locations during hardening are indicated with a blue dot $max(dT/dt)$.

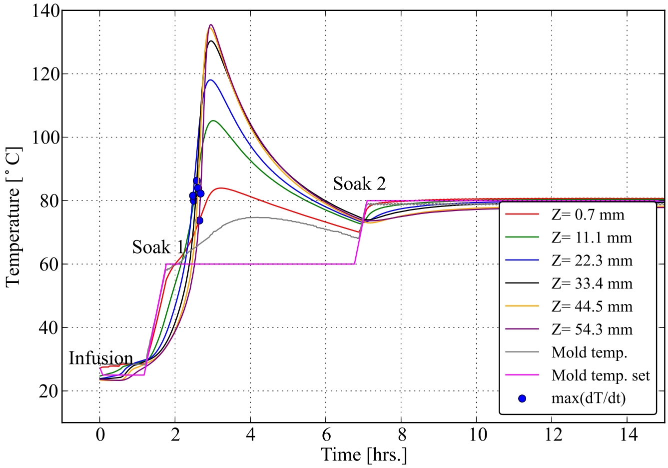

Figure 5.11: Temperature measurements during the manufacturing of panel C. Maximum heating rates locations during hardening are indicated with a blue dot $max(dT/dt)$.

B.

Compression tests for panel A, B and C sub-laminates showed behaviour similar to ILSS results. While panel A and B showed lower ultimate strengths for the outer layers than the inner layers, panel C showed a smaller dependence on the thickness (see figure 5.14). The offset in ultimate strengths between panel A and B was related to the 5% fibre weight ratio variation between panel A and B since both were manufactured with the same curing cycle. Here, the lower fiber content (panel A) results in higher strengths. This is perhaps counter intuitive but previously reported. The decreasing performance for increasing fiber content can be related to the fact that for very high fiber content the bonding between neighboring fibers is not always ensured [136, 137]. The measured strength values are in agreement with previous [123, 128] compression thickness scaled tests carried out for the same material and conditions, with ultimate strengths around 650 MPa for coupons thicknesses between 4 to 20 mm. This value from full laminate tests is closer to the minimum sub-laminates values than to the highest values, which is in line with the theory of the weakest link theory, which states that the lowest local ultimate strength will drive final failure of a section.

Since the local curing temperatures were recorded with embedded thermocouples, it was possible to compute the maximum heating rates ($max(dT/dt)$) during hardening as an indicator of the local curing cycles experienced by each sub-laminate. These heating rates are related to the local mechanical properties. Figure 5.15 and figure 5.16 show the evolution of the ILSS values and the ultimate compression strengths plotted versus the maximum heating rates during hardening. In both cases, the curves show an initial linear increase for the smaller heating rates until a maximum plateau is achieved at a specific heating rate.

Therefore, since the fibre-resin systems tested showed a correlation between the curing cycles and the mechanical properties (see figure 5.15 and figure 5.16), larger thicknesses (for the same resin system/identical cure kinetics) might show wider mechanical property distributions through the thickness due to the wider distribution of local temperature cycles.

HEATING RATE VERSUS CURING RATE

The thermoset matrix properties depend on the degree of cure α and the structure formed during the curing reaction. Since the degree of cure does not change through the thickness, which is indicated by the absence of significant variation of the glass transition temperature through the thickness (see figure 5.8). The influence of the structure is considered as the main reason for the observed variation in strength. The curing rate has been identified with the change in structure, since it influences the gel time and the microgelled region size. Different authors [131–133] have discussed the relevance of the curing

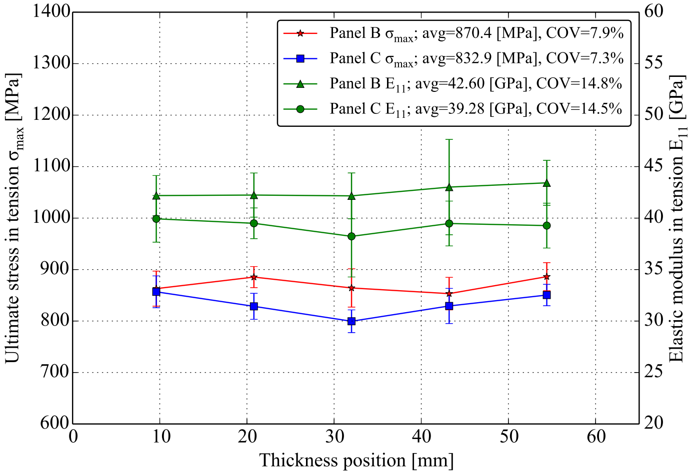

Figure 5.12: Ultimate tension strengths and elastic modulus through the thickness for panel B and C. (Each data point represents N=8 coupons).

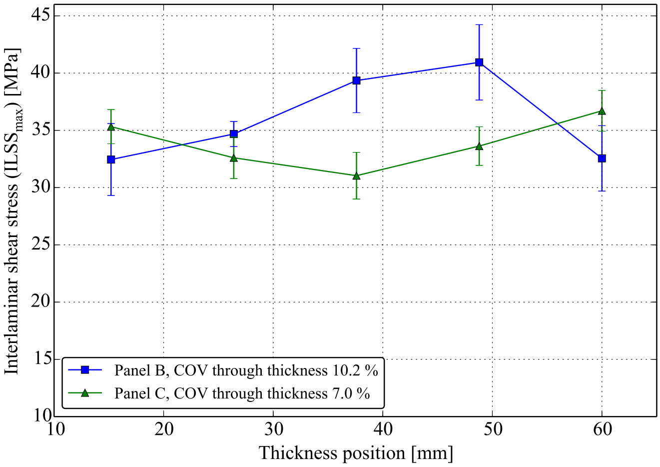

Figure 5.13: Interlaminar shear tests (ILSS) through the thickness for panel B and C. (Each data point represents N=6 coupons).

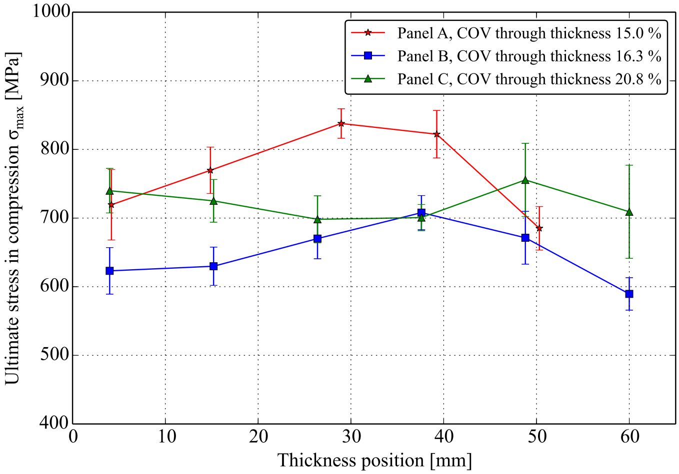

Figure 5.14: Ultimate compression strengths through the thickness for panel A, B and C. (Each data point represents N=8 coupons).

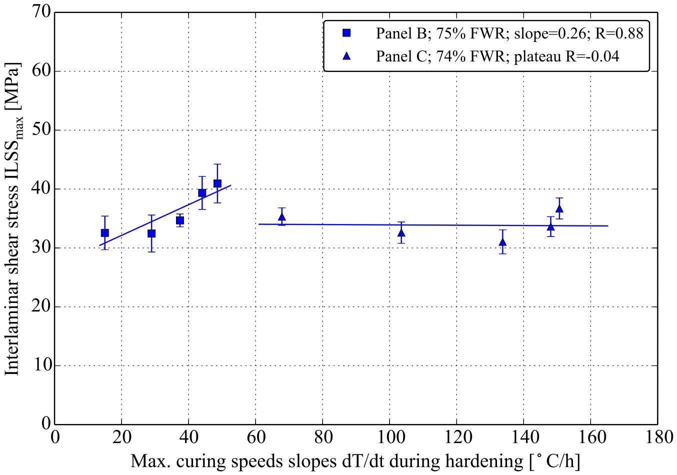

Figure 5.15: Interlaminar shear stresses (ILSS) relation with the maximum curing speeds during the hardening. Panel B and C (FWR: fibre weight ratio, lines performed with a linear regression analysis).

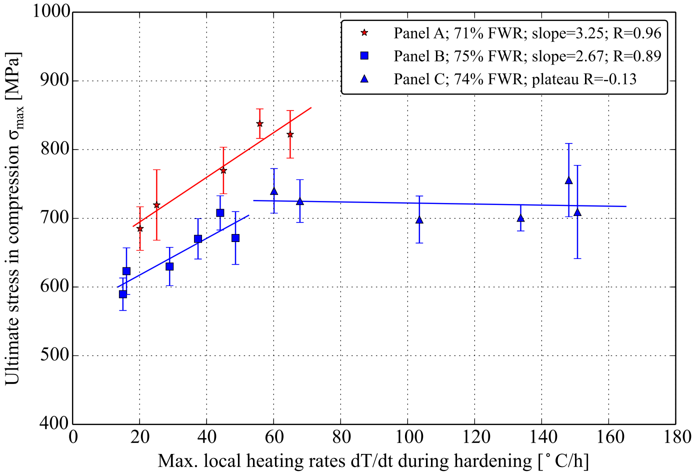

Figure 5.16: Ultimate compression strengths versus maximum heating rates during the hardening. Panel A, B and C (FWR: fibre weight ratio, lines performed with a linear regression analysis).

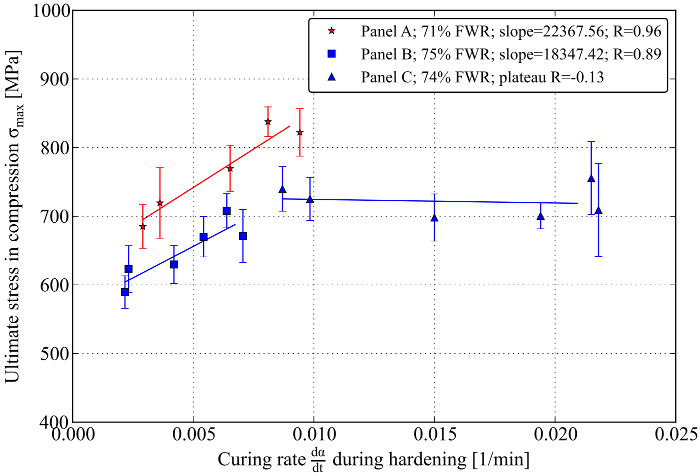

Figure 5.17: Ultimate compression strengths versus curing rates during the hardening. Panel A, B and C (FWR: fibre weight ratio, lines performed with a linear regression analysis).

rate on the structure and the curing. Moreover, Kubota [134] reported superior mechanical properties with higher rates of curing. However, most of the kinetic studies that consider the curing rate are DSC studies on pure resin, without a direct correlation between the mechanical properties of composite material and the curing rates.

In appendix D, the curing rate is shown to be proportional to the heating rate according the following formula,

$$\frac{dT}{dt} \simeq \frac{H_r}{c_P} \cdot \frac{d\alpha}{dt} \tag{5.1}$$

where c_P is the specific heat and H_r is the total heat of the reaction and α is the degree of cure. Since the heating rate and the curing rate are proportional, the correlation between maximum heating rate and mechanical properties found in this study agrees with earlier observations that reveals the influence of the curing rate on the resin properties. The evolution of the matrix related properties with the heating rates from figure 5.15 and 5.16 can also be plotted for the curing rates, when the heating rate is converted into the curing rate with figure D.2 cross-correlation. For example figure 5.17 shows the relation between the curing rates and the compression strengths according figure D.2.

ULTIMATE STRENGTH MODEL BASED ON MAXIMUM HEATING RATE DURING CURING

The relations described in figure 5.15 and figure 5.16 between the ultimate strengths and the maximum heating rates allow to link the spatial temperature field $T(x, y, z, t)$ of the manufacturing curing process to a spatial field of ultimate strengths $S(x, y, z)$ for each one of the different in-plane properties that characterise a laminate. According to the experimental data such relation can be modeled as a linear function with a plateau for the shear and the compression properties (see figure 5.18). With such model it is possible to describe a spatial field of ultimate strengths for a part that has been manufactured with a certain curing cycle. Such a distribution of ultimate strengths can be used in conjunction with a phenomenological failure criterion (i.e max stress, Hill [138], Tsai-Wu [129], Hashin [139], Puck [140], LaRC03 [141]) in order to determine a local failure index field, tuned in agreement with the locally experienced manufacturing curing cycle (see figure 5.19).

According to the theory of the weakest link the failure of a thick laminate section can be expected to be initiated by the ultimate strength which has been cured at the lower heating rates. The maximum and minimum possible ultimate strengths (σ_{max} and σ_{min}) are determined by the local curing cycles. Attending to appendix A, the same reasoning can be given for the curing rates, where the local mechanical properties are defined by the local curing rates experienced by the resin.

Other resin related properties, such as transverse tensile strength, fracture toughness

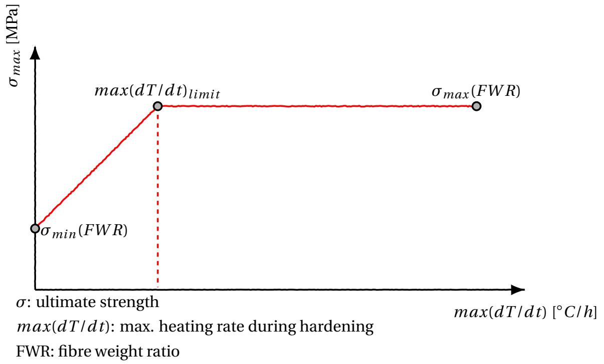

Figure 5.18: Model for ultimate strength as a function of heating rate during curing.

and in plane shear strength, are expected to follow a similar behaviour as the one observed for the compression strength and the ILSS and possibly the same holds for transverse and shear moduli. However, further research on this matter is required in order to confirm this hypothesis.

The proposed model between the heating or curing rates and the resin properties ultimate strengths, was applied successfully to explain scaling effects observed in an experimental campaign of scaled compression tests [123].

MECHANICAL FATIGUE TESTS

The same type of coupons extracted from the sub-laminates and evaluated in the static tests were also tested in tension and compression fatigue tests. Figure 5.20 shows the S-N curves at tension-tension loading for three different sub-laminates of panel B. Similar as in the static tension tests, independent of the thickness position or heating rates during cure, the three S-N curves show similar Pearson correlation coefficients, with values around 0.98 as well as similar fatigue slopes B around 6.7.

To characterize the fatigue properties distribution of the full laminate thickness, the aggregated S-N curve was built for a thick panel considering all coupons from the different sub-laminates together. Such aggregated S-N curves are shown for the tension-tension fatigue tests in figure 5.20, showing similar Pearson correlation coefficients and fatigue slopes B to the S-N curves of each of the sub-laminates due to the minor correlation that exists between the UD tension properties and the thickness position or curing heating rates.

Contrarily, S-N curves carried out at compression-compression loading for three different sub-laminates from panel B taken at three different positions did show a relation with the thickness position or the heating curing rates. Figure 5.21 shows that the three

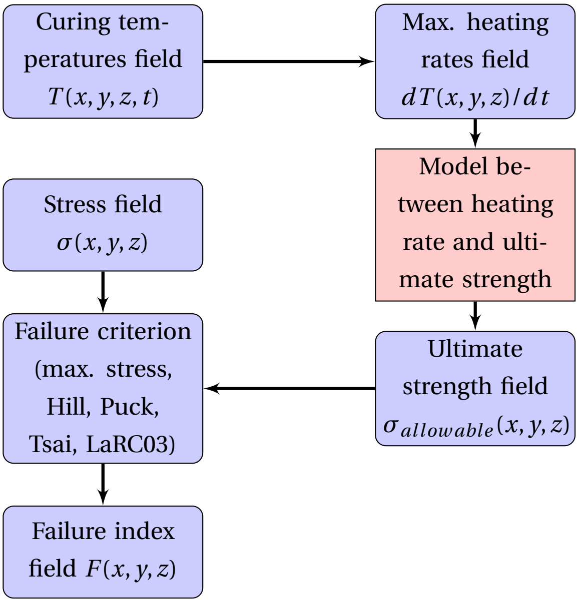

Figure 5.19: Determination of local failure index tuned according the manufacturing curing cycle using the model between heating rate during curing and ultimate strengths.

panel B sub-laminates exhibit a different behaviour with different fatigue slopes for the outer sub-laminates than for the inner sub-laminates and a larger scatter as quantified by the correlation coefficient R. Such behaviour can also be observed in the aggregated S-N curve, which shows significantly lower R correlation coefficients than the individual sub-laminates. This agrees with the large distribution of compression mechanical properties through the thickness showed by the static mechanical tests.

According to this fatigue data observations, it is concluded that there exists a dependence of the S-N curves on the resin structure, which is in turn influenced by the heating or curing rates. Therefore, S-N curves of standard coupons manufactured from thin plates, might not precisely represent fatigue behaviour of thick laminates for resin dominated mechanical properties, because the associated curing rates of thin and thick laminates will be different. Therefore, further research on the influence of the curing rates on fatigue properties is required to be able to optimize the final properties of the thick laminates.

MODEL VALIDATION VERSUS SCALED TESTS

Scaled compression tests from chapter 3 showed a slight enhancement of the ultimate stresses and a decrease of the fatigue properties with the thickness. Previously, it has

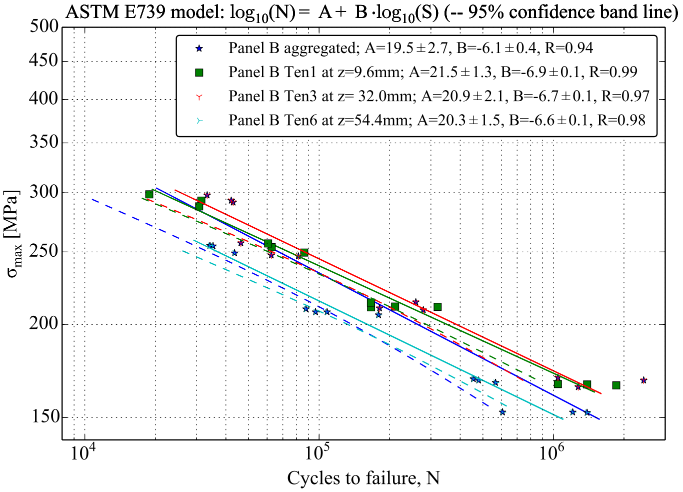

Figure 5.20: S-N curves of sub-laminate Ten1, Ten3 and Ten6 from panel B. (Tension-tension loading ratio).

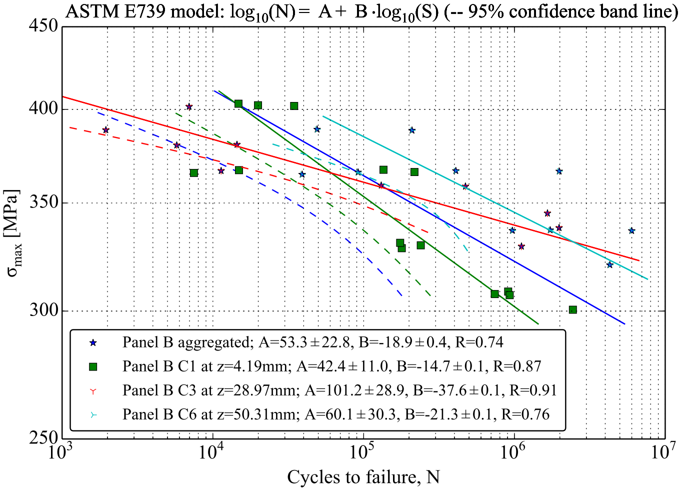

Figure 5.21: S-N curves of sub-laminate C1, C3 and C6 from panel B.

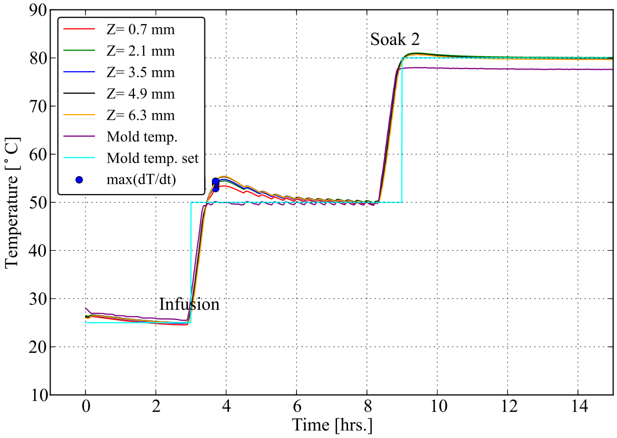

Figure 5.22: Temperature measurements during the manufacturing of scaled compression coupon 4 mm thick coupons. Maximum heating rates locations during the hardening are indicated with a dot $max(dT/dt)$.

been showed that the ultimate stress fields through the thickness vary according to the manufacturing conditions. In this section the model from the previous section, which relates the ultimate stress to the maximum heating rate during curing, is validated. For this purpose, the results obtained from the scaled coupon tests were studied using such model and following the flowchart from figure 5.19. This validation was limited to the scaled compression tests, since these showed a significant size effect.

SCALED COMPRESSION COUPONS TEMPERATURE FIELDS (CURING CYCLES)

Panels of 4 and 10 mm thickness were cured with a curing cycle prescribed by the resin manufacturer for the epoxy resin. The curing cycle was divided into two main stages. The first stage was the hardening stage, where the exothermal reaction of the resin takes place with a setup mould temperature of 50°C. The second stage was the post-curing stage, where the resin finalises the curing process with a setup mould temperature of 80°C. For the panels dedicated to 20 mm thick coupons, the initial hardening stage mould temperature was reduced to 35°C to avoid excessive temperatures due to the exothermic reaction and the thickness of the plate. Temperatures through the thickness were measured with embedded thermocouples during the curing. From these temperatures the maximum heating rates during the hardening stage ($max(dT/dt)$) were computed.

Figure 5.22 and figure 5.23 show the through thickness temperature measurements for 4 and 20 mm thick coupons plates. While the curves for the 20 mm thick coupons plate show clear influence of the exothermal process, those for the 4 mm coupons plate

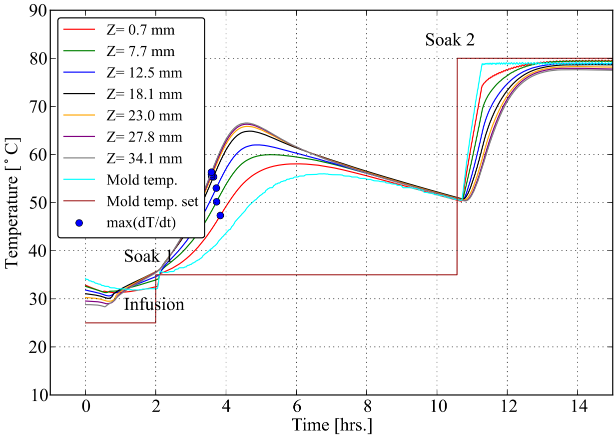

Figure 5.23: Temperature measurements during the manufacturing of scaled compression coupon 20 mm thick coupons. Maximum heating rates locations during the hardening are indicated with a dot $max(dT/dt)$.

show temperatures that are not much higher than that of the mould.

From the manufacturing temperature signals the maximum heating rates during the hardening stage ($max(dT/dt)$) were computed for each thickness position. Moreover, using the curve in figure 5.20 as a transformation function, the ultimate stresses through the thickness were calculated as shown in figure 5.24. It can be observed that while for the 4 mm coupons the internal variation in ultimate stresses due to the manufacturing is around 10 MPa, for the 20 mm thick coupons this variation raises to 25 MPa. Moreover, for a 60 mm thick laminate such variation can be up to 100 MPa as plate A and B from figure 5.20 shows.

FE VALIDATION. STATIC SCALED COMPRESSION TESTS.

Two mechanisms were considered as leading causes of final failure. First the grip effect due to the clamping pressure. Second, the influence of the curing cycle in the lamina compression properties through the thickness. To study these mechanisms, a 2D FE model was used (see chapter 3). One-quarter of the coupon geometry was computed with an equivalent load of 630 MPa in the gauge section as a boundary condition.

The clamping pressure and coupon geometry result in the gauge section a stress gradient through the thickness across the gauge section. The outer layers experience higher stresses than the inner layers. If constant ultimate stress values through the thickness are assumed, the outer layer shows a greater probability of failure. Figure 5.25 shows this stress gradient through the thickness. These stress gradients agree with the front and side

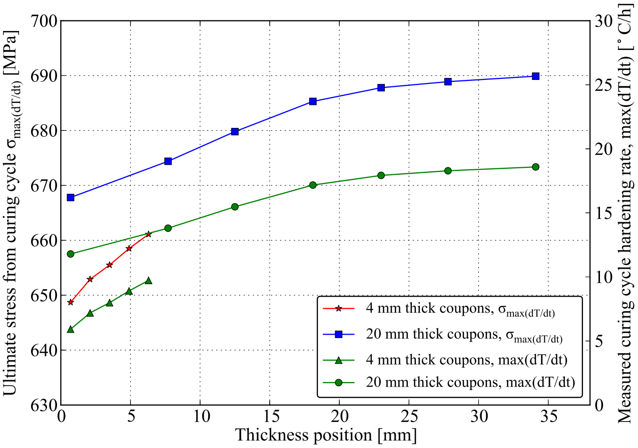

Figure 5.24: Ultimate stress and maximum heating rates during the hardening versus thickness position for 4 and 20 mm thick compression coupons.

face strain gauge measurements performed during the static tests. In the case of 20 mm thick coupons, differences around 20 to 30% were measured between the outer and the middle strain gauges.

Moreover, based on the stress fields the maximum stress failure criterion index was computed as an indicator. Figure 5.26 shows the criterion failure index computed for an ultimate stress of 630 MPa. In both cases, the 4 and 20 mm thick coupons show corresponding stress fields due to the scaling with an average failure index of 1 over the cross-sectional area.

Since ultimate compression stresses in thick laminates are not equal but vary through

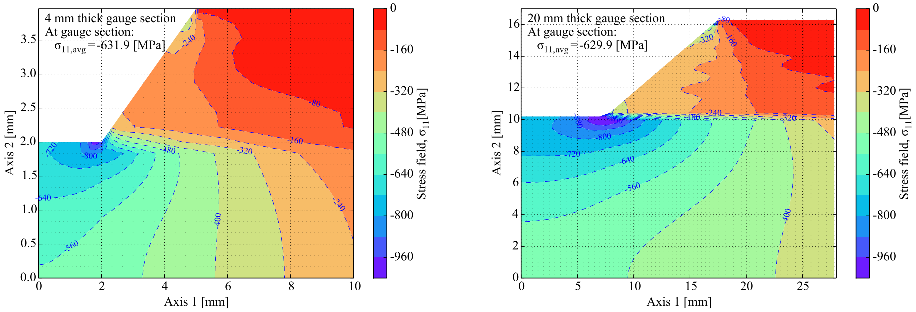

Figure 5.25: Stress gradients in the main fibre direction σ_{11} for 4 and 20 mm thick gauge section geometry at an equivalent load of 630 MPa.

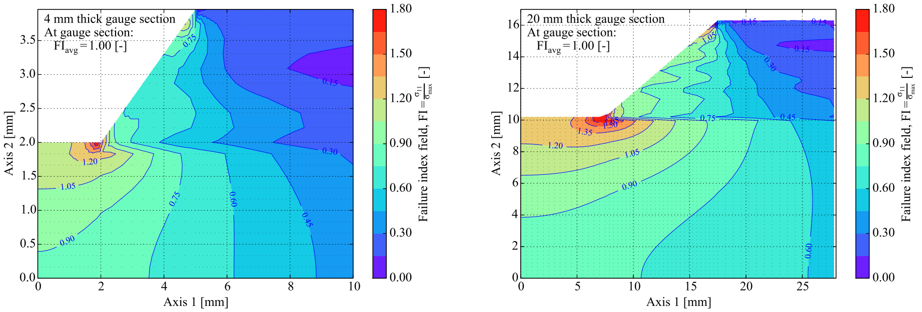

Figure 5.26: Stress max failure index in the main fibre direction σ_{11}. 4 and 20 mm thick gauge section geometry at an equivalent load of 630 MPa. Maximum ultimate stress at UD core 630 MPa, at tabs 315 MPa.

the thickness, the influence of the curing cycle in the mechanical behaviour of the coupons can be evaluated based on figure 5.24. Figure 5.27 show the maximum stress failure index modified due to the curing cycles for the 4 and 20 mm thick coupons. The new failure index relaxes in comparison with the previously computed values. Moreover, due to the influence of the curing cycle, the 20 mm coupons show an average failure index that is 4% lower than the 4 mm coupons. This difference agrees with the increase of the ultimate stresses observed in the static test for the 20 mm thick coupons versus the 4 mm.

Therefore, it is possible to scale the geometry to perform scaled compression tests with corresponding stress fields with equal ultimate stresses fields. However, when the manufacturing process is considered, the assumption of equal ultimate stresses across the thickness is not valid. Since thick laminates experience significant temperature gradients during manufacturing, and temperature gradients are not scalable. The manufacturing process, and, in particular, the curing cycles is identified as a variable that influence the thickness scaling.

FE VALIDATION. FATIGUE SCALED COMPRESSION TESTS.

Following the same approach as for the static tests (see the previous section), two mechanisms were considered as leading causes of final failure. First the grip effect and second the influence of the curing cycle. As a case study, a stress field at an equivalent load of 350 MPa based on a 2D model was computed. Due to the coupon scaling, the stress fields are equal in the case of 4 mm and 20 mm thick coupons. However, according to the experimental S-N curves 4 mm thick coupon achieved $3.87 \cdot 10^6$ cycles and 20 mm thick coupon achieved $1.32 \cdot 10^3$ cycles before failure.

To study this discrepancy, the stress fields were converted into cycles to failure using a single experimental S-N curve per case. This numbers of cycles to failure was normalised

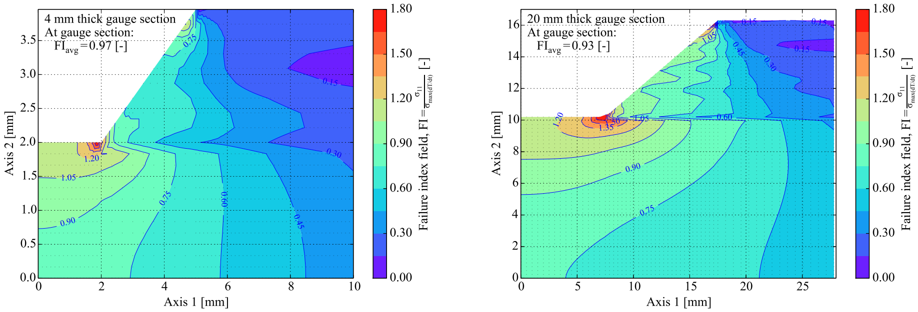

Figure 5.27: Stress max failure index in the main fibre direction σ_{11} corrected with the curing cycles ultimate stresses. 4 and 20 mm thick gauge section geometry at an equivalent load of 630 MPa. Maximum ultimate stress at UD core 630 MPa, at tabs 315 MPa.

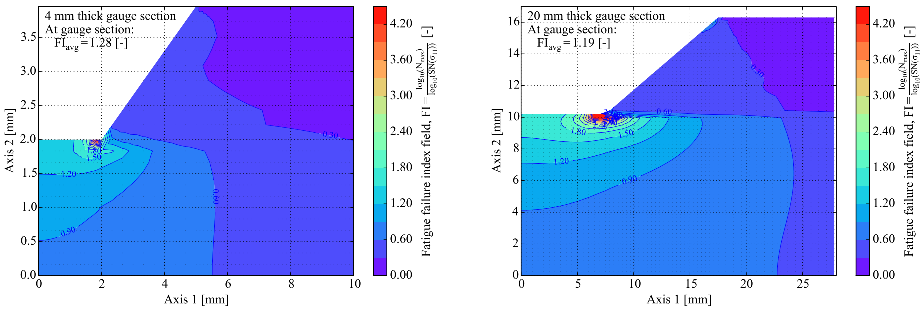

Figure 5.28: Fatigue failure index in the main fibre direction σ_{11}. 4 and 20 mm thick gauge section geometry at an equivalent load to 350 MPa and $N_{max} = 3.87 \cdot 10^6$ cycles. Left and right plots computed with S-N curve of milled 4 mm thick coupons.

into a fatigue failure index defined as,

$$FI_{fatigue} = \frac{log_{10}(N_{max})}{log_{10}(SN_{(\sigma_{max})})} \tag{5.2}$$

where N_{max} is the reference number of cycles and $SN_{(\sigma_{max})}$ is the S-N curve function belonging to the maximum stress.

Figure 5.28 shows the fatigue failure index fields computed as the ratio of the reference number of cycles ($N_{max} = 3.87 \cdot 10^6$) and the number of cycles computed according to an S-N curve and the stress field. The fatigue failure indexes from figure 5.28 were calculated using the experimental 4 mm coupon S-N curve (see chapter 3). Therefore, it is assumed that the 4 mm S-N curve is representative for the 20 mm thick coupon fatigue life. The figure shows same failure indexes for the 4 mm and 20 mm thick coupons due to the stresses

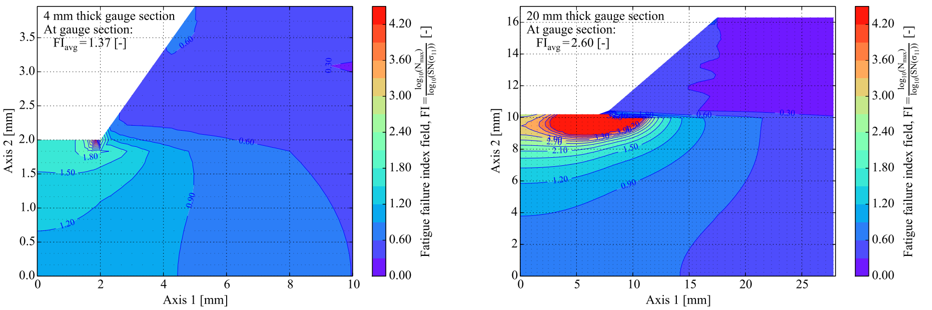

Figure 5.29: Fatigue failure index in the main fibre direction σ_{11}. corrected with the curing cycle influence. 4 and 20 mm thick gauge section geometry at an equivalent load to 350 MPa and $N_{max} = 3.87 \cdot 10^6$ cycles. Left plot (4 mm) computed with S-N curve of a laminate cured at a maximum hardening rate between 8 and 16 °C/h and right plot (20 mm) computed with S-N curve of a laminate cured between 25 and 37 °C/h.

caused by the grip effect. Hence, the grip effect does not explain the reduction in fatigue life of the 20 mm coupon in comparison with the 4 mm thick coupons.

Since figure 5.18 shows that fatigue properties (S-N curves) through the thickness are influenced by the manufacturing process, the fatigue failure indexes were computed according to such S-N curves. Figure 5.29 shows the fatigue failure index computed with two S-N curves associated with two different curing cycles, plate B C1 and plate B C3.

In the case of the 4 mm thick coupon, an S-N curve obtained from a sub-laminate cured with heating rates between 8 and 16 °C/h was used (plate B C1). The 20 mm thick coupon failure index was computed with an S-N curve from a sub-laminate cured with heating rates between 25 and 37 °C/h (plate B C3). Since the S-N curves are influenced by the curing cycle, figure 5.29 shows strong differences between the fatigue failure indexes for 4 mm and 20 mm thick coupons.

While 4 mm thick coupons show similar failure indexes to the ones computed with the 4 mm milled coupon S-N curve, 20 mm thick coupons show a strong increase in failure index which almost doubled. This indicates earlier failure for the 20 mm thick coupons in comparison with the 4 mm coupons due to the curing cycle influence.

Conclusions

Thick laminate panels (80 layers thick) were manufactured with two different curing cycles. From the thick laminates panels, sub-laminates (10 and 4 layers thick) were extracted with the help of peel-ply layers (sub-laminate technique). The temperature was monitored at different thickness positions with thermocouples. The temperature monitoring allowed to observe the temperature profiles through the thickness caused by the exothermic curing cycles. These measurements made it possible to link each sub-laminate plate with a specific local curing cycle and a thickness position.

The sub-laminate plates were transformed into specimens and tested in tension σ_{t11}, compression σ_{c11} and interlaminar shear τ_{13}. While ILSS and compression ultimate strengths revealed a strong correlation with thickness position, tension tests did not show a correlation with thickness position. A plausible explanation is that shear and compression are influenced by the matrix while the fiber dominates UD tension properties. The same behaviour was observed in fatigue tests.

The sub-laminates technique allowed to study how mechanical properties vary through the thickness. Because the thickness position has a correspondence with the local curing cycles and local heating rates. A strong correlation was found between strengths and heating rates during the matrix hardening. The relation was proposed to be modelled as a linear function and a plateau.

For the investigated laminate a maximum heating rate was found to be proportional to the curing rate, which means that this correlation can be related to the effect of curing rate on polymer properties.

Scaled compression tests from chapter 3 were studied according to the heating rates model. For that purpose, the heating rates through the thickness of the 4 and 20 mm thick coupons were experimentally recorded with thermocouples and the ultimate stresses through the thickness computed from the sub-laminates tests data. Next, 4 and 20 mm thick coupons FE models with and without taking into account the variation of the ultimate stresses through the thickness due to the different local temperature histories. The influence of the manufacturing effect was identified as a possible cause for the scaled effect found in the scaled compression tests from chapter 3.

Since the strength field is a function of the manufacturing conditions and the stress field is a function of the boundary conditions, scaling a structure with equal stress fields is possible. However, if the strength fields are not equally scaled via a manufacturing process optimisation, failure will not be equal.

The variation of the mechanical properties or scatter through the thickness of a laminate was described as an inherent characteristic of composites. This holds in particular for thick laminates, where temperature gradients during curing are larger, and the mechanical properties distributions through the thickness become wider.

6

CONCLUSIONS

Differences in the mechanical behavior of thin and thick laminates were found for epoxy GFRP composite laminates due to the thickness scaling. Two mechanisms which drive the thickness scaling effect have been reported, the manufacturing influence due to curing and the self-heating effect.

Test setups and coupon geometries were investigated using FE methods in order to find a suitable setup for the scaled mechanical tests. Mechanical testing of thick laminates is limited, since specific test frame and specific clamping systems designs are necessary to apply high loads.

The influence of manufacturing of thick laminates was studied using the sub-laminate technique. The sub-laminate technique was developed to deconstruct a thick laminate through the thickness into thin plates that can be tested as standard coupons. Laminates of 65 mm thick were sub-divided into thin laminates coupons, where each sub-laminate was referred to a particular thickness position. The sub-laminate technique has the advantage that sub-laminates can be tested according to thin laminates standards and devices but are related to thick laminate properties. Due to the exothermic resin curing process, temperature gradients were measured inside the thick laminates during the manufacturing (with embedded thermocouples). Observations of strength fields through the thickness and temperature gradients due to the manufacturing were combined to study the influence of local curing cycles on mechanical properties. Correlation was found between compression and shear properties and the maximum heating rate. This manufacturing indicator contains similar information as the curing rate, which is known to characterize the resin structure during hardening after gelification. A model was proposed that relates the ultimate compression or shear strength to the curing rate composed of a linear function and a plateau. For tension tests on the sub-laminates no influence of thickness position on material performance was found. This is related to the fact that results of tension tests are strongly fibre-dominated, which means that the matrix curing history is less relevant.

According to the sub-laminates observations, it was concluded that when a thick laminate is manufactured a non-uniform strength distribution due to the spread in the curing thermal history can be expected. When a structure is scaled, equal stress fields are possible. However, if strength fields are not equally scaled due to the manufacturing process, the failure stress and failure modes will not be equal. Therefore, the description of the behavior of a thick laminate with a unique ultimate strength (per tensor component) is less reliable than of thin laminates. This is due to the influence of the manufacturing thermal history in the strength field. Similar behaviour was observed for fatigue properties, where compression S-N curves of sub-laminates through the thickness showed significant differences. Thus, the assumption of using a single S-N curve obtained from measurements on a thin laminate to describe the fatigue behaviour of thick laminates is an inaccurate approach which needs to be accompanied by safety factors.

Thickness scaled tests were carried out in tension and compression for epoxy UD GFRP up to 20 mm thick. Thickness scaled tension tests did not show statistically representative thickness scaling effects. This agrees with the observations of the sub-laminates tests where tension sub-laminates S-N curves through the thickness showed no thickness effect. On the contrary, thickness scaled compression tests did show a scaling effect in quasi-static tests as well as in the fatigue S-N curves. These thickness effect observations were studied taking into account the manufacturing process influence and curing thermal history which both provided a plausible explanation. Regarding the relevance of the thickness effect in fatigue, reserve factors lower than 2.0 were observed for 20 mm thick coupons when compared with GL design rules. This yields safety factors between 1.23 and 1.6 (for DNV-GL design rules model) due to the thickness effect for the compression properties of the investigated material.

To perform the thickness scaled tests, setups and coupon geometries were investigated. In the case of thick tension coupons thick tabs as well as large grip areas are recommended to reduce the grip effect. In the case of thick compression coupons, coupons manufactured with integrated tabs were found to have similar properties as coupons with bonded tabs. Regarding the compression coupons geometry tapered tabs, short gauge sections and thick long tabs are recommended. In performing the mechanical tests, it was observed that the clamping pressure plays a major role in the determination of the compression ultimate strength, in particular for compression tests with a combined loading setup.

Self-heating was studied as a second source of scaling effects in fatigue. When a composite structure is loaded in fatigue, a part of the strain energy is transformed into heat due to non-reversible processes. The hysteresis area loss factor and the strain energy density was linked to the internal volumetric heat that causes the material heating. This assumption was validated via experimental tests. In the case of composite structures loaded in fatigue such as wind turbine blades spar caps, there is a rise in internal laminate temperature due to the self-heating effect and the thermal isolating properties of composites. When internal temperatures approach the matrix glass transition temperatures, mechanical properties degrade, promoting failure. Because of the fact that self-isolation is thickness dependent, self-heating can influence the size effect in fatigue tests.

The self-heating effect was observed in experimental tests where two structures with different thicknesses but equal dynamical loads and equal thermal boundary conditions showed different failure mechanisms due to the internal temperature rise. Moreover, a FE method to predict the temperature distribution due to self-heating was proposed and evaluated against experimental observations. The ability to describe the self-heating effect is relevant for the design of reliable fatigue tests for thick laminate components and structures.

In order to characterise fracture in DCB tests a tool was developed able to measure the crack length using image processing. In addition, a tool was developed to monitor coupons during fatigue with thermography and post-process them in the frequency domain. In both cases, it was possible to measure quantitative indicators of damage such as delamination lengths or areas during experimental tests. Further research on image processing and NDT techniques in performance analysis of test setups and materials is suggested.

RECOMMENDATIONS FOR DESIGN AND ENGINEERING

Based on the current research, the following recommendations are given for designing and testing of thick laminates, with emphasis on wind turbine blades:

- During fatigue tests of sub-components and full-scale components which include thick laminates e.g. blade tests, it is recommended to assess the effect of self-heating. A recommended approach is to measure the surface and ambient temperatures, and limit the loading times or test frequencies according to the inner material temperature. This is particularly recommended for tests carried out in large test halls or outside, where environmental temperatures can vary strongly depending on the season or the night-day cycles. Therefore, to evaluate the inner material temperatures in complex structures a FE method is proposed (section 2.3) or alternatively temperatures can be analytically computed (see equation 2.9).
- Thick laminates showed a variation in strength and fatigue properties through the thickness which is related to the manufacturing history and matrix dominated properties. Therefore, regardless of the modelling technique, the assumption of a unique strength per stress tensor component to characterize the behavior of a thick laminate is an inaccurate approach that requires additional safety factors.

- To test thick laminates in tension or compression, with a straight coupon shape and regarding static or fatigue properties, it is recommended to select geometries according the following criterion,

  $$m = \frac{\sigma}{\tau} \cdot \frac{e}{2} \cdot TF \tag{6.1}$$

  where m is the clamped length tab, e is the thickness of the cross-section, σ is the expected cross-sectional strength, τ is the most critical shear allowable of the resin matrix or the adhesive used for tabbing and TF is the test factor. TF is recommended to be equal or larger than 1.4 for CLC compression and larger than 1.1 in tension. Larger TF and low τ will result in conservative results but increase the complexity of the clamping system.
- Guidelines and standards used to indicate that the coupons used for the characterisation of a material should be manufactured under the same conditions as the final part. However, it is not possible to match the manufacturing conditions of a thick laminate with a thin laminate. The coupons obtained with the sub-laminate technique offer a more reliable characterization of the potential mechanical properties that can be found in a thick laminate than coupons manufactured from thin laminates. The sub-laminate technique is recommended as the best method to determine the critical design of a thick laminate with a particular curing cycle and manufacturing method.
- In a similar manner, instead of using coupons manufactured as thin laminates, the sub-laminates technique is recommended to be used to determine the critical designing S-N curves that can be found in a thick laminate manufactured according to a particular curing cycle and manufacturing method.
- In the design of a fatigue test, a choice must be made for the test frequency. In particular for thick laminates or large structures, test frequencies and environmental temperatures can influence the behaviour. However, literature and standards are vague regarding fatigue tests frequencies at coupon, sub-component and component level. Therefore, it is recommended to choose the test frequencies avoiding the self-heating effect.

6

* * *

RECOMMENDATIONS FOR FURTHER RESEARCH

Regarding the failure behaviour of a thickness scaled composite structure, the following further research topics are recommended:

Test design

Test methods and coupon geometry showed to have a strong influence on the mechanical characterisation of composites laminates. To carry out a mechanical test the specimen needs to be clamped to the test machine. The clamping distorts the ideal stress field that characterizes the mechanical property to be measured, which complicates the interpretation of measurements. For thick laminates nominal forces become larger and coupons, clamping systems and tests setups need to be scaled. Therefore, to test thick laminates improved clamping designs are needed.

Moreover, standardization for GFRP fatigue tests setups and thin coupons geometries for different loading ratios (such as 0.1, 10 and -1) is recommended.

Regarding scaled compression tests it is advised to test thicker coupons to collect more information on the thickness effect. Testing of 30 or 40 mm thick coupons will help to interpret the fatigue life reduction of thick laminates. However, such tests require a larger clamping system which was not available for this project.

Influence of thermal history

From a process engineering point of view, further research on curing processes modelling and final properties optimization is needed. Comparison between the final properties that result from different mould materials with similar set curing cycles is also suggested. In addition, further study is suggested on failure modes in thick laminates where non-uniform strength fields through the thickness are considered in bending and torsion loading cases.

Regarding the modelling of composite laminates, considering non-uniform strength fields, that are dependent on the manufacturing process is an open line of research, from a micro-mechanics point of view regarding the matrix and from a macro-mechanics point of view regarding the laminate. In section 5.4 the influence of non-uniform strength on laminate failure was studied in a simplified way. It is recommended to perform detailed progressive failure analysis with spatially varying properties as input.

Further research is required regarding the sub-laminates to evaluate the properties through the thickness for other fiber-resin systems, as well as further research on the properties of the tensor components related to the resin properties.

Self-heating

Although semi-adiabatic tests showed a clear reduction in mechanical properties due to self-heating, further work is recommended regarding the insulation method and a test setup that allows an integral measurement of the surface temperatures. Also, further work is needed regarding the measurements of convection coefficients and material thermal properties for coupons loaded in a test laboratory environment. Additional research on these topics would allow a finer evaluation of the proposed FE method and self-heating model, as well as a better understanding of the significance of the energy loss factor included in the mentioned model.

A

APPENDIX A. AUTOMATED DELAMINATION LENGTH TOOL FOR DCB TESTS

In order to measure the delamination length in mode I static and fatigue tests, different systems such as the visual methods, embedded fibre Bragg grating sensors and crack gauges are available. These methods have various disadvantages in terms of reproducibility, measurement range, fatigue sensitivity, and cost. The aim of this work is to describe a technique for measuring the delamination length in mode I tests, based on video image processing. Video image processing allows non-contact continuous crack length monitoring in static tests and for the entire fatigue crack propagation curve. A set of static and fatigue tests carried out with the developed method is included in the present work. The static fracture toughness G_{IC}*, the* $G-N$ *fatigue onset curve and the fracture energy rate versus the crack growth rate* da/dN *for epoxy glass fibre reinforced composites are reported. Results show that visual image processing is a stable technique for facilitating the post-processing of static and fatigue mode I tests.*

INTRODUCTION

This work proposes video image processing as a non-contact technique to measure the full delamination length in mode I static and fatigue tests. This offers a reliable measurement in comparison with conventional visual or strain gauge methods and allows to characterise the full delamination length in mode I fatigue crack propagation tests with high signal sampling rates.

The work is divided in two main parts: the description of the video image processing technique and the validation of the technique through static and fatigue tests for an epoxy

---

This chapter is extracted integrally from [12].

glass-fibre reinforced composite. In section A.2 the tests and the video image processing technique (section A.2.1) are described. The video image processing technique outputs a high sampling rate crack length (a) signal. The different data processing methods to calculate the fatigue test parameters (G and da/dN) from the crack length (a), the static and fatigue test results and the evaluation of the technique are discussed in section A.3.

BACKGROUND OF MODE I CRACK GROWTH

Quasi-static mode I tests described in ASTM D5528, are based on the energy criterion for crack length described by Griffith [142] where the calculation of the strain energy release rate G is described as the differential of the strain energy U divided by the crack delamination length differential. By O'Brien [143], three main crack initiation criteria were defined: the non-linear criterion (NL), the 5% offset of the maximum load (5%) and the visual criterion (VS). Moreover, in order to derive the fracture energy rate different methods have been proposed to evaluate these equations applying the beam theory model such as: the Berry method [144] and the modified beam theory (MBT) [145, 146], the compliance calibration method (CC) [147] and the modified compliance calibration method (MCC) [148]. These are given by the following expressions:

$$G = \frac{nP\delta}{2ba} \; ; \; \frac{\delta}{P} = Ka^n \text{ [CC]} \tag{A.1}$$

where P is the load, δ is the displacent, b is the coupon width, a is the delamination length and K and n are the coefficient of the compliance CC calibration curve,

$$G = \frac{3P\delta}{2b(a+|\triangle|)} \; ; \; \left(\frac{\delta}{P}\right)^{\frac{1}{3}} = Ka + |\triangle| \text{ [MBT]} \tag{A.2}$$

where K and $\triangle$ are the coefficient of the compliance MBT calibration curve,

$$G = \frac{3P^2C^{\frac{2}{3}}}{2A^1bh} \; ; \; \frac{a}{h} = A^1\left(\frac{\delta}{P}\right)^{\frac{1}{3}} + cte \text{ [MCC]} \tag{A.3}$$

where C is the compliance, h is the coupon thickness and A^1 and cte are the coefficients of the compliance MCC calibration curve.

Mode I fatigue tests are based on the same coupon geometry as static mode I tests, and can be divided in two different types: the delamination growth onset test and the crack propagation tests. The mode I fatigue delamination growth onset test is described by the standard ASTM D6115 [149] where a series of fatigue tests results can be represented as a $G-N$ curve that describes the start of the delamination growth as a function of the fracture energy rate. The mode I fatigue crack propagation tests are described by the crack propagation curve da/dN vs. G, which is divided in three different regions [150]: the threshold, the linear and the fast fracture region. Both are commonly associated with the Paris relationship [150–152] described by the Paris relationship [153] (eq. A.4) where A and m are constants and G_{max} is the fracture energy rate per cycle at maximum load or displacement.

$$\frac{da}{dN} = AG_{max}^{m} \text{ [Paris relationship]} \tag{A.4}$$

In both cases, the onset and propagation tests, delamination length monitoring is required in order to compute the fracture energy rate G and the crack growth rate da/dN.

METHODS FOR CRACK LENGTH DETERMINATION

Currently, in order to measure the delamination length a, different systems are available such as visual methods and methods using crack gauges. The visual methods based on human observation with or without optical microscopes [154, 155] present several disadvantages:

- they require to mark the coupons precisely;
- in order to perform the readings tests have to be stopped periodically;
- low crack length sampling rates in static and fatigue tests are common;
- the human interaction adds subjectivity to the measurement;
- synchronisation of the load-displacement signal from the test equipment with the crack length signal may be an issue.

Using crack strain gauges for the observation of crack length eliminates the problem of synchronisation and subjectivity, but these sensors are limited in size and thus cannot always measure the full coupon delamination length. In fatigue tests they become unreliable due to fatigue of the sensor.

Embedded Bragg fibres have been reported as a method to characterize the initial threshold region in mode I fatigue tests as recently proposed Sans et al. [156]. Both, crack gauges and Bragg fibres perform discrete measurements of the delamination length for a very limited number of experimental points usually complemented by visual techniques and interpolations. The local gauge positioning with respect to the initial crack front needs to be measured before the processing of the material, which is slightly more straightforward in surface-mounted crack gauges than in embedded Bragg fibres [157]. The advantage of Bragg fibres is that they are more fatigue resistant. Both Bragg sensors and crack gauge sensors are single-use sensors and require expertise and effort to apply.

As a potential alternative to the conventional visual systems, Yarlagadda et al. [158] developed a time domain reflectometry system which requires to equip the coupons with wires and allows automated delamination length measurements. Based on image processing techniques, Uhlig et al. [159] developed a system for crack tracking in neat resin fracture toughness coupons, based on a particular illumination system for transparent coupons. Richter et al. [160] also describe a set of image processing trials for static adhesive mode I coupons. In those trials different image processing algorithms were tested with varying success and the final measurements of the images was carried out manually. Other experiences have been reported on optical crack tracking by Dare [161] for concrete coupons and by Ryu [162] to estimate residual life in industrial facilities.

METHODOLOGY

In this section, the method and test set-up used for the automated crack length determination are described. The method was carried out on static and fatigue Mode I tests on representative wind energy material samples.

DETERMINATION OF THE DELAMINATION LENGTH VIA IMAGE PROCESSING

The videos of the tests were processed by an algorithm based on image processing techniques. The code was built in Python 2.6.3 [163] and OpenCV [164], and its final output was the crack length signal synchronized with the force and displacement signals of the data acquisition system. Measures were taken to maximise the accuracy of the measurement:

- the coupon was painted in white and the background was black, to maximize contrast between coupon and background;
- illumination was controlled in order to avoid shadows;
- reflections were avoided using a matte paint;
- brittle plastic paints were used in order to follow the coupon crack length accurately;
- the coupon was oriented perpendicular to the camera and filled more than 50% of the total image width. The coupon size was 120mm, this dimension corresponds to around 1000 pixels in the image, so the maximum resolution is ±0.12mm;
- the initial crack tip in the coupons was marked by a dark line.

The process can be described by the following logic workflow:

- Each video frame was considered as a raw image which is synchronized with a timestamp value that was also recorded in the load and displacement measure-

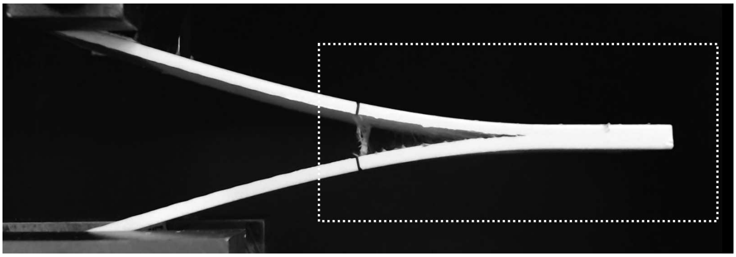

Figure A.1: Mode I coupon raw image (dashed square defined by the user).

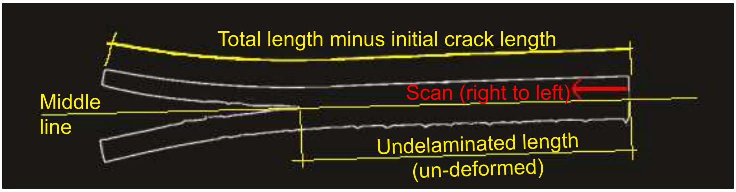

Figure A.2: Mode I coupon binary image processed contour. Determination of the crack tip.

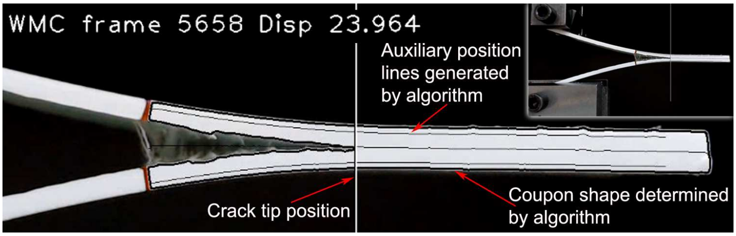

Figure A.3: Diagram of the auxiliary lines.

ments with signal synchronization purposes. The area where the growth of the crack is predicted to occur was cropped (see Figure A.1).

- For each frame the image was filtered to determine specimen contour. An initial threshold filter by colour was applied [165]. Secondly a Canny filter with a Gaussian kernel of 5x5 pixels [166] and to finalise the filtering an Otsu threshold [167] was used. The result was a contour shape of the coupon and the delamination (see Figure A.2).
- Auxiliary lines were constructed inside the contour, offset top and bottom lines were calculated and used as auxiliary lines with reduced distortion (see Figure A.3). Based on the top and bottom line a middle line was calculated.
- The crack tip is found by scanning the contour binary image along the centre line from the right side to the left side starting at the end of the coupon. In this way the un-delaminated length is obtained as shown in figure A.2. Because the distance between the coupon and the camera is always the same, the distances measured in pixels can be transformed into millimetres by a constant coefficient which is calibrated with the initial frames taken before the test.
- Taking into account that the un-delaminated part is not deforming, the deformation of the DCB coupon arms does not influence the measurement of the un-delaminated length. Therefore the delamination length increment is calculated as the coupon length minus the initial delamination length minus the un-delaminated length.

MATERIAL

Nominal ASTM D5528 size coupons were used in the static and fatigue tests. Two different plates (batch TP and VN) were infused with a common wind energy epoxy resin and type E unidirectional (UD) glass fiber (GFRP) of 600gr/m2 non-crimp fabric. The layup was 6 UD layers, with the UD roving facing the crack. A 50 microns Teflon© layer to induce the initial crack length (a_o, nominal length 65mm) was used. Average fibre volumes of 43% with glass transition temperatures of around 82°C was tested in both plates. Steel blocks of 20x20x20mm were bonded to the coupons with a cyanoacrylate adhesive.

TEST SETUP

The coupons were painted with a brittle white matte spray paint and the initial crack length was marked with a dark marker pen. A colour high definition USB© camera was used to measure the crack length signal as figure A.4 shows. The videos were encoded in a high quality AVI container with 1920x1080 resolution.

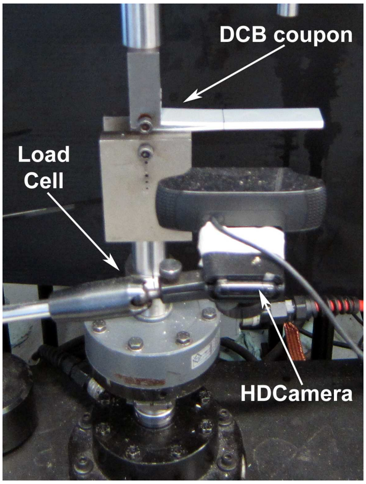

Figure A.4: Test setup.

STATIC TEST CONFIGURATION

Nine coupons were tested in mode I according to ASTM D5528. Tests were carried out at test speeds of 3mm/min. The tests started with an initial loading until crack initiation, next the coupon was unloaded and finally the load was applied from zero load until failure or maximum machine displacement.

The tests were performed in an MTS 10kN maximum capacity test frame with a 1kN class I load cell. The load and displacement signals were recorded with the in-house developed data acquisition software WMCS 0.3 [168].

FATIGUE TEST CONFIGURATION

The DCB fatigue tests were performed at constant displacement amplitude at an ambient temperature of 23°C. Based on the average displacement at maximum force recorded in the static tests, the fatigue test was designed for 11 coupons at different displacement ratios (the ratio between the square maximum displacement in the fatigue test and the square average displacement at maximum load in the static tests) between 0.6 and 0.1 (see table A.1). The coupons were tested approximately between 500.000 and 3.000.000 cycles.

Tests were performed at a frequency of 1.5Hz, and 15 seconds of video and data were recorded at intervals of 100-500 cycles below 200.000 cycles and at intervals of 5000 cycles above the 200.000 cycles. The force and displacement sampling rate was 800Hz and the video frame rate was 7fps.

In addition, the delamination growth onset was determined per the ASTM D6115

Coupon Id	Disp. ratio	Max. cycles	Coupon Id	Disp. ratio	Max. cycles
VN06I30	0.60	2.728.762	VN15I30	0.10	813.959
VN07I30	0.60	385.124	VN16I30	0.35	1.164.99
VN08I30	0.60	1.642.590	VN17I30	0.35	1.418.630
VN09I30	0.50	1.681.130	VN18I30	0.20	550.492
VN10I30	0.50	1.395.939	VN19I30	0.20	909.206
VN14I30	0.10	857.604	-	-	-

Table A.1: Fatigue mode I test matrix.

standard [149] in order to obtain the delamination growth onset $G-N$ curve, which describes the starting cycles of the delamination for a certain strain energy release rate G. Based on the video image delamination length signal a, the visual starting cycles were gathered as the first observed crack initiation cycle or at cycle $a > a_o + 1$.

The required signal processing in order to obtain the crack propagation and the delamination growth onset plots is summarize in the workflow chart in figure A.6.

TWO DIFFERENT METHODS TO CALCULATE ENERGY RELEASE RATE

According to Ashcroft [150] the fracture energy release rate G_{max} can be obtained as eq.A.5. The differential of the compliance with the crack length, da/dN, is calculated with a third order polynomial fit of the compliance versus crack length curve and the subsequent model differentiation. Moreover, due to the high sampling rate that the video crack length measurement allows, a second method to calculate the G_{max} was feasible. This second method is based on the differentiation of the strain energy U (eq.A.6) with a power law fit.

$$G_{max} = \frac{P_{max}^2}{2b}\frac{dC}{da} \text{ ; [Compliance method]} \tag{A.5}$$

$$G_{max} = \frac{1}{b}\frac{dU_{max}}{da} \text{ ; [Strain energy method]} \tag{A.6}$$

DETERMINATION OF CRACK GROWTH RATE da/dN

In order to perform the differentiation of the crack length with respect to the number of cycles the ASTM E647-86a [169] describes two different methods: the secant method and the incremental polynomial method. Both numerical differential methods require a linear or polynomial fitting along the dataset in order to obtain the slope. Alternative to these two methods and taking into account the shape of the graph of crack length (a) versus cycles (N) shown in figure A.7, the crack growth rate da/dN was calculated by fitting the whole curve with a power law model and differentiating the curve model.

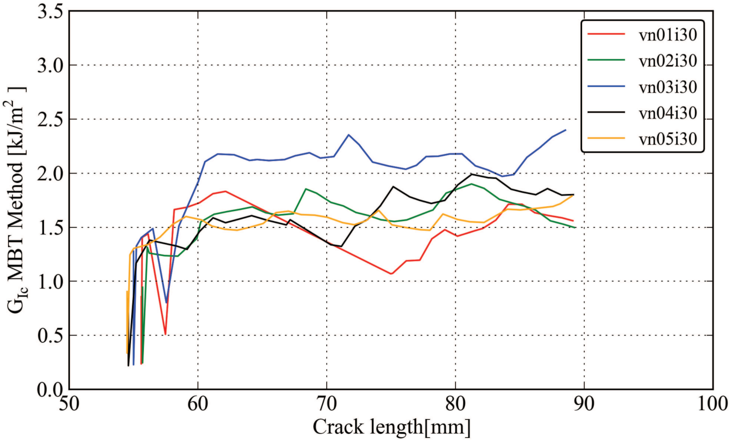

Figure A.5: Typical delamination resistance curve (R curve) from mode I static test.

Batch (panel)	F_{max}	δ at F_{max}	Type	G_{IC} MBT	G_{IC} CC	G_{IC} MCC
	[N]	[mm]		$[kJ/m^2]$		
TP	80.59	15.46	NL	0.171	0.180	0.193
			VS	1.133	1.182	1.208
			5%	0.883	0.921	0.949
VN	72.81	15.68	NL	0.228	0.248	0.255
			VS	1.164	1.274	1.256
			5%	0.872	0.945	0.942

Table A.2: Energy release rate averages results for static DCB tests.

RESULTS AND DISCUSSION

STATIC TESTS

Typical fracture energy release rates results are shown in table A.2. While the averages do not show significant differences between the three standard calculation methods, large differences are observed, depending on the choice of crack initiation criterion. Due to the very early loss of linearity of the load displacement curve, application of the non-linear criterion (NL) exhibits lower G_{IC} values than the visual (VS) or 5% offset criteria. Despite the fact that the TP coupons batch shows higher coefficients of variation than VN coupons batch, both sets are characterised by similar average results with differences lower than 10%.

The crack length measured via image processing is used in the visual criterion and in the determination of the delamination resistance curves (R-curve) shown in figure A.5. The R-curves show the characteristic energy release rate plateau. Between the crack lengths of 56 to 59 mm a depression is observed for all specimens, caused by the loading

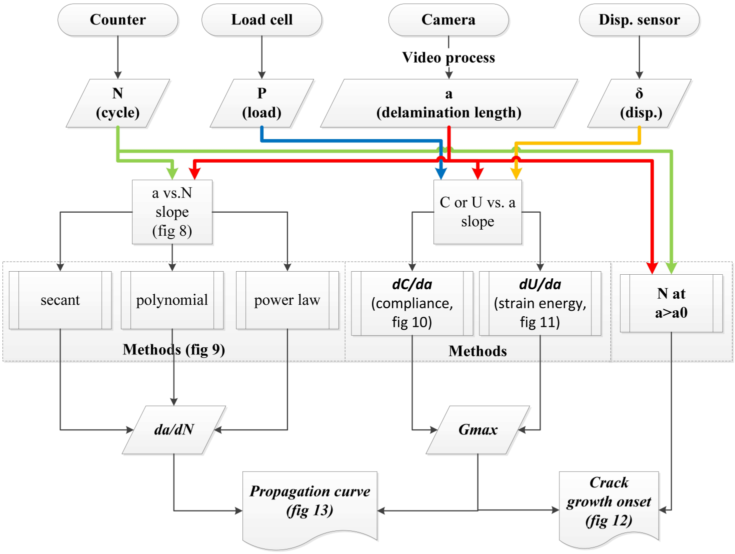

Figure A.6: Signals workflow process in fatigue. Image processed delamination length a influence each one of the calculated values which describes the crack propagation and the crack growth onset.

and unloading cycle that the standard requires. The R-curves and the load vs. displacement plots show a slight crack length growth stick and slip behaviour which was monitored via image processing, showing a good synchronization between the signals.

FATIGUE TESTS

Displacement at maximum force from the static test is subsequently used for the determination of the different loading ratios and fatigue test design. The signal processing required to gather the fatigue parameters that describes the crack progation and crack growth onset results is showed by the workflow chart of figure A.6. The flow chart exhibits how the automated image processed delamination length signal is involved in each one of the parameters such as the fracture energy release rate G and the crack growth rate da/dN.

The crack growth rate da/dN is related to the curve slope shown in figure A.7, where the continuous monitoring via image processing of the crack length versus the cycles is plotted for each coupon. In order to compute da/dN three different methods were used. The results of the secant method, incremental polynomial method and direct differentiation of a power law model method are plotted in figure A.8 for one of the coupons. While the three methods present similar trends in all the coupons, the average R correlation coefficients between the three methods is around 0.59 due to the high dispersion that the secant and incremental polynomial method introduce in the comparison. In addition, it

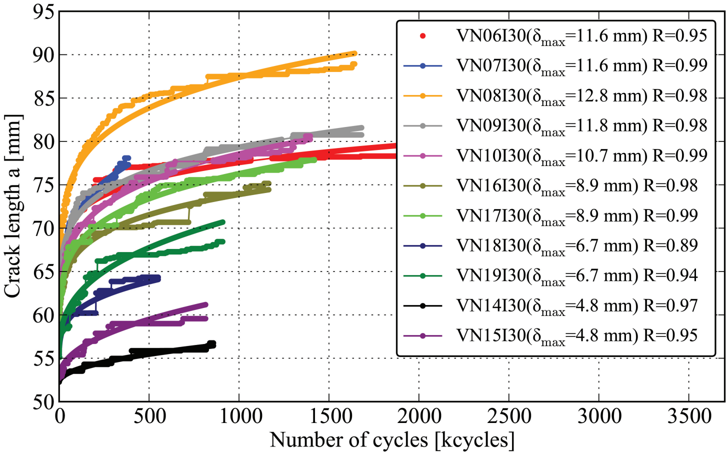

Figure A.7: Crack length versus cycles at different loading ratios and power law fittings with *R* correlation coefficient values.

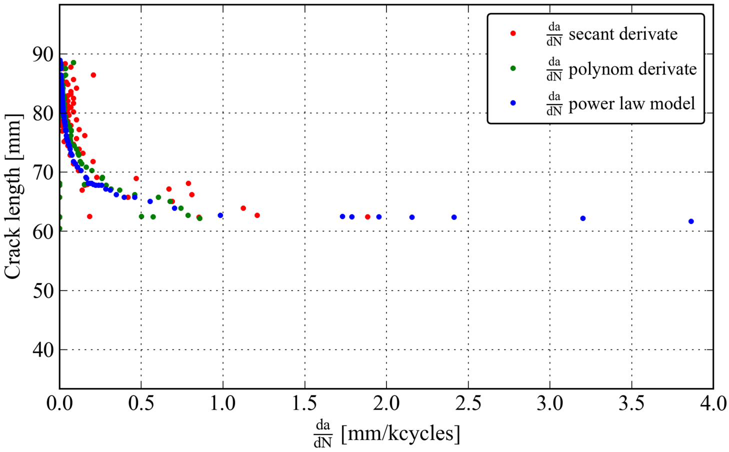

Figure A.8: Crack growth rate calculation methods, secant derivate, polynomial derivate and power law model. Coupon VN08I30.

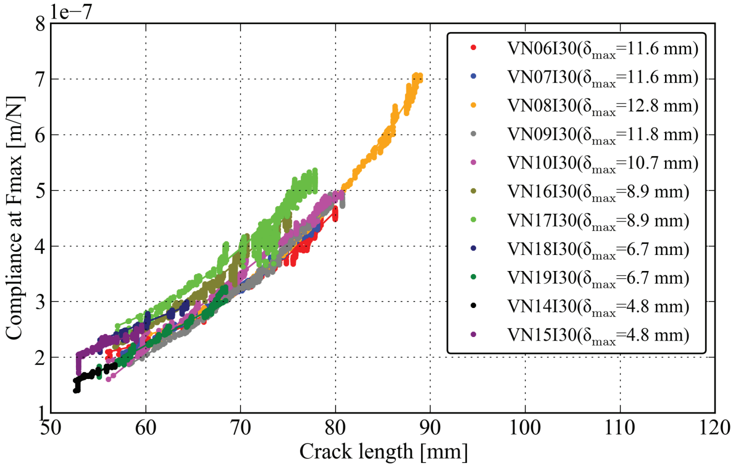

Figure A.9: Compliance at F_{max} versus crack length. Experimental and fit curves.

	Crack propagation slopes			
	secant	polynomial	power law	dU/da
Average	4.72	6.20	6.40	5.26
COV [%]	58.4	46.1	33.9	33.8

Table A.3: Crack propagation slopes for each computation method (where COV is cofficient of variance).

was observed that despite some stick and slip behaviour, the crack length growth versus the cycles follows a power law model in all the tested coupons with an average R correlation coefficient value of 0.93.

Table A.3 shows the average slopes according a Paris relationship for the three different cases of crack growth rate calculations versus the compliance strain energy release rate method. The secant method shows the biggest differences in comparison with the others, it presents higher dispersion than the others and in some coupons was not possible to be computed. On the other hand the polynomial method slopes are close to the power law fit differentiation and both present the smaller dispersions. In view of the good correlation and small dispersion in the crack propagation curve, the da/dN obtained by the power law fit is presented in the remainder of the paper.

The fracture energy release rate G is computed by two different methods, each method is based on the compliance or strain energy versus the video processed delamination length a signal curves slopes (see figure A.9 and A.10). The polynomial method fittings of the compliance versus the monitored crack length are shown in figure A.9 with an average R correlation coefficient value of 0.96. Figure A.10 represents the strain energy and the power law fitting models as function of the crack length, a good correlation

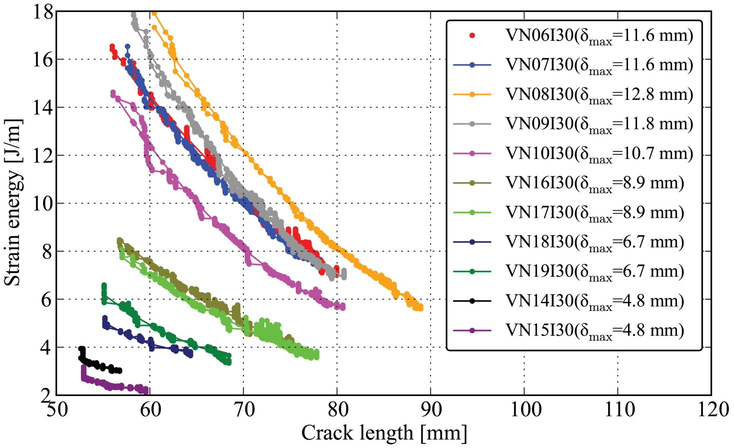

Figure A.10: Strain energy versus crack length. Experimental and fit curves.

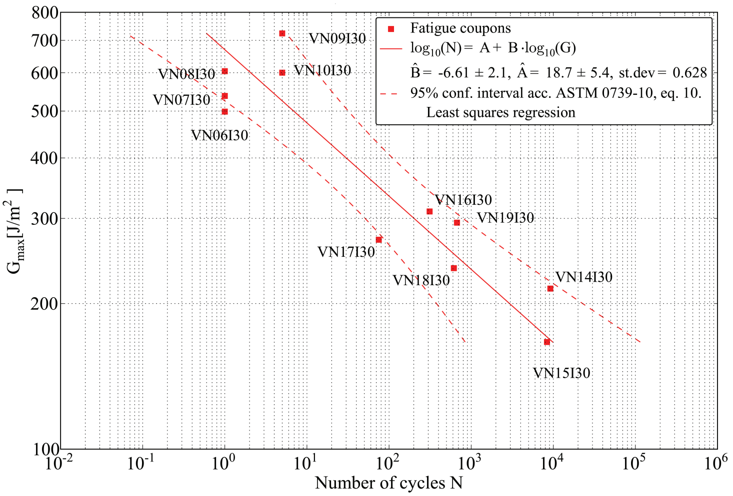

Figure A.11: Delamination growth onset G_{max} vs. cycles log/log curve (ASTM D6115).

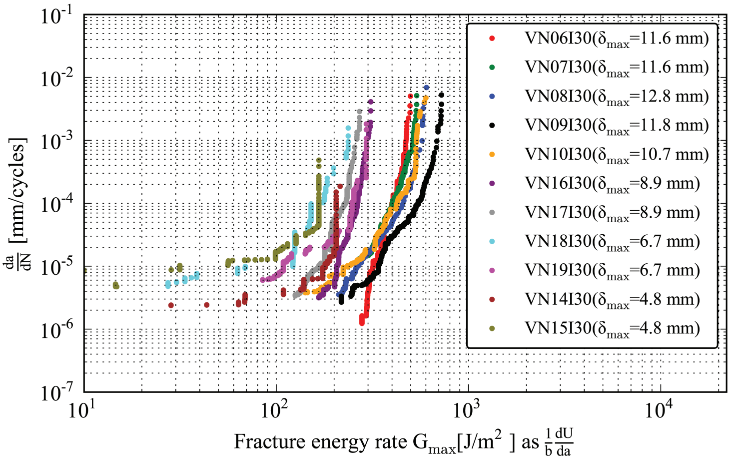

Figure A.12: Crack propagation curves. Crack growth rate vs. max fracture energy rate.

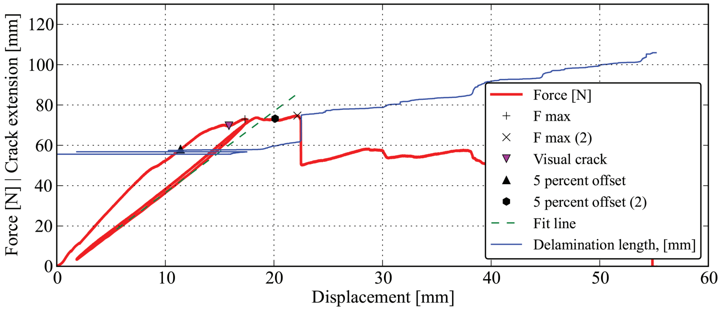

Figure A.13: Force and crack extension vs. displacement curve. Coupon VN01I30 static test (3 mm/min).

between both is shown with an average R correlation coefficient of 0.97. Since the strain energy represents the cyclically imposed work, the strain energy dependence on the loading ratios is observed. The average R correlation coefficient between the two methods to calculate energy release rate G is 0.91, showing similar fracture energy release rates values.

As shown in figure A.11, the $G_{max} - N$ delamination growth onset curve is characterised by a slope of 6.61 with a 95% confidence interval of 2.1. The $G_{max} - N$ curve shows a very early start of the delamination in fatigue for fracture energies close to the static tests results. As the videos were taken at cyclic intervals, the resolution of the curve is determined by the interval length. Taken into account that $G_{max} - N$ curve and the crack length in figure A.7 shows a power law trend, an incremental approach in order to perform the video monitoring and reduce the data storage seems to be the best approach.

Figure A.12 shows the crack growth rate as a function of the maximum fracture energy rate for the different loading ratios tested in fatigue. While low displacement ratio coupons show two differentiated regions with a extended linear region up to 100 J/m^2, for the rest of the coupons only the fast growth region is visible. The different coupons present similar trends, higher crack growth rates occurs for the highest fracture energy rates in the range of 100 to 1000 J/m^2. In between, the fracture energy rate shift from lower to higher fracture energy rates can be observed as the loading ratios increase.

VIDEO IMAGE PROCESSING TECHNIQUE

For the standard 3mm/min static tests speed a frame rate of 7fps allows a movement resolution of 0.0071 mm of displacement per frame. Synchronisation of the load, displacement, and crack length signals can be achieved by correlating distinct jumps, as Figure A.13 shows.

In the case of the fatigue test, a 1.5Hz frequency test with 10mm amplitudes is equivalent to a test speed of 30mm/sec, which is a very high speed in view of a direct synchronization between the measured crack length and force. However, because each video is representative of around 10-30 cycles the highest delamination length measured in that range was chosen assuming no crack length in that relative small interval of time in comparison with the 2-3 weeks extension of a one million cycles fatigue test.

The accuracy of the system has been established with dummy shapes previously measured with a calliper at different extreme positions and camera setups. It shows that it can achieve accuracies around ±0.5mm in the static test, which is the minimum required by the ASTM D5528 standard. Additionally the final crack extension in the fatigue tests was compared against calliper measurements showing relatives differences below 8% at the end of the fatigue tests.

CONCLUSIONS

A visual technique based on video image processing for measuring the delamination length in mode I static and fatigue tests has been described and applied in glass fibre reinforced composites. The crack length measurements show a reliable signal with no need to stop the tests, high sampling rate and synchronization with the force and displacement signals. Accuracies up to ±0.5mm were measured for calibrated coupons and relative differences lower than 8% where observed in comparison with calliper measurements.

Crack length signals were measured every 100-500 cycles in mode I fatigue tests. A power law trend was observed in the crack length signal evolution with the cycles for the studied GFRP. Three different methods to compute the crack growth rate were evaluated with similar results, of which the power law method shows the smallest dispersion. The fracture energy rates were computed by two different methods with similar results.

B

APPENDIX B. IR INSPECTION OF THICK LAMINATES DURING FATIGUE

The thermoelastic stress analysis (TSA) technique is a lock-in thermography technique of the PPT type, where the stimulus is the thermo-elastic behaviour of the material when it is dynamically loaded [171]. Generally, in TSA the final purpose is to obtain the full field principal stress gradient, which requires a calibration and synchronized load or strain signal [77].

Tests carried out in chapter 2 and 3 were studied with TSA. The phase and amplitude thermographs during the fatigue tests were computed with an in-house algorithm based on FFT. First, the IR inspection was carried out for a well known open-hole fatigue test (see figure B.1). The results of the open-hole tests revealed that FFT thermographs show higher intensity values where the major damage is located and such thermographs agree with final failure photographs.

The same technology was applied to scaled compression tests from chapter 3. The FFT thermographs recorded during fatigue tests showed damage development close to the end of the grip were the higher stresses are located due to the clamping force. This was previously referred as the grip effect, which is the most common cause of failure during mechanical tests. Figure B.2 and B.3 show higher intensities in the FFT thermographs close to the end of the grip that agrees with the final failures observed in the fatigue tests.

This chapter is extracted from [170].

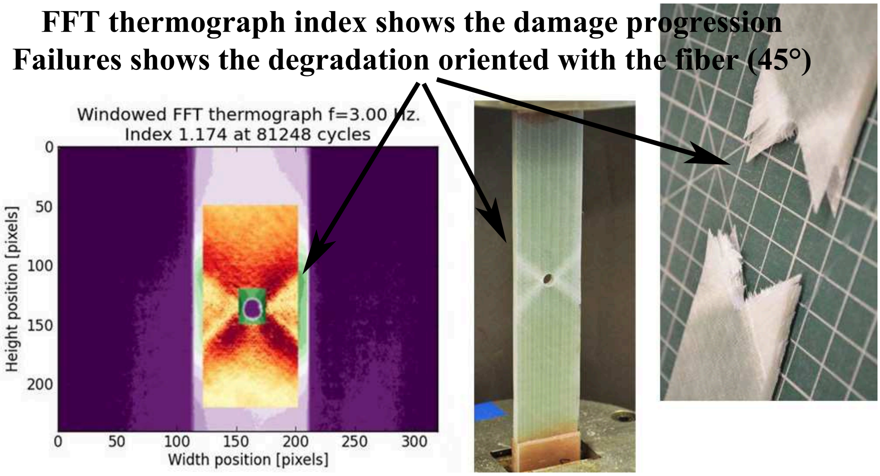
FFT thermograph index shows the damage progression
Failures shows the degradation oriented with the fiber (45°)

Figure B.1: Open hole fatigue tests recorded with IR camera. Thermographs and FFT thermographs were damage is located. Photos of the coupons during the fatigue tests as well final failure photo.

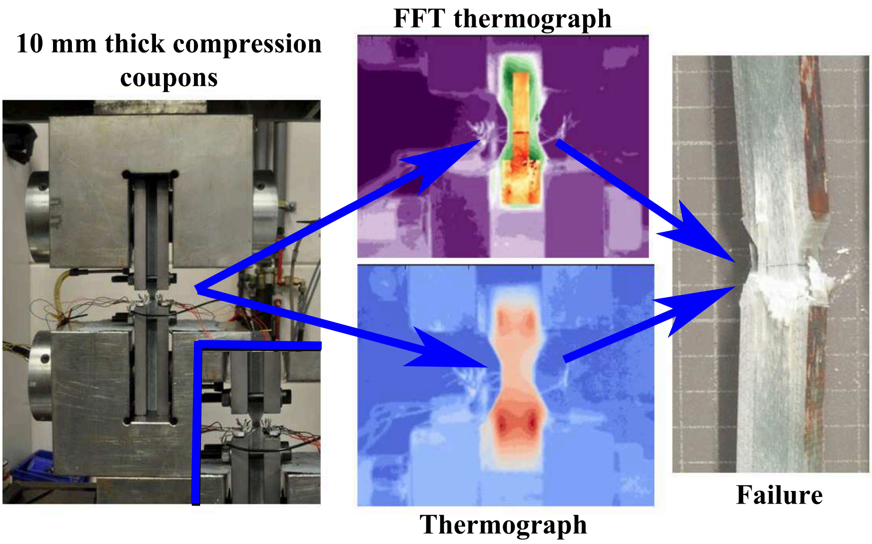

Figure B.2: 10 mm compression tests recorded with IR camera. Thermographs and FFT thermographs were damage is located. Photos of the coupons during the fatigue tests as well final failure photo. Large intensity areas shows the main locations of the stress fields peaks cause by the grip effect.

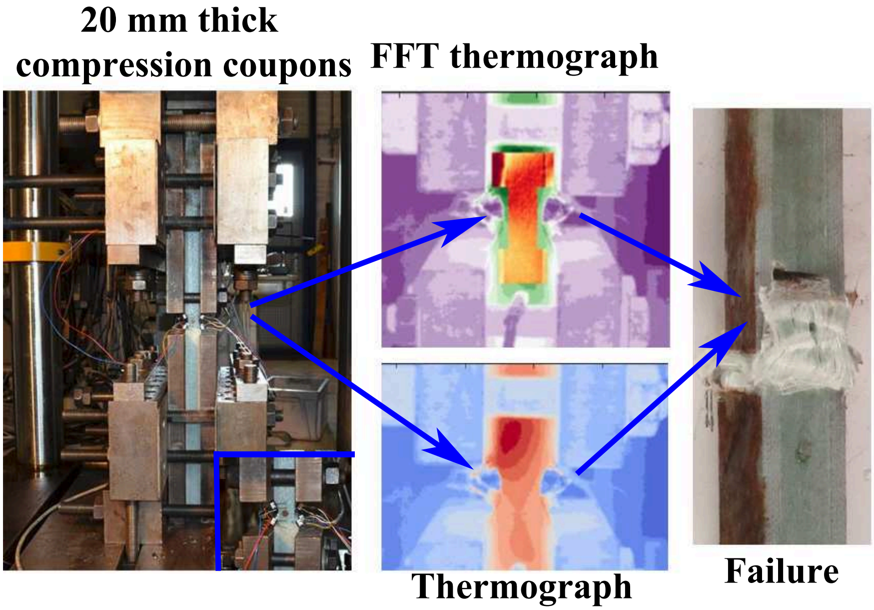

Figure B.3: 20 mm compression tests recorded with IR camera. Thermographs and FFT thermographs were damage is located. Photos of the coupons during the fatigue tests as well final failure photo. Large intensity areas shows the main locations of the stress fields peaks cause by the grip effect.

C

APPENDIX C

case	group	e	h	h_0	k	m	n	g	w	l	α	layout tab
		[mm]	[mm]	[mm]	[mm]	[mm]	[mm]	[mm]	[mm]	[mm]	°	
0	base	2.8	7.0	7.0	50.0	96.360	27.28	15.0	10.0	320.0	18.9	UD_1, UD_2, UD_3
1	g / m	2.8	7.0	7.0	50.0	96.360	27.28	**15.0**	10.0	320.0	18.9	UD_1, UD_2, UD_3
2	g / m	2.8	7.0	7.0	50.0	88.860	42.28	**30.0**	10.0	320.0	18.9	UD_1, UD_2, UD_3
3	g / m	2.8	7.0	7.0	50.0	73.860	72.28	**60.0**	10.0	320.0	18.9	UD_1, UD_2, UD_3
4	g / m	2.8	7.0	7.0	50.0	43.860	132.28	**120.0**	10.0	320.0	18.9	UD_1, UD_2, UD_3
5	g / m	2.8	7.0	7.0	50.0	23.860	172.28	**160.0**	10.0	320.0	18.9	UD_1, UD_2, UD_3
6	g / m	2.8	7.0	7.0	50.0	13.860	192.28	**180.0**	10.0	320.0	18.9	UD_1, UD_2, UD_3
7	alpha	2.8	7.0	7.0	50.0	78.497	63.01	15.0	10.0	320.0	**5.0**	UD_1, UD_2, UD_3
8	alpha	2.8	7.0	7.0	50.0	90.590	38.82	15.0	10.0	320.0	**10.0**	UD_1, UD_2, UD_3
9	alpha	2.8	7.0	7.0	50.0	97.997	24.01	15.0	10.0	320.0	**25.0**	UD_1, UD_2, UD_3
10	alpha	2.8	7.0	7.0	50.0	98.863	22.27	15.0	10.0	320.0	**30.0**	UD_1, UD_2, UD_3
11	h	2.8	**5.8**	5.8	50.0	98.114	23.77	15.0	10.0	320.0	18.9	UD_1, UD_2
12	h	2.8	**8.8**	8.8	50.0	93.729	32.54	15.0	10.0	320.0	18.9	UD_1, UD_2, UD_3
13	h	2.8	**11.8**	11.8	50.0	89.343	41.31	15.0	10.0	320.0	18.9	UD_1 to UD_5
14	h	2.8	**14.8**	14.8	50.0	84.957	50.09	15.0	10.0	320.0	18.9	UD_1 to UD_7

Table C.1: FE tension parametric analysis. Cases table.

D

APPENDIX D. RELATION BETWEEN HEATING RATE AND CURE RATE.

The curing cycle of thermoset thick laminates can be modelled using the general heat equation [172, 173]. Assuming that the temperature differences between resin and fibers are negligible at any time and neglecting the convective effect of the resin flow, the governing equation can be expressed as follows,

$$\begin{aligned}\rho \cdot c_P \cdot \frac{\partial T}{\partial t} = \frac{\partial}{\partial x}\left(K_x \cdot \frac{\partial T}{\partial x}\right) \\ + \frac{\partial}{\partial y}\left(K_y \cdot \frac{\partial T}{\partial y}\right) \\ + \frac{\partial}{\partial z}\left(K_z \cdot \frac{\partial T}{\partial z}\right) + \dot{q} \end{aligned} \tag{D.1}$$

where ρ is the laminate density, c_P is the specific heat, $K_i\,(i = x, y, z)$ is the thermal conductivity, $T = T(x, y, z, t)$ is the temperature field, t is the time and $\dot{q}$ is the internal heat generation component per unit volume or also called rate of heat generation.

The internal heat generation component $\dot{q}$ can be modelled as follows,

$$\dot{q} = \rho \cdot H_r \cdot R_\alpha = \rho \cdot H_r \cdot \frac{d\alpha}{dt} \tag{D.2}$$

where H_r is the total heat of the reaction, $R_\alpha = \frac{d\alpha}{dt}$ is the rate of reaction (also called cure rate or conversion rate) and α is the degree of cure or conversion factor which defines the curing reaction kinetic.

Assuming one dimensional conditions and a thermal conductivity K_z that is independent of the location, equation D can be simplified as follows,

---

This appendix was integrally extracted from appendix B from [130].

$$\rho \cdot c_P \cdot R_t = K_z \cdot \frac{\partial}{\partial z}\left(\frac{\partial T}{\partial z}\right) + \rho \cdot H_r \cdot R_\alpha \tag{D.3}$$

where $R_t = \frac{dT}{dt}$ is the heating rate. Equation D.3 shows that the heating rate is proportionally related to reaction cure rate and the diffusion component. Before and after the curing reaction $\alpha = 0$ and $\alpha = 1$, the heating rate R_t is dominated by the diffusion component. During the curing reaction $0 < \alpha < 1$ the internal heat component becomes active. And in the case of small thermal conductivities K_i, the diffusion component can be neglected. In such case the internal heat component can be approximated to the transient part as follows,

$$R_t \simeq \frac{H_r}{c_P} \cdot R_\alpha \tag{D.4}$$

where the heating rate and the curing rate during curing reaction are proportional and follows a close behaviour.

Measuring the curing rate with three thermocouples

If equation D.3 is discretized using finite-differences [118] it can be written as follows,

$$\rho \cdot c_P \cdot R_t = K_z \cdot \frac{T^p_{k+1} + T^p_{k-1} - 2 \cdot T^p_k}{\Delta z^2} + \rho \cdot H_r \cdot R_\alpha \tag{D.5}$$

$$R_t = \frac{T^{p+1}_k - T^p_k}{\Delta t} \tag{D.6}$$

where k relates to the discrete thickness location of nodal points and p denotes the discrete time dependence of the temperature field as $t = p \cdot \Delta t$.

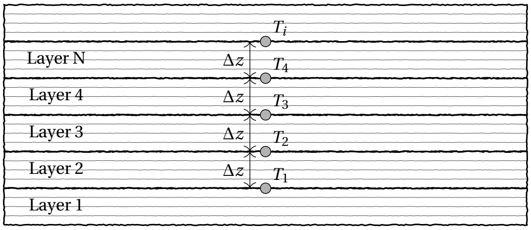

Figure D.1: Embedded thermocouples array through the thickness to measure the local temperatures.

In the case of the sub-laminate tests, a serie of thermocouples were embedded along the laminate thickness to measure the local temperatures (see figure D.1 and table 5.1). Those temperature measurements can be seen as discrete temperature measurement points noted as $T_i\,(i = 1, \ldots, N)$ where N is the number of temperature measurements through the thickness. Therefore, equation D.5 can be written as follows,

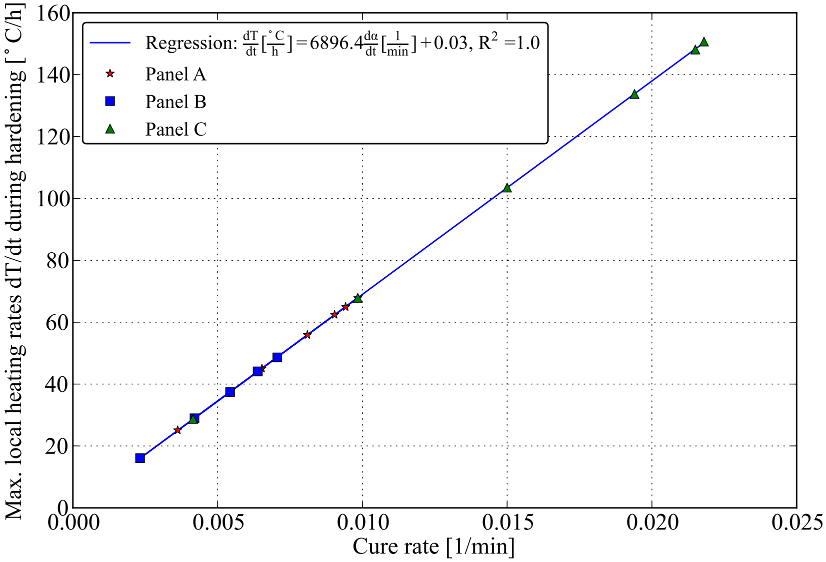

Figure D.2: Correlation between the heating rate and the curing rate according equation D.7 ($c_p = 1.044\,[J/g^\circ C]$, $H_r = 120\,[J/g]$, $K_z = 0.512\,[W/m^\circ C]$ and $\rho = 1.86\,[g/cm^3]$). Plates A, B and C.

$$R_{\alpha,p} = \frac{c_P}{H_r} \cdot \frac{T_i^{p+1} - T_i^p}{\Delta t} - \frac{K_z}{\rho \cdot H_r} \cdot \frac{T_{i+1}^p + T_{i-1}^p - 2 \cdot T_i^p}{\Delta z^2} \tag{D.7}$$

where the curing rate R_α can be computed from an array of three thermocouples assuming 1D conditions and neglecting the corresponding error from the finite-differences discretization.

Based on the sub-laminates temperature measurements and equation D.7, the curing rate was computed at the maximum heating rate during hardening. The c_P, H_r, K_z and ρ were obtained from the bibliography [110] for the tested material. The relation between curing rate and heating rate is shown in figure D.2. This figure shows the correlation between both rates with a Pearson coefficient around 1. The thermal diffusion component values are below 1% of the transient component values. Therefore, the approximation of equation D.4 is valid for the investigated system around the time of max. heating rate. This indicates that the heating rate during the hardening phase is almost proportional to the curing rate, and that just one thermocouple is sufficient to measure the curing rate.

BIBLIOGRAPHY

[1] TPI Composites, “Cost study for large wind turbine blades : windpact blade system design studies sand2003-1428”, Sandia National Laboratories, Warren, Tech. Rep. May, 2003.

[2] RPL Nijssen, T Westphal, F Lahuerta, and DRV van Delft, “Recent results in characterisation and modeling of composites for wind turbine blades”, in *Composites week @ LEUVEN and TEXCOMP-11 Conference*, Leuven, 2013.

[3] *Dnv-gl guideline for the certification of wind turbines*, Germany 2010.

[4] *Dnv-os-c501 composite components*, 2003.

[5] *Nen-en-iec 61400-23, wind turbines - part 23: full-scale structural testing of rotor blades*, 2014.

[6] *Iec 61400-1, wind turbines part 1: design requirements*, 2004.

[7] IM Daniel, HM Hsiao, and SC Wooh, “Failure mechanisms in thick composites under compressive loading”, *Composites Part B: Engineering*, vol. 27B, pp. 543–552, 1996. DOI: `10.1016/1359-8368(95)00010-0`.

[8] K Zimmermann, D Zenkert, and M Siemetzki, “Testing and analysis of ultra thick composites”, *Composites Part B: Engineering*, vol. 41, no. 4, pp. 326–336, 2010, ISSN: 13598368. DOI: `10.1016/j.compositesb.2009.12.004`.

[9] E Stammes, RPL Nijssen, and T Westphal, “Effect of laminate thickness tests on thick laminates wmc-2009-38”, Knowledge centre WMC, Knowledge centre WMC, Wieringerwerf NL, Tech. Rep. May, 2010, p. 89.

[10] A van Wingerde, “Evaluation on the effect of thick laminates wp10”, Knowledge centre WMC, Wieringerwerf NL, Tech. Rep., 2006.

[11] A van Wingerde, RPL Nijssen, and DRV van Delft, “Fe analysis of thick test specimens”, Knowledge centre WMC, Wieringerwerf NL, Tech. Rep., 2005.

[12] F Lahuerta, T Westphal, RPL Nijssen, FP van der Meer, and LJ Sluys, “Measuring the delamination length in static and fatigue mode i tests using video image processing”, *Composites Part B: Engineering*, vol. 63, pp. 1–7, 2014, ISSN: 13598368. DOI: `10.1016/j.compositesb.2014.03.003`.

[13] F Lahuerta and RPL Nijssen, “Static enf test configuration, with different reinforcement roving configuration. wmc-2013-004c”, WMC Knowledge Centre, Wieringerwerf, NL, Tech. Rep., 2013.

[14] *Upwind optidat database. wmc knowledge centre.* [Online]. Available: `http://www.wmc.eu/optimatblades/optidat.php`.

[15] JR Lund and JP Byrne, “Leonardo da vinci’s tensile strength tests: implication for the discovery”, *Civil Engineering and Enviromental Systems*, vol. 18, no. 3, pp. 243–250, 2001. DOI: `10.1080/02630250108970302`.

[16] ZP Bažant, “Size effect on structural strength : a review”, *Archive of applied mechanics*, vol. 69, no. 9-10, pp. 703–725, 1999. DOI: `10.1007/s004190050252`.

[17] C Zweben, “Is there a size effect in composites?”, *Composites*, vol. 25, no. 6, pp. 451–454, Jul. 1994. DOI: `10.1016/0010-4361(94)90102-3`.

[18] GJ Simitses, “Design of scaled down structural models”, in *Workshop on scaling effects in composite materials and structures NASA-CP-3271*, 1994.

[19] LS Sutherland, RA Shenoi, and SM Lewis, “Size and scale effects in composites: i. literature review”, *Composites Science and Technology*, vol. 59, no. 2, pp. 209–220, 1999. DOI: `10.1016/S0266-3538(98)00065-7`.

[20] KE Jackson and S Kellas, “Sub-ply level scaling approach investigated for graphite epoxy composite beam colums”, in *Workshop on scaling effects in composite materials and structures NASA-CP-3271*, 1994.

[21] KE Jackson, S Kellas, and J Morton, “Scale effects in the response and failure of fiber reinforced composite laminates loaded in tension and in flexure”, *Journal of Composite Materials*, vol. 26, no. 18, pp. 2674–2705, 1992, ISSN: 0021-9983. DOI: `10.1177/002199839202601803`.

[22] GC Grimes, “Experimental observations of scale effects on bonded and bolted joints in composite structures”, in *Workshop on scaling effects in composite materials and structures NASA-CP-3271*, 1994.

[23] G Camponeschi, “The effects of specimen scale on the compression strength of composite materials”, in *Workshop on scaling effects in composite materials and structures NASA-CP-3271*, Langley research center, Hampton (Virginia), 1994.

[24] HW Blake and JM Starbuck, “Hydrostatic pressure testing of graphite/epoxy cyclinder c6-1”, Martin marietta energy systems, INC, Tech. Rep., 1992.

[25] Q Bing and CT Sun, “Specimen size effect in off-axis compression tests of fiber composites”, *Composites Part B: Engineering*, vol. 39, no. 1, pp. 20–26, Jan. 2008. DOI: `10.1016/j.compositesb.2007.02.010`.

[26] DJ Wilkins, “On nature’s scaling effects”, in *Workshop on scaling effects in composite materials and structures NASA-CP-3271*, Langley research center, Hampton (Virginia), 1994.

[27] ASD Wang, “Scaling effects of defects in fiber reinforced composites”, in *Workshop on scaling effects in composite materials and structures NASA-CP-3271*, Langley research center, Hampton (Virginia), 1994.

[28] J Phillips, A Shenoi, and M Lewis, “Effect of specimen size on the strength scaling of gfrp laminates”, *Materials Letters*, vol. 21, no. November, pp. 229–238, 1994. DOI: `10.1016/0167-577x(94)90181-3`.

[29] MR Wisnom, “Relationship between strength variability and size effect in unidirectional carbon fibre / epoxy”, *Composites*, vol. 22, no. 1, pp. 47–52, 1991. DOI: `10.1016/0010-4361(91)90102-M`.

[30] R Byron and MR Gurvich, “Strength size effect of laminated composites”, *Composites Science and Technology*, vol. 55, pp. 93–105, 1995. DOI: `10.1016/0266-3538(95)00092-5`.

[31] MR Wisnom and JW Atkinson, “Reduction in tensile and flexural strength of unidirectional glass fibre-epoxy with increasing specimen size”, *Composite Structures*, vol. 38, no. 1, pp. 405–411, 1997. DOI: `10.1016/S0263-8223(97)00075-5`.

[32] MR Wisnom, “Size effects in the testing of fibre-composite materials. review”, *Composites Science and Technology*, vol. 59, no. 13, pp. 1937–1957, Oct. 1999, ISSN: 02663538. DOI: `10.1016/S0266-3538(99)00053-6`.

[33] LS Sutherland, RA Shenoi, and SM Lewis, “Size and scale effects in composites: ii. unidirectional laminates”, *Composites Science and Technology*, vol. 59, no. 2, pp. 221–233, 1999. DOI: `10.1016/S0266-3538(98)00083-9`.

[34] LS Sutherland, RA Shenoi, and SM Lewis, “Size and scale effects in composites: iii. woven-roving laminates”, *Composites Science and Technology*, vol. 59, no. 2, pp. 235–251, 1999. DOI: `10.1016/S0266-3538(98)00106-7`.

[35] P Davies and D Petton, “An experimental study of scale effects in marine composites”, *Composites Part A: Applied Science and Manufacturing*, vol. 30, pp. 267–275, 1999. DOI: `10.1016/S1359-835X(98)00156-0`.

[36] JA Lavoie, C Soutis, and J Morton, “Apparent strength scaling in continuous fiber composite laminates”, *Composites Science and Technology*, vol. 60, no. 2, pp. 238–299, 2000. DOI: `10.1016/S0266-3538(99)00124-4`.

[37] MR Wisnom, SR Hallett, and C Soutis, “Scaling effects in notched composites”, *Journal of Composite Materials*, vol. 44, no. 2, pp. 195–210, 2009. DOI: `10.1177/0021998309339865`.

[38] J Lee and C Soutis, “Measuring the notched compressive strength of composite laminates: specimen size effects”, *Composites Science and Technology*, vol. 68, no. 12, pp. 2359–2366, 2008. DOI: `10.1016/j.compscitech.2007.09.003`.

[39] W Weibull, “A statistical theory of the strength of materials”, PhD thesis, Royal Technical University Stockholm, 1939.

[40] FT Peirce, “Tensile tests for cotton yarns v, ’the weakest link’ theorems on strength of lon and composite specimens”, *Journal of Textile Institute*, vol. 17, T335–T368, 1926.

[41] A Tabiei and J Sun, “Statistical aspects of strength size effect of laminated composite materials”, *Composites Structures*, vol. 46, pp. 209–216, 1999. DOI: `10.1016/S0263-8223(99)00056-2`.

[42] FW Crossman and ASD Wang, “The dependence of transverse cracking and delamination on ply thickness in graphite/epoxy laminates”, in *Damage in composite materials ASTM STP 775*, 1982, pp. 118–139.

[43] PM Scop and AS Argon, “Statistical theory of strength of laminated composites”, *Journal of Composite Materials*, vol. 1, pp. 92–99, 1967. DOI: `10.1177/002199836700100109`.

[44] PM Scop and aS Argon, “Statistical theory of strength of laminated composites ii”, *Journal of Composite Materials*, vol. 3, no. 1, pp. 30–47, 1969. DOI: `10.1177/002199836900300103`.

[45] C Zweben and BW Rosen, “A statistical theory of material strength with application to composite materials”, *Journal of the Mechanics and Physics of Solids*, vol. 18, no. 3, pp. 189–206, 1970. DOI: `10.1016/0022-5096(70)90023-2`.

[46] Y Zhu, B Zhou, G He, and Z Zheng, “A statistical theory of composite materials strength”, *Journal of Composite Materials*, vol. 23, no. 3, pp. 280–287, 1989. DOI: `10.1177/002199838902300305`.

[47] J Degrieck and WV Paepegem, “Fatigue damage modelling of fibre-reinforced composite materials : review”, *Applied Mechanics Reviews*, vol. 54, no. 4, pp. 279–300, 2001. DOI: `10.1115/1.1381395`.

[48] Stammes E, RPL Nijssen, S Raijmaekers, and T Westphal, “Influence of laminate thickness in fatigue testing of wind turbine composites”, in *SAMPE Seico*, Paris, 2010.

[49] Jt Fong, “What is fatigue damage ?”, *Damage in Composite Materials ASTM STP775*, pp. 243–266, 1982.

[50] T Nyman, “Composite fatigue design methodology: a simplified approach”, *Composite Structures*, vol. 35, pp. 183–194, 1996. DOI: `doi:10.1016/0263-8223(96)00032-3`.

[51] D Revuelta, J Cuartero, A Miravete, and R Clemente, “A new approach to fatigue analysis in composites based on residual strength degradation”, *Composite Structures*, vol. 48, no. 1-3, pp. 183–186, 2000. DOI: `10.1016/S0263-8223(99)00093-8`.

[52] K Cox and A Echtermeyer, “Effects of composite fiber orientation on wind turbine blade buckling resistance”, *Wind Energy*, vol. 17, pp. 1925–1943, 2014. DOI: `10.1002/we.1681`.

[53] HJ Sutherland and JF Mandell, “The effect of mean stress on damage predictions for spectral loading of fibreglass composite coupons”, *Wind Energy*, vol. 8, no. August 2004, pp. 93–108, 2005. DOI: `10.1002/we.125`.

[54] L Mishnaevsky, P Brøndsted, RPL Nijssen, DJ Lekou, and TP Philippidis, “Materials of large wind turbine blades: recent results in testing and modeling”, *Wind Energy*, vol. 15, pp. 83–97, 2012. DOI: `10.1002/we.470`.

[55] HJ Sutherland, “A summary of the fatigue properties of wind turbine materials”, *Wind Energy*, vol. 3, pp. 1–34, 2000. DOI: `10.1002/1099-1824(200001/03)3:1<1::AID-WE28>3.0.CO;2-2`.

[56] JC Marín, A Barroso, F París, and J Cañas, “Study of fatigue damage in wind turbine blades”, *Engineering Failure Analysis*, vol. 16, no. 2, pp. 656–668, 2009. DOI: `10.1016/j.engfailanal.2008.02.005`.

[57] NP Inglis, “Hysteresis and fatigue of wohler rotatng cantilever specimen”, *The Metallurgist*, pp. 23–27, 1927.

[58] A Kimball and D Lovell, “Internal friction in solids”, *Physical Review*, vol. 30, no. 6, pp. 948–959, 1927. DOI: `10.1103/PhysRev.30.948`.

[59] HF Moore and JB Koomers, “Fatigue of metals under repeated stress”, *Trans. Amer. Soc.*, vol. 25, pp. 1141–1144, 1921.

[60] AE Green and PM Naghdi, “A general theory of an elastic-plastic continuum”, *Archive for Rational Mechanics and Analysis*, vol. 18, no. 4, 1965. DOI: `10.1007/BF00251666`.

[61] Z Mróz and B Raniecki, “On the uniqueness problem in coupled thermoplasticity”, *International Journal of Engineering Science*, vol. 14, no. 2, pp. 211–221, 1976. DOI: `10.1016/0020-7225(76)90090-2`.

[62] Z Mróz and B Raniecki, “A derivation of the uniqueness conditions in coupled thermoplasticity”, *International Journal of Engineering Science*, vol. 14, no. 4, pp. 395–401, 1976. DOI: `10.1016/0020-7225(76)90012-4`.

[63] DW Nicholson, “A note on uniqueness in coupled thermoplasticity”, *Acta Mechanica*, vol. 78, no. 1-2, pp. 161–168, 1989. DOI: `10.1007/BF01174007`.

[64] SB Ratner, VI Korobov, and SG Agamalyan, “Mechanical and thermal fracture of plastics under cyclic strains”, *Soviet Materials Science*, vol. 5, no. 1, pp. 66–70, 1972. DOI: `10.1007/BF00721313`.

[65] SB Ratner and VI Korobov, “Spontaneous heating in a polymer during repeated deformation”, *Soviet Physics Doklady*, vol. 10, p. 361, 1965.

[66] SB Ratner and VI Korobov, “Self-heating of plastics during cyclic deformation”, *Polymer Mechanics*, vol. 1, no. 3, pp. 63–68, 1966, ISSN: 0032-390X. DOI: `10.1007/BF00858807`.

[67] AV Stinskas, NI Antropova, VI Korobov, SB Ratner, AV Samokhvalov, and AV Sharova, “Fatigue properties of kapron (nylon-6) and kaprolon”, *Polymer Mechanics*, vol. 1, no. 2, pp. 90–92, 1966. DOI: `10.1007/BF00860690`.

[68] KL Reifsnider and RS Williams, “Determination of fatigue-related heat emission in composite materials during fatigue loading”, *Experimental Mechanics*, vol. 14, no. 12, pp. 479–485, Dec. 1974, ISSN: 0014-4851. DOI: `10.1007/BF02323148`.

[69] WW Stinchcomb, KL Reifsnider, LA Marcus, and RS Williams, “Effects of frequency on the mechanical response of two composite materials to fatigue loads”, in *Fatigue of composite materials ASTM STP 569*, 1975.

[70] AK K Wong and GC C Kirby, “A hybrid numerical/experimental technique for determining the heat dissipated during low cycle fatigue”, *Engineering Fracture Mechanics*, vol. 37, no. 3, pp. 493–504, 1990. DOI: `10.1016/0013-7944(90)90375-Q`.

[71] J Lemaître and R Desmorat, *Engineering Damage Mechanics*. Berlin/Heidelberg: Springer-Verlag, 2005. DOI: `10.1007/b138882`.

[72] JM M Kenny and M Marchetti, "Elasto plastic behavior of thermoplastic composite laminates under cyclic loading", *Composites Structures*, vol. 32, no. 1-4, pp. 375–382, Jan. 1995, ISSN: 02638223. DOI: `10.1016/0263-8223(95)00052-6`.

[73] TK Jacobsen, BF Sørensen, and P Brøndsted, "Measurement of uniform and localized heat dissipation induced by cyclic loading", *Experimental Mechanics*, vol. 38, no. 4, pp. 289–294, 1998. DOI: `10.1007/BF02410391`.

[74] O Redon, "Fatigue damage development and failure in unidirectional and angle-ply glass fibre / carbon fibre hybrid laminates", PhD thesis, Riso-R-1168, 2000, ISBN: 8755026702.

[75] EK Gamstedt, O Redon, and P Brøndsted, "Fatigue dissipation and failure in unidirectional and angle-ply glass fibre/carbon fibre hybrid laminates", *Key Engineering Materials*, vol. 221-222, pp. 35–48, 2001. DOI: `10.4028/www.scientific.net/KEM.221-222.35`.

[76] MP Luong, "Fatigue limit evaluation of metals using an infrared thermographic technique", *Mechanics of Materials*, vol. 28, no. 1-4, pp. 155–163, 1998. DOI: `10.1016/S0167-6636(97)00047-1`.

[77] FA Diaz, EA Patterson, and JR Yates, "Fatigue damage assessment using thermoelastic stress analysis", in *ECF15*, 2004, pp. 1–8.

[78] F Maquin and F Pierron, "Refined experimental methodology for assessing the heat dissipated in cyclically loaded materials at low stress levels", *Comptes Rendus Mécanique*, vol. 335, no. 3, pp. 168–174, 2007. DOI: `10.1016/j.crme.2007.02.004`.

[79] X Wang, V Crupi, Y Zhao, and X Guo, "Lock-in thermographic methodology for fatigue assessment and nonlinear stress measurement", *Proceedings of SPIE*, vol. 7375, 73752P–73752P–6, 2008. DOI: `10.1117/12.839226`.

[80] F Maquin and F Pierron, "Heat dissipation measurements in low stress cyclic loading of metallic materials: from internal friction to micro-plasticity", *Mechanics of Materials*, vol. 41, no. 8, pp. 928–942, 2009. DOI: `10.1016/j.mechmat.2009.03.003`.

[81] AL L Audenino, V Crupi, and EM M Zanetti, "Correlation between thermography and internal damping in metals", *International Journal of Fatigue*, vol. 25, no. 4, pp. 343–351, Apr. 2003, ISSN: 01421123. DOI: `10.1016/S0142-1123(02)00137-8`.

[82] SM Johnson, HK Kim, RF El, and RM Haj, "An ir technique for damage characterisation in thick section composites", in *Conference: 2004 SEM X International Congress & Exposition on Experimental & Applied Mechanics*, 2004.

[83] A Mian, X Han, S Islam, and G Newaz, "Fatigue damage detection in graphite/epoxy composites using sonic infrared imaging technique", *Composites Science and Technology*, vol. 64, no. 5, pp. 657–666, 2004. DOI: `10.1016/j.compscitech.2003.07.005`.

[84] S Johnson, Hk Kim, Bs Wei, and R Haj-ali, “Infrared thermography for damage and fatigue of thick- section frp composites”, in *9th International Fatigue Congress*, Atlanta, Georgia, 2004.

[85] L Toubal, M Karama, and B Lorrain, “Damage evolution and infrared thermography in woven composite laminates under fatigue loading”, *International Journal of Fatigue*, vol. 28, no. 12, pp. 1867–1872, 2006. DOI: `10.1016/j.ijfatigue.2006.01.013`.

[86] M Naderi, M Amiri, and MM Khonsari, “On the thermodynamic entropy of fatigue fracture”, *Proceedings of the Royal Society A: Mathematical, Physical and Engineering Sciences*, vol. 466, no. 2114, pp. 423–438, 2009. DOI: `10.1098/rspa.2009.0348`.

[87] M Eleuteri, J Kopfová, and P Krejčí, “A thermodynamic model for material fatigue under cyclic loading”, *Physica B: Condensed Matter*, vol. 407, no. 9, pp. 1415–1416, 2012. DOI: `10.1016/j.physb.2011.10.017`.

[88] Mh Maitournam, “Comptes rendus mecanique entropy and temperature gradients thermomechanics : dissipation , heat conduction inequality and heat equation”, *Comptes Rendus Mecanique*, vol. 340, no. 6, pp. 434–443, 2012. DOI: `10.1016/j.crme.2012.04.001`.

[89] M Naderi and MM Khonsari, “An experimental approach to low-cycle fatigue damage based on thermodynamic entropy”, *International Journal of Solids and Structures*, vol. 47, no. 6, pp. 875–880, 2010. DOI: `10.1016/j.ijsolstr.2009.12.005`.

[90] M Naderi and M Khonsari, “Real-time fatigue life monitoring based on thermodynamic entropy”, *Structural Health Monitoring*, vol. 10, no. 2, pp. 189–197, 2010. DOI: `10.1177/1475921710373295`.

[91] M Naderi and MM Khonsari, “A thermodynamic approach to fatigue damage accumulation under variable loading”, *Materials Science and Engineering: A*, vol. 527, no. 23, pp. 6133–6139, 2010. DOI: `10.1016/j.msea.2010.05.018`.

[92] M Naderi and MM Khonsari, “Thermodynamic analysis of fatigue failure in a composite laminate”, *Mechanics of Materials*, vol. 46, pp. 113–122, 2012. DOI: `10.1016/j.mechmat.2011.12.003`.

[93] M Naderi and MM Khonsari, “A comprehensive fatigue failure criterion based on thermodynamic approach”, *Journal of Composite Materials*, vol. 46, no. 4, pp. 437–447, 2011. DOI: `10.1177/0021998311419540`.

[94] M Naderi, A Kahirdeh, and MM M Khonsari, “Dissipated thermal energy and damage evolution of glass/epoxy using infrared thermography and acoustic emission”, *Composites Part B: Engineering*, vol. 43, no. 3, pp. 1613–1620, 2012. DOI: `10.1016/j.compositesb.2011.08.002`.

[95] Sy Lee and GS Springer, “Effects of cure on the mechanical properties of composites”, *Journal of Composite Materials*, vol. 22, no. 1, pp. 15–29, 1988. DOI: `10.1177/002199838802200102`.

[96] L Davies, R Day, D Bond, A Nesbitt, J Ellis, and E Gardon, “Effect of cure cycle heat transfer rates on the physical and mechanical properties of an epoxy matrix composite”, *Composites Science and Technology*, vol. 67, no. 9, pp. 1892–1899, Jul. 2007, ISSN: 02663538. DOI: `10.1016/j.compscitech.2006.10.014`.

[97] L Liu, BM Zhang, DF Wang, and ZJ Wu, “Effects of cure cycles on void content and mechanical properties of composite laminates”, *Composite Structures*, vol. 73, no. 3, pp. 303–309, Jun. 2006, ISSN: 02638223. DOI: `10.1016/j.compstruct.2005.02.001`.

[98] SR White and HT Hahn, “Cure cycle optimization for the reduction of processing-induced residual stresses in composite materials”, *Journal of Composite Materials*, vol. 27, no. 14, pp. 1352–1378, Jan. 1993, ISSN: 0021-9983. DOI: `10.1177/002199839302701402`.

[99] Y Huang and RJ Young, “Interfacial behaviour in high temperature cured carbon fibre/epoxy resin model composite”, *Composites*, vol. 26, no. 8, pp. 541–550, Aug. 1995, ISSN: 00104361. DOI: `10.1016/0010-4361(95)92619-N`.

[100] S Ziaee and GR Palmese, “Effects of temperature on cure kinetics and mechanical properties of vinyl – ester resins”, *Journal of Polymer Science Part B: Polymer Physics*, vol. 37, no. July 1998, pp. 725–744, 1999, ISSN: 0887-6266. DOI: `10.1002/(SICI)1099-0488(19990401)37:7<725::AID-POLB23>3.0.CO;2-E`.

[101] J Zhang, YC Xu, and P Huang, “Effect of cure cycle on curing process and hardness for epoxy resin”, *Express Polymer Letters*, vol. 3, no. 9, pp. 534–541, 2009, ISSN: 1788618X. DOI: `10.3144/expresspolymlett.2009.67`.

[102] SR White and YK Kim, “Staged curing of composite materials”, *Composites Part A: Applied Science and Manufacturing*, vol. 27, no. 3 PART A, pp. 219–227, 1996, ISSN: 1359835X. DOI: `10.1016/1359-835X(95)00023-U`.

[103] PR Ciriscioli, GS Springer, and Q Wang, “A technique for determining mechanical properties of thick composite laminates”, *Journal of Composite Materials*, vol. 25, p. 1330, 1991. DOI: `10.1177/002199839102501005`.

[104] F Lahuerta, RPL Nijssen, FP van der Meer, and LJ Sluys, “Static and dynamic through thickness lamina properties of thick laminates”, in *ICCM20 - 20th International Conference on Composite Materials*, Copenhage, 2015, pp. 19–24.

[105] FYC Boey and SW Lye, “Effects of vacuum and pressure in an autoclave curing process for a thermosetting fibre-reinforced composite”, *Journal of Materials Processing Technology*, vol. 23, no. 2, pp. 121–131, 1990. DOI: `10.1016/0924-0136(90)90152-K`.

[106] DD Shin and HT Hahn, “A process sensitivity study of composite compressive strength”, *Journal of Thermoplastic Composite Materials*, vol. 11, no. 1, pp. 70–81, 1998. DOI: `10.1177/089270579801100104`.

[107] KV Kumar, M Safiulla, and ANK Ahmed, “An approach to cure thick fiber reinforced composite laminates”, *International journal of advanced and innovative research (IJAIR)*, vol. August, pp. 158–162, 2012.

[108] HT Hahn and KS Kim, “Residual stress development during processing of graphite/epoxy composites”, *Composites Science and Technology*, vol. 36, no. 2, pp. 121–132, 1989. DOI: `10.1016/0266-3538(89)90083-3`.

[109] TA Bogetti and JW Gillespie, “Process-induced stress and deformation in thick-section thermoset composite laminates”, *Journal of Composite Materials*, vol. 26, no. 5, pp. 626–660, 1992, ISSN: 0021-9983. DOI: `10.1177/002199839202600502`.

[110] F Lahuerta, RPL Nijssen, FP van der Meer, and LJ Sluys, “Experimental–computational study towards heat generation in thick laminates under fatigue loading”, *International Journal of Fatigue*, vol. 80, pp. 121–127, 2015. DOI: `10.1016/j.ijfatigue.2015.05.014`.

[111] *Astm d3479-12 standard test method for tension-tension fatigue of polymer matrix composite*, 2013. DOI: `10.1520/D3479\_D3479M-12`.

[112] F Lahuerta, T Westphal, and RPL Nijssen, “Self-heating forecasting for thick laminate specimens in fatigue”, *Journal of Physics: Conference Series*, vol. 555, p. 012 062, Dec. 2014. DOI: `10.1088/1742-6596/555/1/012062`.

[113] W Yin-Tao, G Liang-jin, and Y Ting-Qing, “Prediction of the 3-d effective damping matrix and energy dissipation of viscoelastic fiber composites”, *Composite Structures*, vol. 54, no. 1, pp. 49–55, Oct. 2001, ISSN: 02638223. DOI: `10.1016/S0263-8223(01)00069-1`.

[114] Z Zhang and G Hartwig, “Relation of damping and fatigue damage of unidirectional fibre composites”, *International Journal of Fatigue*, vol. 24, no. 7, pp. 713–718, Jul. 2002, ISSN: 01421123. DOI: `10.1016/S0142-1123(01)00206-7`.

[115] A Katunin, “Self-heating effect in laminate plates during harmonic forced loading”, *Scientific Problems of Machine Operation and Maintenance*, vol. 44, no. 2, pp. 73–84, 2009.

[116] PA Zinoviev and YN Ermakov, *Energy dissipation in composite materials.* Lancaster, Pennsylvania 17604 USA: Technomic Publishing Company Inc., 1994, p. 245, ISBN: 1-56676-082-8. DOI: `1-56676-082-8`.

[117] AT Echtermeyer, B Engh, and L Buene, “Lifetime and young’s modulus changes of glass/phenolic and glass/polyester composites under fatigue”, *Composites*, vol. 26, no. 1, pp. 10–16, Jan. 1995, ISSN: 00104361. DOI: `10.1016/0010-4361(94)P3624-A`.

[118] TL Bergman, FP Incropera, AS Lavine, and DP DeWitt, *Fundamentals of Heat and Mass Transfer*, 6th ed. John Wiley & Sons, Ltd, 2007.

[119] RL Taylor, KS Pister, and GL Goudreau, “Thermomechanical analysis of viscoelastic solids”, *International Journal for Numerical Methods in Engineering*, vol. 2, no. 1, pp. 45–59, 1970. DOI: `10.1002/nme.1620020106`.

[120] D Cugnet, C Hauviller, A Kuijper, V Parma, and G Vandoni, “Thermal conductivity of structural glass/fibre epoxy composite as a function of fibre orientation”, in *19th International cryogenic engineering conference ICEC19*, Grenoble, France, 2002.

[121] "Forced convection correlations. chapter 9 (url: www.pathways.cu.edu.eg/ec)", Cairo University, Faculty of Engineering, Cairo University, Tech. Rep., 2006, pp. 75–97. [Online]. Available: `http://www.pathways.cu.edu.eg/ec`.

[122] M Khandelwal and MM M Mench, "Direct measurement of through-plane thermal conductivity and contact resistance in fuel cell materials", *Journal of Power Sources*, vol. 161, no. 2, pp. 1106–1115, Oct. 2006, ISSN: 03787753. DOI: `10.1016/j.jpowsour.2006.06.092`.

[123] F Lahuerta, RPL Nijssen, FP van der Meer, and LJ Sluys, "Thickness scaled compression tests in unidirectional glass fibre reinforced composites in static and fatigue loading", *Composites Science and Technology*, vol. 123, pp. 115–124, 2015. DOI: `10.1016/j.compscitech.2015.12.008`.

[124] HM Hsiao, IM Daniel, and SC Wooh, "A new compression test method for thick composites", *Journal of Composite Materials*, vol. 29, no. 13, pp. 1789–1806, Sep. 1995. DOI: `10.1177/002199839502901307`.

[125] J Lee and C Soutis, "Thickness effect on the compressive strength of t800/924c carbon fibre–epoxy laminates", *Composites Part A: Applied Science and Manufacturing*, vol. 36, no. 2, pp. 213–227, Feb. 2005. DOI: `10.1016/j.compositesa.2004.06.010`.

[126] R Baldini, JI Bech, SH Madsen, and LP Mikkelsen, "Thick uni-directional composite testing for wind blades", in *Wind Turbine Blade Manufacture 2014*, Duesseldorf, DE, 2014.

[127] HM Hsiao, IM Daniel, and RD Cordes, "Dynamic compressive behavior of thick composite materials", *Experimental Mechanics*, vol. 38, no. 3, pp. 172–180, 1998. DOI: `10.1007/BF02325740`.

[128] F Lahuerta, T Westphal, RPL Nijssen, FP van der Meer, and LJ Sluys, "Static and fatigue performance of thick laminates test design and experimental compression results", in *ECCM-16Th European conference on composite materials*, Sevilla, Spain, 2014, pp. 1–9.

[129] SW Tsai and EM Wu, "A general theory of strength for anisotropic materials", *Journal of Composite Materials*, vol. 5, no. 1, pp. 58–80, 1971. DOI: `10.1177/002199837100500106`.

[130] F Lahuerta, RPL Nijssen, FP van der Meer, and LJ Sluys, "The influence of curing cycle and through thickness variability of properties in thick laminates", *Journal of Composite Materials*, vol. Prepublish, 2016. DOI: `10.1177/0021998316648758`.

[131] RB Prime, "Differential scanning calorimetry of the epoxy cure reaction", *Polymer Engineering & Science*, vol. 13, no. 5, pp. 365–371, 1973. DOI: `10.1002/pen.760130508`.

[132] MR Keenan, "Autocatalytic cure kinetics from dsc measurements: zero initial cure rate", *Journal of Applied Polymer Science*, vol. 33, no. 5, pp. 1725–1734, 1987. DOI: `10.1002/app.1987.070330525`.

[133] PJ Halley and ME Mackay, "Chemorheology of thermosets—an overview", *Polymer Engineering & Science*, vol. 36, no. 5, pp. 593–609, 1996. DOI: `10.1002/pen.10447`.

[134] H Kubota, “Curing of highly reactive polyester resin under pressure: kinetic studies by differential scanning calorimetry”, *Journal of Applied Polymer Science*, vol. 19, no. 8, pp. 2279–2297, 1975. DOI: `10.1002/app.1975.070190819`.

[135] A. Savitzky and MJE Golay, “Smoothing and differentiation of data by simplified least squares procedures.”, *Analytical Chemistry*, vol. 36, no. 8, pp. 1627–1639, Jul. 1964, ISSN: 0003-2700. DOI: `10.1021/ac60214a047`.

[136] M Waas and CR Schultheisz, “Compressive failure of composites, part ii: experimental studies”, *Progress in Aerospace Sciences*, vol. 32, no. 1, pp. 43–78, 1996. DOI: `10.1016/0376-0421(94)00003-4`.

[137] SH Lee, CS Yerramalli, and AM Waas, “Compressive splitting response of glass-fiber reinforced unidirectional composites”, *Composites Science and Technology*, vol. 60, no. 16, pp. 2957–2966, 2000. DOI: `10.1016/S0266-3538(00)00159-7`.

[138] R Hill, “A theory of the yielding and plastic flow of anisotropic metals”, *Proceedings of the Royal Society of London A: Mathematical, Physical and Engineering Sciences*, vol. 193, no. 1033, pp. 281–297, May 1948. DOI: `10.1098/rspa.1948.0045`.

[139] Z Hashin, “Failure criteria for unidirectional fiber composites”, *Journal of Applied Mechanics*, vol. 47, no. 2, pp. 329–334, Jun. 1980, ISSN: 0021-8936. DOI: `10.1115/1.3153664`.

[140] A Puck, “Failure analysis of frp laminates by means of physically based phenomenological models”, *Composites Science and Technology*, vol. 58, no. 7, pp. 1045–1067, Jul. 1998, ISSN: 02663538. DOI: `10.1016/S0266-3538(96)00140-6`.

[141] CG Davila, PP Camanho, and CA Rose, “Failure criteria for frp laminates”, *Journal of Composite Materials*, vol. 39, no. 4, pp. 323–345, Feb. 2005. DOI: `10.1177/0021998305046452`.

[142] AA Griffith, “The phenomena of rupture and flow in solids”, *Philosophical transactions of the Royal Society of London Series A*, vol. 221, pp. 163–198, 1921.

[143] T Kevin O’Brien and Roderick H Martin, “Results of astm round robin testing for mode 1 interlaminar fracture toughness of composite materials nasa-tm-104222”, Langley Research Center, Tech. Rep., 1992.

[144] JP Berry, “Determination of fracture surface energies by the cleavage technique”, *J. Appl. Phys.*, vol. 34, no. 1, pp. 62–68, 1963.

[145] S Hashemi, AJ Kinloch, and JG Williams, “The analysis of interlaminar fracture in uniaxial fibre-polymer composites”, *Proceedings of the Royal Society A: Mathematical, Physical and Engineering Sciences*, vol. 427, no. 1872, pp. 173–199, Jan. 1990, ISSN: 1364-5021. DOI: `10.1098/rspa.1990.0007`.

[146] *Astm d5528-01 (reapproved 2007) standard test method for mode i interlaminar fracture toughness unidirectional fiber-reinforced polymer matric composites*, 2001.

[147] *Fibre-reinforced plastic composites—determination of mode i interlaminar fracture toughness, gic, for unidirectionally reinforced materials iso/dis 15024*, 1999.

[148] K Kageyama and M Hojo, "Proposed methods for interlaminar fracture thougness tests of composite laminates", in *Proceedings of the 5th US/Japan conference on composite materials*, Tokyo, 1990, p. 227.

[149] *Astm d 6115-97 standard test method for mode i fatigue delamination growth onset of unidirectional fiber reinforced polymer matrix composites*, 2004.

[150] Ia Ashcroft and SJ Shaw, "Mode i fracture of epoxy bonded composite joints 2. fatigue loading", *Int. J. Adhes. Adhes.*, vol. 22, no. 2, pp. 151–167, Jan. 2002, ISSN: 01437496. DOI: `10.1016/S0143-7496(01)00050-1`.

[151] A Argüelles, J Viña, AF Canteli, MA Castrillo, and J Bonhomme, "Interlaminar crack initiation and growth rate in a carbon-fibre epoxy composite under mode i fatigue loading", *Compos. Sci. Technol.*, vol. 68, no. 12, p. 2325, Sep. 2008, ISSN: 02663538. DOI: `10.1016/j.compscitech.2007.09.012`.

[152] PD Mangalgiri, WS Johnson, and JR RA Everett, "Effect of adherend thickness and mixed mode loading on debond growth in adhesively bonded composite joints", in *Proceedings of the, 10th Annual Meiing of the Adhesion Society Inc.*, Michigan, 1987, p. 725.

[153] PC Paris, MP Gomez, and WE Anderson, "A rational analytical theory of fatigue", *The trend in engineering*, vol. 13, pp. 9–14, 1961.

[154] S Stelzer, AJ Brunner, A Argüelles, N Murphyd, and G Pinter, "Mode i delamination fatigue crack growth in unidirectional fiber reinforced composites: development of a standardized test procedure", *Compos. Sci. Technol.*, vol. 72, no. 10, pp. 1102–1107, 2012. DOI: `10.1016/j.compscitech.2011.11.033`.

[155] M Hojo, S Matsuda, M Tanaka, S Ochiai, and A Murakami, "Mode i delamination fatigue properties of interlayer-toughened cf/epoxy laminates", *Compos. Sci. Technol.*, vol. 66, no. 5, pp. 665–675, May 2006, ISSN: 02663538. DOI: `10.1016/j.compscitech.2005.07.038`.

[156] D Sans, J Renart, J Costa, N Gascons, and JA Mayugo, "Assessment of the influence of the crack monitoring method in interlaminar fatigue tests using fiber bragg grating sensors", *Compos. Sci. Technol.*, vol. 84, pp. 44–50, Jul. 2013, ISSN: 02663538. DOI: `10.1016/j.compscitech.2013.04.022`.

[157] BD Manshadia, AP Vassilopoulosb, and J Botsis, "A combined experimental/numerical study of the scaling effects on mode i delamination of gfrp", *Compos. Sci. Technol.*, pp. 32–39, 2013. DOI: `10.1016/j.compscitech.2013.04.016`.

[158] S Yarlagadda, A AbuObaid, MK Yoon, N Hager, and R Domszy, "An automated technique for measuring crack propagation during mode i dcb testing", *Conference: 2004 SEM X International Congress & Exposition on Experimental & Applied Mechanics*, 2004.

[159] C Uhlig, O Kahle, B Wieneke, and M Bauer, "Optical crack tracing - a new method for the automatic determination of fracture toughness for crack initiation and propagation", in *MicroMat 2000. Proceedings 3rd International Conference and Exhibition Micro Materials*, Berlin, Germany, 2000, pp. 618–629.

[160] V Richter-Trummer, EA Marques, FJP Chaves, J Tavares, LFM da Silva, and P de Castro, “Analysis of crack growth behavior in a double cantilever beam adhesive fracture test by different digital image processing techniques”, *Materialwiss. Werkstofftech.*, vol. 42, no. 5, pp. 452–459, 2011. DOI: `10.1002/mawe.201100807`.

[161] P Dare, H Hanley, C Fraser, B Riedel, and W Niemeier, “An operational application of automatic feature extraction: the measurement of cracks in concrete structures”, *The Photogrammetric Record*, vol. 17, no. 99, pp. 453–464, Apr. 2002, ISSN: 0031-868X. DOI: `10.1111/0031-868X.00198`.

[162] DH Ryu and SH Nahm, “Image processing techniques applied to automatic measurement of the fatigue-crack”, *Key Eng. Mater.*, vol. 297-300, pp. 34–39, Aug. 2005, ISSN: 1662-9795. DOI: `10.4028/www.scientific.net/KEM.297-300.34`.

[163] G van Rossum and FL Drake, *Python reference manual*. PythonLabs, Virginia, USA, 2001, pp. 1–100.

[164] G Bradski, “The opencv library”, *Dr. Dobb’s Journal of Software Tools*, pp. 1–2, Nov. 2000.

[165] P Levi, “Course image understanding”, University of Stuttgart, Germany, Tech. Rep., 2011.

[166] J Canny, “A computational approach to edge detection”, *IEEE Trans. Pattern Anal. Mach. Intell.*, vol. 8, no. 6, pp. 679–98, Jun. 1986, ISSN: 0162-8828. DOI: `10.1109/TPAMI.1986.4767851`.

[167] N Otsu, “A threshold selection method from gray-level histograms”, *IEEE Trans. Syst. Man Cybern.*, vol. 20, no. 1, pp. 62–66, 1979. DOI: `10.1109/TSMC.1979.4310076`.

[168] JJ Kuiken, “Wmc measurement and control system. wmcs manual wmc-2013-096”, WMC Knowledge Centre, Wieringerwerf, NL, Tech. Rep., 2013, pp. 1–3.

[169] *Astm e647-13 standard test method for measurement of fatigue crack growth rates*, 2013.

[170] F Lahuerta, RPL Nijssen, FP van der Meer, and LJ Sluys, “Infrared inspection of thick laminates during fatigue tests”, in *7th International Conference on Composites Testing and Model Identification*, IMDEA, 2015, pp. 7–8.

[171] G Pitarresi, a Normanno, and L D’Acquisto, “Thermoelastic stress analysis of a 2d stress field using a single detector infrared scanner and lock-in filtering”, *Journal of Physics: Conference Series*, vol. 181, p. 012 075, 2009. DOI: `10.1088/1742-6596/181/1/012075`.

[172] JH Oh and DG Lee, “Cure cycle for thick glass / epoxy composite laminates”, *Journal of Composite Materials*, vol. 36, no. 01, pp. 19–45, 2002. DOI: `10.1106/00219980202330`.

[173] A Cheung, Y Yu, and K Pochiraju, “Three-dimensional finite element simulation of curing of polymer composites”, *Finite Elements in Analysis and Design*, vol. 40, no. 8, pp. 895–912, 2004. DOI: `10.1016/S0168-874X(03)00119-7`.

LIST OF FIGURES

LIST OF TABLES

ACKNOWLEDGEMENTS

My gratitude to my mentors Bert Sluys, Frans van der Meer and Rogier Nijssen for the support of my Ph.D study and research. Their guidance helped me during the research and writing of this thesis. Besides my mentors, I would like to thanks the committee for their contribution.

Thanks to WMC employees who provided me the opportunity to join their team, and granted me open access to the laboratory and research facilities. Without their support, openness and kindness it would not be possible to conduct this research.

Last but not least, sincere gratitude to my friends "por los tiempos heróicos", family, auntie and parents.

* * *

"We acknowledge financial support for this research from ADEM. A green Deal in Energy Materials of the Ministry of Economic Affairs of The Netherlands www.adem-innovationlab.nl"

ABBREVIATIONS

α	*degree of cure or conversion factor*
$\dot{q}$	*internal heat generation*
ν	Poisson coeficient
ρ	*density*
σ	stress
σ_{max}	*ultimate strength*
τ	shear stress
c_P	*specific heat*
CLC	*combine loading compression*
COV	*coefficient of variance*
$d\alpha/dt$	*curing rate*
DSC	*differential scanning calorimeter*
dT	*differential of temperature field*
dt	*differential of time*
dT/dt	*heating rate*
E	elastic moduli
F	*failure index field*
FWR	*fiber weight ratio*
G_{Ic}	critical fracture energy release rate in mode I
G_{IIc}	critical fracture energy release rate in mode II
H_r	*total heat of reaction*

$ILSS$	*interlaminar shear strength test*
$ILSS_{max}$	*maximum interlaminar shear strength*
K_x, K_y, K_z	*thermal conductivity fields per coordinate*
PP	*peel-ply*
R	*coefficient of determination*
$R-ratio$	*fatigue stress ratio*
R_t	*heating rate*
R_α	*curing rate*
S	*strength field*
$S-N$	*stress versus cycles to failure fatigue curve*
T	*temperature field*
t	*time*
T_g	*glass transition temperature*
x, y, z	*spatial coordinates*
Biax	biaxial material
CFRP	carbon fiber reinforced polymer
COE	cost of energy
COV	coefficient of variance
DCB	double cantilever beam
FE	finite element method
FFT	Fast Fourier Transform
G	shear moduli
GFRP	glass fiber reinforced polymer
IR	infrared
PPT	phase pulse thermography

PTFE	politetrafluoroetileno
TF	test factor
TSA	thermoelastic stress analysis
UD	unidirectional
UV	ultraviolet

LIST OF PUBLICATIONS

JOURNAL CONTRIBUTIONS

[1] F Lahuerta, RPL Nijssen, FP van der Meer, and LJ Sluys, “Thickness scaled compression tests in unidirectional glass fibre reinforced composites in static and fatigue loading”, *Composites Science and Technology*, vol. 123, pp. 115–124, 2015. DOI: `10.1016/j.compscitech.2015.12.008`.

[2] F Lahuerta, RPL Nijssen, FP van der Meer, and LJ Sluys, “Experimental–computational study towards heat generation in thick laminates under fatigue loading”, *International Journal of Fatigue*, vol. 80, pp. 121–127, 2015. DOI: `10.1016/j.ijfatigue.2015.05.014`.

[3] F Lahuerta, T Westphal, RPL Nijssen, FP van der Meer, and LJ Sluys, “Measuring the delamination length in static and fatigue mode i tests using video image processing”, *Composites Part B: Engineering*, vol. 63, pp. 1–7, 2014. DOI: `10.1016/j.compositesb.2014.03.003`.

[4] F Lahuerta and RPL Nijssen, “Energy dissipation in thermoset composites in mode i fatigue”, *Mechanics of Advanced Materials and Structures*, vol. Prepublish, 2015. DOI: `10.1080/15376494.2015.1124950`.

[5] F Lahuerta, RPL Nijssen, FP van der Meer, and LJ Sluys, “The influence of curing cycle and through thickness variability of properties in thick laminates”, *Journal of Composite Materials*, vol. Prepublish, 2016. DOI: `10.1177/0021998316648758`.

CONFERENCE CONTRIBUTIONS

[1] F Lahuerta, T Westphal, and RPL Nijssen, “Self-heating forecasting for thick laminate specimens in fatigue”, *Journal of Physics: Conference Series*, vol. 555, p. 012 062, 2014. DOI: `10.1088/1742-6596/555/1/012062`.

[2] F Lahuerta, RPL Nijssen, FP van der Meer, and LJ Sluys, “Effect of laminate thickness on the static and fatigue properties of wind turbine composites”, in *10th EAWE PhD Seminar in Wind Energy*, Orleans: EAWE Secretariat, 2014.

[3] F Lahuerta, RPL Nijssen, FP van der Meer, and LJ Sluys, “Infrared inspection of thick laminates during fatigue tests”, in *7th International Conference on Composites Testing and Model Identification*, IMDEA, 2015, pp. 7–8.

[4] F Lahuerta, RPL Nijssen, FP van der Meer, and LJ Sluys, “Static and dynamic through thickness lamina properties of thick laminates”, in *ICCM20 - 20th International Conference on Composite Materials*, Copenhage, 2015, pp. 19–24.

[5] F Lahuerta, S Raijmaekers, JJ Kuiken, T Westphal, and RPL Nijssen, "Automated delamination length video tracking in static and fatigue dcb test", in *6th International Conference on Composites Testing and Model Identification*, Aalborg, DK, 2013, pp. 6–7.

[6] F Lahuerta, T Westphal, RPL Nijssen, FP van der Meer, and LJ Sluys, "Static and fatigue performance of thick laminates test design and experimental compression results", in *ECCM-16TH European conference on composite materials, Seville*, Sevilla, Spain, 2014, pp. 1–9.

[7] F Lahuerta, T Westphal, and RPL Nijssen, "Self-heating forecasting for thick laminates testing coupons in fatigue", in *The Science of Making Torque from Wind, Torque*, Oldenburg, Germany, 2012, pp. 1–8. [Online]. Available: `uuid:2ae6c0d9-c5cc-4ac9-b4ed-2a62e6071e2c`.

[8] RPL Nijssen, T Westphal, F Lahuerta, and DRV Van Delft, "Recent results in characterisation and modeling of composites for wind turbine blades", in *Composites week @ LEUVEN and TEXCOMP-11 Conference*, Leuven, 2013.

PROPOSITIONS

1. Composites scaling effects must be a fact since full-scale component tests are still required.
2. The strength and fatigue life of a thick laminate of thickness h are influenced by each infinitesimal part with thickness dh, where the fatigue life and strengths of each infinitesimal part depends on the local curing history and flaws.
3. Who you know opens doors. What you know builds new doors.
4. A model is the expression of an incomplete scientific understanding.
5. To conceptualize a problem is part of the solution. To simplify a problem is part of the conceptualization.
6. Populism is seen as the answer, as long as no questions are asked and no explicit answers are expected.
7. Technology is the search for the maximum outcome with the minimum effort.
8. To universalize knowledge deprecates its value.
9. Supervisors who are certain about all research issues produce poor PhD-students, since doubt is part of the learning process.

These propositions are regarded as opposable and defendable, and have been approved as such by the supervisor prof. dr. ir. Bert Sluys.

STELLINGEN

1. Schalingseffecten van composieten moeten een onontkoombaar feit zijn, aangezien full-scale testen nog steeds vereist worden.
2. De sterkte en vermoeiingslevensduur van een dik laminaat met dikte h worden beïnvloed door elk infinitesimaal deel met dikte dh, waarbij de vermoeiingslevensduur en sterkte van ieder infinitesimaal deel afhankelijk zijn van het lokale uithardingsverloop en materiaalafwijkingen.
3. Deuren gaan open door wie je kent. Deuren ontstaan door wat je weet.
4. Een model is de uitdrukking van onvolledig wetenschappelijk begrip.
5. Het conceptualiseren van een probleem is onderdeel van de oplossing. Het vereenvoudigen van een probleem is onderdeel van de conceptualisatie.
6. Populisme wordt gezien als het antwoord, zo lang er maar geen vragen gesteld worden en geen concrete antwoorden worden verwacht.
7. Technologie is de zoektocht naar het maximale resultaat voor de minimale inspanning.
8. Het vrij beschikbaar maken van kennis vermindert haar waarde.
9. Begeleiders die zeker zijn over alle kwesties van een onderzoek leveren armzalige promovendi, aangezien twijfel een deel van het leerproces is.

Deze stellingen worden opponeerbaar en verdedigbaar geacht en zijn als zodanig goedgekeurd door de promotor prof. dr. ir. Bert Sluys.